SHORT-WAVE INFRARED OPTICAL IMAGING TECHNIQUES FOR THE ASSESSMENT AND QUANTIFICATION OF DENTAL DISEASE

by

CHRISTINE CHARLES SAHYOUN

A dissertation submitted to the

School of Graduate Studies

Rutgers, The State University of New Jersey

In partial fulfillment of the requirements

For the degree of

Doctor of Philosophy

Graduate Program in Biomedical Engineering

Written under the direction of

Mark C. Pierce

And approved by

_____

_____

_____

_____

_____

New Brunswick, New Jersey

January, 2020

ABSTRACT OF THE DISSERTATION

Short-wave infrared optical imaging techniques for the assessment and quantification of dental disease

By CHRISTINE CHARLES SAHYOUN

Dissertation Director:

Mark C. Pierce

Periodontal disease and tooth decay are conditions that, if detected early enough, can be corrected or reversed. Visual inspection and radiography are the current standard detection methods for such conditions, and while cracks and caries can be identified with this methodology, dental lesions can only be detected through radiography once the disease has progressed significantly. There is a need for non-invasive, accurate, and quantitative assessment of both dental and periodontal tissue to allow for prompt diagnosis and subsequent treatment. Optical imaging approaches may offer improved assessments because they can provide full-field information from within the first few millimeters of tissue depth, which is appropriate for assessing both tooth layers (enamel and dentin) and gingival tissue. This dissertation is focused on developing optical techniques for quantitatively assessing dental tissue in a non-invasive, non-destructive manner for translation into clinical work.

Optical coherence tomography (OCT) is a technique that uses infrared light to generate cross-sectional images of sub-surface tissue structure. While OCT has been investigated for dental applications, the elements of an OCT system can be configured differently and optimized for the requirements of specific applications, and there are several different commercially available OCT systems that can be used for dental applications. It had not yet been established which combination of system configurations and parameters is best for detection and quantification of enamel indications. Chapters 2

and 3 focus on applications of OCT for hard dental tissue assessment. Chapter 2 provides a detailed comparison of commercially available OCT systems using healthy enamel samples to demonstrate the performance of each system in relation to dental imaging. The systems in Chapter 2 were then utilized for the assessment and quantification of both artificial and natural white spot lesions in Chapter 3. Lesion formation, depth, and heterogeneity were assessed through OCT-established parameters to provide quantitative visualization of white spot lesions that could be used for both clinical identification of lesions and assessment of treatment efficacy.

Spatial frequency domain imaging (SFDI) is another imaging modality that can be performed with infrared wavelengths to provide absolute quantification of tissue chromophore concentrations, including water. There appears to be only one report directly performing SFDI at short-wave infrared (SWIR) wavelengths for the extraction of water and lipid content, but this work is limited in wavelength range and utilizes measurements at many wavelengths in order to get accurate results. Optimization of both wavelength and spatial frequency choices needs to be conducted to lead to system simplification without sacrificing accuracy of chromophore extraction. Chapters 4 and 5 spotlight SWIR-SFDI for potential use in both oral and dental health evaluation. Chapter 4 details the creation of a SWIR-SFDI system and optimization of wavelength and spatial frequency selection for accurate extraction of water and lipid content using phantoms. Chapter 5 utilizes this system to provide a spatially resolved map of reduced scattering for the natural white spot lesion samples from Chapter 3, demonstrating the capability of the SWIR-SFDI system to provide quantitative assessment of hard dental tissue in addition to hydration evaluation.

Publications and Presentations

Several sections of this dissertation and related research have been published in a peer-reviewed journal and/or presented at scientific conferences.

Peer-reviewed journal publications:

Sahyoun CC, Subhash HM, Peru D, Ellwood RP, Pierce MC. "A comparison of optical coherence tomography systems for non-invasive assessment of hard dental tissues." *Caries Research* (2019). DOI: doi.org/10.1159/000502375

Conference presentations (* indicates presenting author):

Sahyoun CC*, Dumas JP, Zhao Y, Applegate MB, Roblyer DM, Pierce MC, "Short-wave infrared spatial frequency domain imaging for non-invasive quantification of tissue water content." Presented as an oral presentation at *SPIE Photonics West* – San Francisco, CA. Feb 2019.

Sahyoun CC, Subhash HM, Peru D, Ellwood RP, Zaidel L, Kilpatrick L, Pierce MC*, "A comparison of structural and functional optical coherence tomography systems for assessment of hard dental tissues." Presented as a poster at *SPIE Translational Biophotonics* – Houston, TX. May 2018

Sahyoun CC*, Subhash HM, Peru D, Ellwood RP, Zaidel L, Kilpatrick L, Pierce MC, "Effect of optical coherence tomography resolution on the assessment of dental enamel indications." Presented as a poster at *OSA Biomedical Optics Conference* – Hollywood, FL. Apr 2018

Sahyoun CC*, Pierce MC, “Spatial frequency domain imaging for noninvasive assessment of tissue hemodynamic properties.” Presented as a poster at *BMES Annual Conference* – Tampa, FL. Oct 2015.

Other presentations (* indicates presenting author):

Sahyoun CC*, “A Comparison of Structural and Functional Optical Coherence Tomography Systems for Assessment of Hard Dental Tissues.” Oral presentation at the *New York Section Society for Applied Spectroscopy* – Piscataway, NJ. Oct 2018.

Acknowledgement

Chapter 2 of this dissertation has been published in Caries Research, and a license to republish the article in this dissertation was obtained. Copyright © 2019 Karger Publishers, Basel, Switzerland.

Sahyoun CC, Subhash HM, Peru D, Ellwood RP, Pierce MC. "A comparison of optical coherence tomography systems for non-invasive assessment of hard dental tissues." *Caries Research* (2019). DOI: doi.org/10.1159/000502375

Table of Contents

List of Figures and Tables

Chapter 1: Background and introduction

1.1 Pathophysiology of dental and oral disease

Gingivitis and periodontitis are diseases of the gums that produce inflammation, which can result in damage and recession of the gums as well as tooth decay in the case of the latter[1]. Both conditions serve as risk factors and indicators for systemic disease, and conversely, systemic conditions including immune disorders and diabetes have been found to negatively affect the periodontium[1]. In addition to physical wellness, oral health is important for an individual's psychological and social quality-of-life[1]. If diagnosed early, some of these conditions can be corrected or reversed, making it important to have reliable methods of detection. Probing pocket depths, probe-induced bleeding, clinical attachment loss, and measurement of salivary biomarkers are typical clinical methods used to detect periodontal disease[2,3]. The current clinical detection methods for dental conditions are visual inspection and radiography, but the latter can only detect cracks and lesions once they have progressed significantly[4]. There is thus a need for non-invasive, accurate, and quantitative assessment of both dental and periodontal tissue to allow for detection of such conditions in their early stages when topical interventions can be applied. Optical imaging approaches may offer solutions to this challenge and were investigated in this work.

Biological changes such as enamel demineralization, tissue (de)hydration, and inflammation can alter the optical properties of the affected tissue, potentially allowing for distinction from healthy tissue. For example, as enamel undergoes demineralization, its microstructure and refractive index changes, creating detectable variations in backscattered light intensity and polarization. The increase in porosity of enamel results in an increase in (back)scattering of incident light that increases signal intensity, with demineralized enamel also causing depolarization of light[5]. In gingival tissue, physiological changes and inflammation may also lead to differences in backscattered

light due to the variations in content of blood and water, chromophores that have strong absorption at particular wavelengths; these changes lead to differences in absorption and scattering that provide different contrast levels depending on the state of the tissue and the wavelength of incident light, allowing for the evaluation of periodontal health. Optical imaging systems can be constructed or purchased at a relatively low cost, which makes them feasible for use in primary care settings. Such effects make optical imaging an ideal approach for detection of dental and oral disease. To optimize these systems for detection of the various aforementioned dental conditions, it is important to understand the relevant physical changes that occur for each, and how these changes translate to differences in optical properties.

1.1.1 Enamel demineralization

Enamel is largely comprised of bundles of hydroxyapatite crystals, which are collectively termed enamel prisms[6]. Demineralization is the dissolution of these crystals either from the center or periphery of the structure, leading to the formation of pores[6,7]. Healthy enamel typically cycles between demineralization and remineralization, but an imbalance in this cycle leaning towards the former will result in the formation of a carious lesion[8]. Several different factors can affect a tooth's susceptibility to the development of caries. Host factors, such as variations in mineral content of the enamel structure as well as saliva composition and flow, can make a tooth more or less susceptible to caries[8]. Diet also has a heavy impact on caries formation, with carbohydrates and specifically sucrose contributing to the production of acids and to the adhesion and formation of plaque[8]. Plaque microorganisms such as *Streptococcus mutans* further contribute to the progression of demineralization through continued acid production[8]. The roughening of the enamel structure that results from the demineralization process leads to changes in the intensity of backscattered light that could be detected with optical imaging methods.

1.1.2 White spot lesions

White spot lesions (WSLs) broadly encompass carious and non-carious lesions[9]. Carious WSLs are opaque, white, and chalky in appearance as well as rough and porous[9]. These lesions are the middle men between early demineralization and cavitated caries[9]. Non-carious WSLs, on the other hand, are shiny and smooth in appearance, and are of developmental origin (i.e. fluorosis, enamel hypoplasia)[9]. While the various factors mentioned in the section above all play a role in an individual's susceptibility to the formation of WSLs, orthodontic appliances such as braces provide additional challenges to oral hygiene and allow for more surface area for plaque to attach to, leading to an increased risk of lesion formation[9]. It is important to manage these lesions before they progress to cavitated caries, and remineralizing agents such as topical fluoride and amorphous calcium phosphate are used to do so[9,10]. Remineralization rates between carious and non-carious WSLs vary, with a higher remineralization rate observed with carious WSLs[11]. It is therefore important to identify WSLs early into their development to determine the appropriate treatment route to prevent further progression and/or remineralize the lesion. The same light scattering properties described for demineralization is section 1.1.1 are observed with WSLs, but there is a distinct, intact enamel surface above the WSL.

1.1.3 Gingival inflammation

Gingivitis and periodontitis are diseases of the supporting structures of the teeth[8]. Gingivitis is gingival inflammation caused by an accumulation of plaque around the gingival margin; this can further progress to inflammation of the periodontal tissue loss of attachment from the teeth, or periodontitis[8]. The presence of plaque triggers an immune response that has a part in both the initiation and progression of periodontal diseases, as well as in the recovery from such conditions[8]. The inflammatory response to the

subgingival plaque leads to an increase in gingival crevicular fluid (GCF) and associated antibodies that indicate involvement of T-cells and B-cells[8]. While this response is meant to be protective, it also damages the tissue and can further progress the disease[8]. Chronic marginal gingivitis results in swelling and redness of the gingival tissue, often accompanied with bleeding but not pain[8]. An initial acute lesion forms, which is then followed by further progression of clinical levels of inflammation until an established lesion and periodontal pocket have formed; this pocket contains a large population of B lymphocytes, plasma cells, and neutrophils[8]. The increased presence of inflammatory cells, blood, and water may change the absorption and scattering of incident light and may potentially be distinguishable from healthy tissue through differences in backscattered intensity of incident light.

1.1.4 Dry mouth

Saliva plays an important role in oral health in many ways including lubrication and antimicrobial properties, promotion of remineralization of teeth, and transportation of digestive enzymes[12]. When an individual experiences salivary gland hypofunction (SGH), or decreased saliva secretion, it is often termed "dry mouth"[12]. Dry mouth can be attributed to a wide array of causes, from old age and habits (i.e. smoking and alcohol use), to medications and chemotherapy, or chronic inflammatory autoimmune disease (i.e. Sjogren's syndrome)[12]. Beyond discomfort, dry mouth increases the risk of demineralization and dental caries, as well as difficulty in speech and eating[12]. Treatment of dry mouth is focused on symptom management through the use of salivary stimulators and/or oral moisturizers[12]. Given that saliva is composed mostly of water, having an imaging modality that can detect and/or quantify hydration content would allow for the tracking of dry mouth severity and/or treatment. With water having strong absorption in the short-wave infrared spectral range (900 to 1,700 nm), measuring diffuse reflectance

using such wavelengths can potentially provide water-dependent contrast differences that can be quantified.

1.2 Short-wave infrared imaging modalities

The structural and functional changes that arise from the previously discussed conditions alter the optical absorption and scattering properties of the affected tissue. These changes may allow for distinction from healthy tissue, particularly if tissue is assessed using wavelengths of light in the short-wave infrared spectral region. Optical coherence tomography and spatial frequency domain imaging are two imaging modalities that can be performed at short-wave infrared wavelengths to provide visualization and quantification of structural changes and variations in tissue chromophore content. The fundamental operating principles of these systems and their current usage in dental applications will be discussed in this section.

1.2.1 Optical coherence tomography

Optical coherence tomography (OCT) is a technique that uses infrared light to generate cross-sectional images of sub-surface tissue structure. The OCT light source is typically connected to a fiber-optic circulator that directs light to a beam splitter, sending light to both the tissue and to a stationary reference mirror. Light returning from different depths within the tissue and from the reference mirror is recombined at the beam splitter, resulting in a spectral interference pattern that contains information on the depth locations of structural features within the tissue. A Fourier transformation of the measured interference pattern provides a 1-dimensional profile of the reflected light intensity as a function of depth (Z) within the tissue, also known as an *A-line*. By transversely scanning the beam across the tissue in the X-direction, multiple A-lines can be acquired from adjacent tissue locations to generate a 2-dimensional cross-sectional image in the XZ

plane, or *B-scan*. Finally, if the beam is also scanned in the Y-direction, collection of sequential B-scans results in a 3-dimensional volumetric dataset, or *C-scan*. The spectral interference pattern can be obtained in two different ways. In "spectral-domain" (SD)-OCT, the light source emits a broad spectrum of wavelengths and interference at each wavelength is measured simultaneously by using a spectrometer as the detector. In "swept-source" (SS)-OCT, the light source emits a single wavelength that is swept across a broad range of wavelengths in a time-dependent manner; in this case the interference pattern is measured at each wavelength sequentially by using a single photodetector. For a given tissue sample, the measured interference pattern should be the same for both SD-OCT and SS-OCT approaches. These steps are visualized in the schematic in **Figure 1.1**.

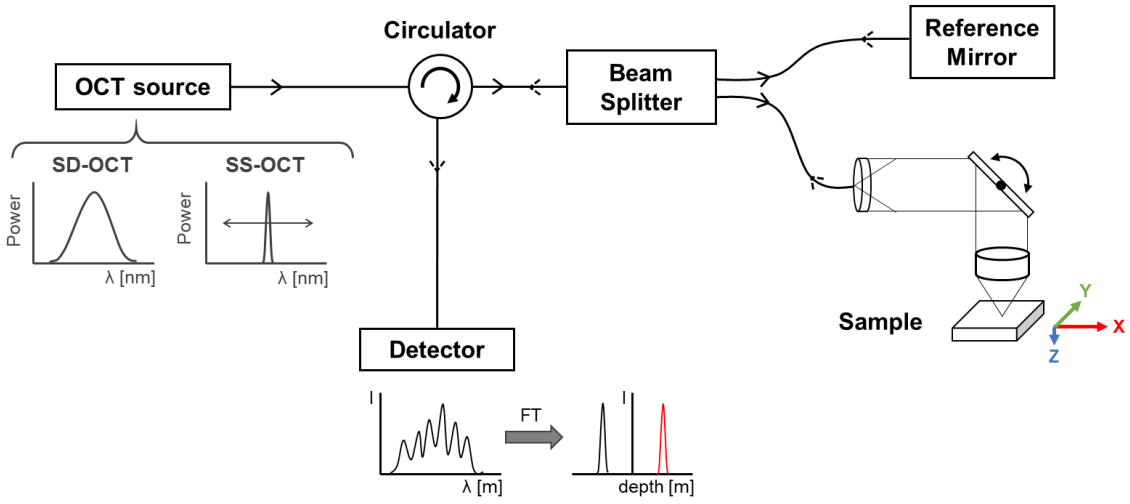

Figure 1.1 OCT system schematic. The OCT light source is connected to a fiber-optic circulator that directs light to a beam splitter, sending light to both the tissue and to a stationary reference mirror. Light returning from different depths within the tissue and from the reference mirror is recombined at the beam splitter, resulting in a spectral interference pattern that contains information on the depth locations of structural features within the tissue. A Fourier transformation of the measured interference pattern provides a 1-dimensional A-line. Transverse scanning in the X-direction generates a B-scan and scanning of the beam in the Y-direction allows for volumetric data collection (C-scan).

OCT has been investigated previously both *in vitro* and *in vivo* across a wide range of dental applications[13,14] including enamel defects[14-16], demineralization[17-21], remineralization[22,23], caries[24-27], non-carious lesions[28], white spot lesions[5], restorations[29], biofilms[30], and orthodontic studies[31,32]. **Figure 1.2** depicts B-scans of healthy tooth (**Figure 1.2A**), near-surface demineralization (**Figure 1.2B**), and deep demineralization (**Figure 1.2C**)[33]. From these cross-sections, the enamel and dentin layers can be clearly seen in the healthy tooth scan, and the greater backscattered intensity (red arrows) due to the demineralized tissue allows for clear distinction between diseased and healthy tissue.

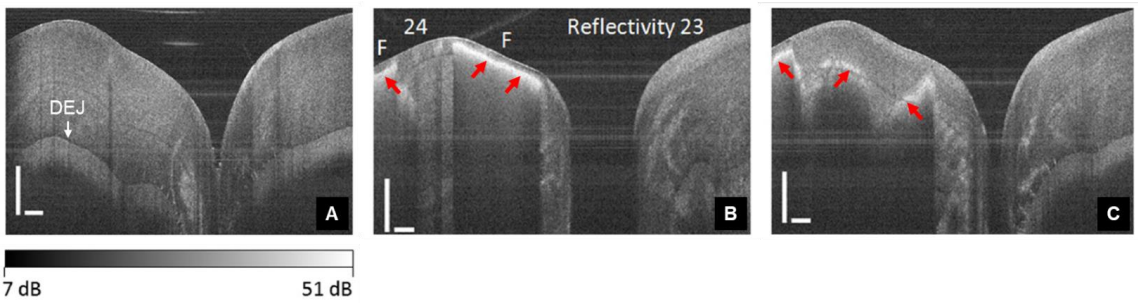

Figure 1.2 OCT B-scans of various enamel indications. **(A)** healthy enamel, **(B)** near-surface demineralization, and **(C)** deep demineralization. Scale bars correspond to 500 microns. The dentin-enamel junction (DEJ) is indicated in **(A)**, and the red arrows in **(B)** and **(C)** indicate regions of high backscattering intensity due to the presence of demineralized lesions. Adapted from Figure 6 from Walther *et al.*[33] used under CC BY 4.0. / select panels used, and arrows added for visual assistance.

Most dental OCT studies reported previously used light sources operating in the 1,300 nm wavelength range, with low numerical aperture (NA) (high f-number) imaging lenses. Under these conditions, OCT images extend up to around 2 mm in sub-surface depth with approximately 10 μm resolution, allowing visualization of fine structural details within the enamel and dentin layers. However, these elements of an OCT system can be configured differently and optimized for the requirements of specific applications, and

there are several different commercially available OCT systems that can be used for dental applications. It has not yet been established which combination of system configurations and parameters is best for detection and quantification of enamel indications.

1.2.2 Near infrared and short-wave infrared reflectance imaging

Near infrared (NIR) and short-wave infrared (SWIR) multispectral reflectance imaging is another optical technique that has been investigated for the assessment of dental indications. This method is simple in its execution, with images acquired by illuminating the sample with various wavelength light sources (i.e. LEDs, lasers) and capturing the diffuse reflectance of each with a detector (i.e. camera). NIR/SWIR multispectral imaging has been explored for dental applications, motivated by the decreased scattering of light in tissue at these wavelengths[34-37]. Previous studies have found an increase in lesion contrast when illuminated with longer wavelengths (i.e. beyond 1,300 nm). A studied conducted by Chung *et al.* compared reflectance images from a tooth with occlusal decay using visible (300-800 nm), and SWIR (1,300 nm and 1,460 nm) illumination (**Figure 1.3**)[35]. The greatest contrast was observed with the 1,460 nm illumination (**Figure 1.3C**), followed by the 1,300 nm (**Figure 1.3B**) and finally the visible range (**Figure 1.3A**), where lesion distinction is almost impossible. Contrast also increases with lesion depth and severity[35,36], providing further functionality of this imaging modality. Therefore, multispectral imaging can potentially assess enamel lesions over a large field-of-view in an *en face* manner, rather than the cross-sectional method given by OCT.

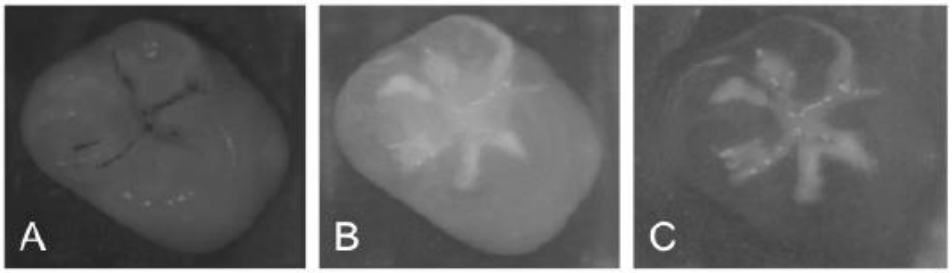

Figure 1.3 Reflectance images of a tooth with occlusal decay. Reflectance images of occlusal decay at **(A)** 300-8800 nm, **(B)** 1,300 nm, and **(C)** 1,460 nm. Increased lesion contrast is apparent with longer wavelengths. Dark likes in (A) are stains, not decay. Reprinted with permission from Chung *et al.*[35] © The Optical Society.

1.2.3 Short-wave infrared spatial frequency domain imaging

Spatial frequency domain imaging (SFDI) is a noninvasive technique that can go one step beyond multi/hyper-spectral imaging and provide absolute quantification of tissue chromophore concentrations. The fundamental basis of SFDI is to project structured light patterns onto the tissue and capture the diffusely reflected light, the magnitude of which depends on both the optical properties of the tissue and the spatial frequency of the projected pattern. This is necessary because different combinations of tissue absorption and scattering coefficients can produce the same diffuse reflectance value. If only uniform incident light was used, it would not be possible to determine a unique pair of absorption and scattering coefficients that produced the measured diffuse reflectance. To overcome this, SFDI utilizes the principle that the diffuse reflectance of an object varies with the spatial frequency of incident light. Therefore, by imaging an object under illumination with light at multiple (known) spatial frequencies, the absorption and reduced scattering coefficients of the sample can be extracted. Optical properties vary with wavelength, so when these measurements are obtained using different wavelengths of light, the overall absorption and reduced scattering spectra of the tissue can be measured as a function of wavelength. The measured absorption spectrum can be treated as a linear combination of contributions from the major tissue chromophores (i.e. hemoglobin, oxyhemoglobin,

water, and lipid). Since this combination is based on concentration-dependent contributions, the absorption / extinction spectra of the pure chromophores can be used to calculate how much of each chromophore is present in the sample.

SFDI can be implemented in various ways, and the current state of this imaging modality has been recently reviewed[38]. A schematic of a typical setup and the processing steps is provided in **Figure 1.4**. Depending on the application, the light source and wavelength choices may vary, but the process is the same. The light source is directed onto a digital micromirror device, which is used to sequentially project three equally phase-shifted illumination patterns per spatial frequency onto the sample. The diffuse reflectance images are then captured with a camera and stored for processing.

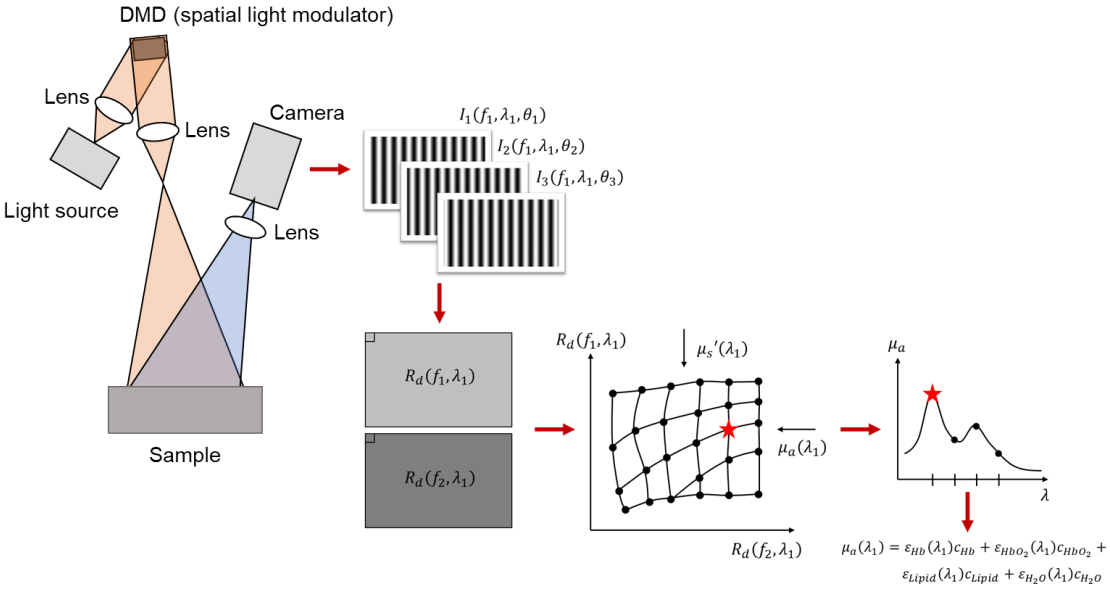

Figure 1.4 Schematic of SFDI setup and processing steps. The light source is directed onto a digital micromirror device, which is used to sequentially project three equally phase-shifted illumination patterns per spatial frequency onto the sample, and the reflectance images are captured with a camera. The measurement of the amplitude modulation (M_{AC}) for each spatial frequency is determined through single-pixel demodulation. A look-up table generated through Monte Carlo simulations is used to extract absorption and reduced scattering coefficients. This extraction of optical properties is repeated at different wavelengths in order to produce overall absorption, which is treated as a linear combination of the different tissue constituents.

The measurement of the amplitude modulation (M_{AC}) for each spatial frequency is determined through single-pixel demodulation using the following equation:

$$M_{AC}(f_1,\lambda_1) = \frac{\sqrt{2}}{3}\cdot\left\{\begin{matrix}[I_1(f_1,\lambda_1,\theta_1) - I_2(f_1,\lambda_1,\theta_2)]^2 + [I_2(f_1,\lambda_1,\theta_2) - I_3(f_1,\lambda_1,\theta_3)]^2 + \\ [I_3(f_1,\lambda_1,\theta_3) - I_1(f_1,\lambda_1,\theta_1)]^2\end{matrix}\right\}^{1/2} \quad (1.1)$$

Usually, just two spatial frequencies are used: one low frequency (typically 0 mm^{-1}) and one high frequency. This measurement of the amplitude modulation (M_{AC}) represents the diffuse reflectance of the sample combined with an unknown "instrument factor". To determine this factor, a reference phantom of known optical properties, and therefore known diffuse reflectance $R_{d,red,pred}(f_1,\lambda_1)$, is measured with the system $M_{AC,ref}(f_1,\lambda_1)$:

$$Instrument\ factor\ (f_1,\lambda_1) = \frac{M_{AC,ref}(f_1,\lambda_1)}{R_{d,red,pred}(f_1,\lambda_1)} \quad (1.2)$$

This instrument factor is determined for all spatial frequencies and all wavelengths. All future measurements of unknown samples (M_{AC}) are then divided by this instrument factor to get the sample's true diffuse reflectance (R_d) at each wavelength. In a two-spatial frequency scenario (after correction with the calibration phantom), there are two R_d measurements per wavelength. In order to convert from diffuse reflectance to optical properties, a look-up table is often used, which is generated through Monte Carlo simulations and consists of different predicted R_d values for samples using ranges of absorption and reduced scattering values at the two specific frequencies. This extraction of optical properties is repeated at different wavelengths in order to produce overall absorption and reduced scattering spectra. The overall absorption of a sample at a single wavelength, λ_i , can be described as a linear sum of concentration-dependent

contributions from individual chromophores, and at multiple wavelengths, each chromophore concentration can be determined through the matrix equation[39]:

$$\begin{bmatrix} \mu_a(\lambda_1) \\ \vdots \\ \mu_a(\lambda_j) \end{bmatrix} = \begin{bmatrix} \varepsilon_1(\lambda_1) & \cdots & \varepsilon_N(\lambda_1) \\ \vdots & \ddots & \vdots \\ \varepsilon_1(\lambda_j) & \cdots & \varepsilon_N(\lambda_j) \end{bmatrix} * \begin{bmatrix} c_1 \\ \vdots \\ c_N \end{bmatrix} \quad (1.3)$$

where μ_a is the sample's absorption coefficient, $\varepsilon_n(\lambda_i)$ is the extinction coefficient of chromophore "n" at a designated wavelength, λ_i, c_n is the chromophore concentration, N is the total number of chromophores being considered, and j is the number of measured wavelengths.

SFDI utilizing visible/NIR wavelengths has been implemented in many biomedical applications, providing information on oxy- and deoxy-hemoglobin concentrations for applications including assessment of burn wounds, pressure ulcers, and tumor resections. SFDI provides pixel-by-pixel mapping of absorption and scattering coefficients which can show the variations in these coefficients over the entire image and allow for the distinction between normal and malignant ovarian tissue[40]. Further characterization can be achieved using SWIR wavelengths (approximately 900 – 1,700 nm) due to distinctive absorption bands of water, lipid, and collagen in this spectral range. Quantification of these tissue components may have clinical significance in relation to oral health topics such as inflammation and dry mouth. Due to the influence of water in these implications, using SWIR wavelengths that water has high absorption at can help quantify water content, which can be used to track severity or treatment of inflammation or dry mouth. Previous work on extending SFDI into the SWIR region combined VIS/NIR-SFDI with planar imaging at SWIR wavelengths[41]. Due to the scattering changes of the enamel with demineralization, the reduced scattering coefficient mapping provided with SFDI could be used to identify and quantify enamel lesions in a quick and quantitative manner. There is

currently no literature directly performing SFDI at SWIR wavelengths for absolute quantification of water content and/or tissue scattering for the assessment of dental health.

1.3 Dissertation overview

The scope of this work is to establish SWIR imaging techniques for the non-invasive and quantitative assessment of dental tissue and related conditions. Chapters 2 and 3 focus on applications of OCT for hard dental tissue assessment, while Chapters 4 and 5 spotlight SWIR-SFDI for potential use in both oral and dental health evaluation. Chapter 2 provides a detailed comparison of commercially available OCT systems using healthy enamel samples to demonstrate the performance of each system in relation to dental imaging. The systems in Chapter 2 were then utilized for the assessment and quantification of both artificial and natural white spot lesions in Chapter 3. Lesion formation, depth, and heterogeneity were assessed through OCT-established parameters to provide quantitative visualization of white spot lesions that could be used for both clinical identification of lesions and assessment of treatment efficacy. Chapter 4 details the creation of a SWIR-SFDI system and optimization of wavelength and spatial frequency selection for accurate extraction of water and lipid content using phantoms. Chapter 5 utilizes this system to provide a spatially resolved map of reduced scattering for the natural white spot lesion samples from Chapter 3, demonstrating the capability of the SWIR-SFDI system to provide quantitative assessment of hard dental tissue in addition to hydration evaluation.

Chapter 2: An experimental review of optical coherence tomography systems for non-invasive assessment of hard dental tissues[1]

2.1 Introduction

There is a need for real-time non-invasive imaging methods to better detect and quantify dental pathology. Optical coherence tomography (OCT) is an emerging technique that uses near-infrared light to generate cross-sectional images of sub-surface tissue structure. OCT has been investigated previously both *in vitro* and *in vivo* across a wide range of dental applications[13,14] including enamel defects[14-16], erosion[42], demineralization[17-21], remineralization[22,23], caries[24-27], non-carious lesions[28], white spot lesions[5], restorations[29], biofilms[30], and orthodontic studies[31,32]. To further transition this technology into standard clinical practice and facilitate imaging of hard to access areas, handheld OCT probes have also been developed and tested for dental applications[43,44]. OCT can be implemented in several different ways, with properties of the light source, imaging lenses, and detection unit impacting the achievable depth, resolution, field-of-view, and contrast. Most dental OCT studies use light sources operating in the 1300 nm wavelength range and low numerical aperture (NA) imaging lenses. Under these conditions, OCT images can extend up to around 2 mm in depth with approximately 10 μm axial resolution, allowing visualization of fine structural details within the enamel and dentin layers. However, these elements of an OCT system can be configured differently

[1] This chapter has been published in Caries Research, and a license to republish the article in this dissertation was obtained.

Sahyoun CC, Subhash HM, Peru D, Ellwood RP, Pierce MC. "A comparison of optical coherence tomography systems for non-invasive assessment of hard dental tissues." Caries Research (2019). DOI: doi.org/10.1159/000502375

and optimized for the requirements of specific applications. For example, a light source emitting longer wavelengths generally provides greater imaging depth in tissue, but also has poorer axial (depth) resolution for a given spectral bandwidth[45]. Imaging lenses with higher NA provide better lateral resolution but suffer from a shallower depth-of-field and typically a smaller field-of-view.

Once the light source properties and imaging optics are selected, OCT images can be generated in two distinct ways; (1) using a broadband light source and a spectrometer for detection, termed “spectral domain” OCT (SD-OCT), or (2) using a narrowband light source which rapidly sweeps across a broad wavelength range, with a single photodetector, termed “swept source” OCT (SS-OCT). Both approaches measure the spectral interference pattern generated between light returning from the tissue sample and from a stationary reference mirror, producing similar cross-sectional OCT images. OCT can also be implemented in “polarization-sensitive” mode, whereby measurement of the polarization state of backscattered light can provide functional information on the degree of structural organization of the tissue.

OCT has potential for use in several dental applications, but each may have different requirements for imaging depth, resolution, and field-of-view[21]. The aim of this chapter was to experimentally characterize and demonstrate the performance of different commercially available systems, imaging lenses, and detection modules on OCT imaging performance in direct relation to enamel imaging. In this chapter, the impact of these choices on visualization and quantification of dental imaging depth is examined using sound tooth samples to help guide users in determining the optimal setup for their specific applications.

2.2 Methods

2.2.1 Optical coherence tomography principles and systems

The general setup of OCT comprises a light source whose output is divided at a beam splitter, sending light to both the tissue and to a stationary reference mirror. Light returning from different depths within the tissue and from the reference mirror is recombined at the beam splitter, resulting in a spectral interference pattern that contains information on the depth locations of structural features within the tissue. A Fourier transformation of the measured and calibrated interference pattern provides a 1-dimensional profile of the reflected light intensity as a function of depth (Z) within the tissue, also known as an *A-line*. By transversely scanning the beam across the tissue in the X-direction, multiple A-lines can be acquired from adjacent tissue locations to generate a 2-dimensional cross-sectional image in the XZ plane, or *B-scan*. Finally, if the beam is also scanned in the Y-direction, collection of sequential B-scans results in a 3-dimensional volumetric dataset, or *C-scan*.

The spectral interference pattern can be obtained in two different ways. In “spectral-domain” (SD)-OCT, the light source emits a broad spectrum of wavelengths and interference at each wavelength is measured simultaneously by using a spectrometer as the detector. In “swept-source” (SS)-OCT, the light source emits a single wavelength that is swept across a broad range of wavelengths in a time-dependent manner; in this case the interference pattern is measured at each wavelength sequentially by using a single photodetector. For a given tissue sample, the measured interference pattern should be the same for both SD-OCT and SS-OCT approaches. In this study, two SD-OCT systems (Lumedica, OQ LabScope 1.0 (**Figure 2.1A**) and Thorlabs, Tel320 (**Figure 2.1B**)) were used. The Lumedica OQ LabScope 1.0 is a cost-efficient ($10k) system, while the Thorlabs Tel320 is a high-end platform ($80k). The technical specifications of these

systems are detailed in **Table 2.1**. The maximum sensitivity and sensitivity roll-off were determined for each system by measuring the signal from a gold mirror attenuated by calibrated neutral density filters, as detailed in[46]. The depth of field for each system was assessed by moving a sharp edge through the focal plane and calculating the lateral resolution from the measured edge spread function at each axial position[47]. The lateral (X and Y) scan distances were confirmed for both systems by imaging a chrome-on-glass grid target (Thorlabs R1L3S3P) with 500 µm markers.

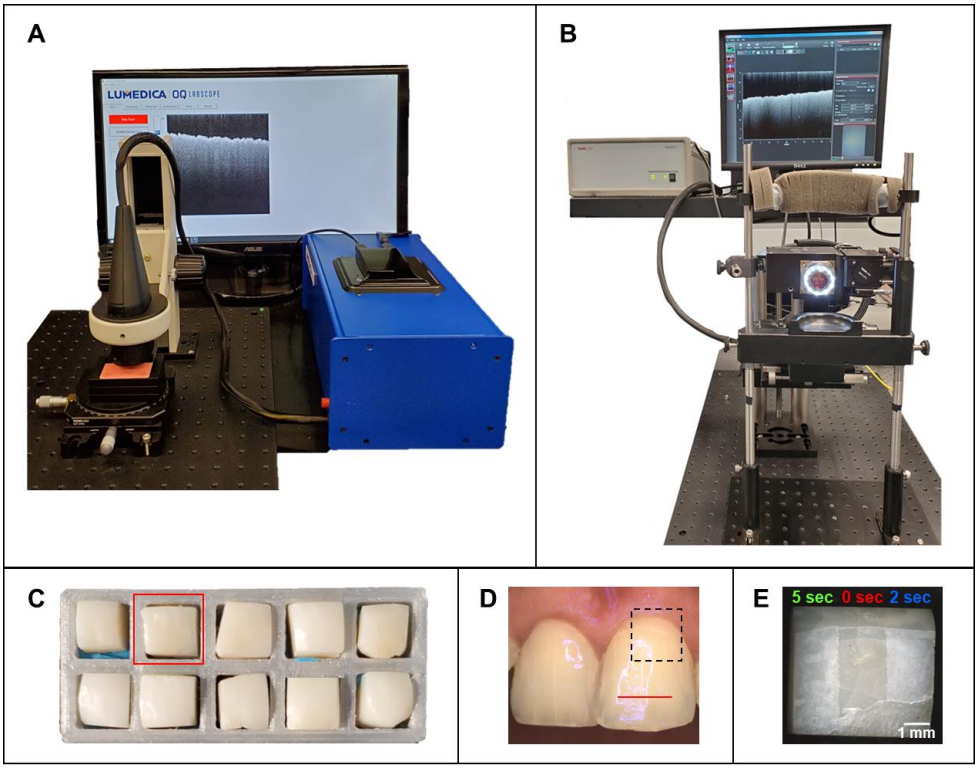

Figure 2.1. Imaging systems and study samples. (A) The OQ LabScope 1.0 OCT setup, with the probe facing downwards to demonstrate the configuration for *in vitro* data collection. **(B)** The Tel320 setup, with the probe facing outwards with the chin rest to demonstrate the configuration for *in vivo* data collection. **(C)** 10 human molar samples mounted in a 3-D-printed holder; each segment of the holder measures 4.5 x 4.5 mm. The red box indicates the sample shown in Figure 2.3. **(D)** *In vivo* human subject, with the dashed box on tooth #9 corresponding to the area scanned for volumetric OCT data (Figure 2.4). The red line corresponds to the location used for collection of PS-OCT data (Figure 2.6). **(E)** Bovine enamel sample with three distinct regions of demineralization following 0 s, 2 s, and 5 s exposure to 30% phosphoric acid.

Table 2.1. Technical specifications of the commercial SD-OCT systems compared in this study

	Lumedica OQ LabScope 1.0	**Thorlabs Tel320**
Center wavelength, nm	840	1,300
Bandwidth (FWHM), nm	45	100
Maximum pixels per A scan	512	1,024
Axial resolution[1] (air), μm	9	5.7
Imaging depth[1] (air), mm	2.6	3.6
A-scan line rate, kHz	8.8	10[2], 28, 76, 146
Sensitivity[1], dB	95	112 (at 10 kHz)
Output power[1]	460 μW	5 mW
NA (BD/2f)	0.050	0.062
Lateral resolution, μm	15	13

BD, beam diameter; f, focal length.
[1] Values that were measured in this study. All other values were taken from manufacturing specifications.
[2] A-scan line rate used for this study.

To demonstrate the effect of sample arm NA on transverse image resolution, a SS-OCT system (Thorlabs, OCS1300SS) was used with a typical OCT lens (Thorlabs, LSM03) providing a working NA of 0.04, and with a microscope objective (Mitutoyo, M Plan Apo NIR 20x) providing a working NA of 0.15. This SS-OCT system has a central wavelength of 1325 nm, spectral bandwidth (FWHM) of 64 nm, imaging depth of 3 mm in air, and an axial resolution of 12 μm in air. To compare imaging in conventional and polarization-sensitive modes, a dual-channel detection module (Thorlabs, PSOCT-1300) was added to the SS-OCT system for simultaneous collection of interference patterns in horizontal and vertical polarization states.

2.2.2 Tissue specimens and human subjects

To demonstrate differences in imaging depth and image quality between the two SD-OCT systems when imaging hard dental tissue, ten sound extracted human molar

samples were cut and mounted in a custom, 3-D-printed holder (**Figure 2.1C**) for volumetric OCT imaging. *In vivo* imaging was performed with a healthy male subject; IRB approval and informed consent was obtained for such *in vivo* imaging. Volumetric OCT data was taken near the top of the left central incisor (#9), including tooth and gingival tissue in the scan (region indicated by the dashed box in **Figure 2.1D**). To demonstrate differences in system NA, bovine enamel was eroded under different acid challenge conditions; bovine was chosen over human enamel due to its larger size. A 5 mm x 5 mm x 3 mm polished bovine enamel sample underwent demineralization by exposure to 30% phosphoric acid (**Figure 2.1E**). One third of the sample was exposed for 2 seconds, one third exposed for 5 seconds, and one third was protected with yellow vinyl tape (3M) to create a non-acid exposed, control (0 second) region. Immediately following the phosphoric acid exposure, the entire sample was rinsed in running water for one minute and dried with compressed air for 20 seconds.

2.2.3 Data collection and analysis

For SD-OCT system comparison using both *in vivo* and *in vitro* tissues, volumetric data were collected with the scanning beam acquiring 512 A-lines over a 5 mm wide B-scan (X-direction), and 512 B-scans over a 5 mm transverse scan (Y-direction) for both systems. The sample arm focus was set at a distance of 0.75 mm from the zero optical path difference position (top of the image) in both systems by adjusting the sample arm lens to maximize the signal measured from a reflective sample positioned at this axial location. The OCT probe was oriented in a downward-facing direction for *in vitro* data collection, as demonstrated with the OQ LabScope 1.0 in **Figure 2.1A**, and in a forward-facing direction with a chin-rest apparatus for *in vivo* imaging, as seen with the Tel320 in **Figure 2.1B**. Raw spectral interference data were acquired from each system, which

underwent the same standard OCT processing steps (interpolation to linear k-space, Fourier transformation, logarithmic scaling) to produce B-scans in units of decibels (dB). An appropriate dynamic range was set for each system, and this range was used to map the dB values across 256 grayscale levels for image display. A-lines (1-D depth profiles) from *in vivo* data were generated by plotting the intensity in decibels as a function of depth for the designated A-line(s). For B-scans and A-line profiles, the image depth was adjusted to account for the refractive index of enamel (1.6). Intensity profiles for the ten *in vitro* samples were generated by realigning 100 B-scans within the middle of the volume to the sample surface so that all depth measurements were made relative to the enamel surface, and then averaging 200 logarithmically-scaled A-lines within each B-scan to reduce noise and provide a mean intensity profile per sample, which was then rescaled to range from 0 to 1 based on the dynamic range chosen for each system. These normalized mean intensity profiles for the ten samples were then averaged together to provide a mean intensity profile and imaging depth in sound enamel for each OCT system.

Motion artifacts inevitably occur with *in vivo* imaging, and this can affect the appearance of OCT images. Since B-scans are captured in a fraction of a second, subject motion has relatively little effect on individual 2-D cross-sectional images. However, 3-D volumes require several seconds to minutes to acquire, and subject motion during this time interval this can appear as horizontal banding in *en face* (XY plane) reconstructions generated from 3-D datasets. To reduce these artifacts, all B-scan images within each *in vivo* volume were adjusted such that the top 1% and bottom 1% of all pixel values were saturated (at values of 255 and 0 respectively). 3-D tissue volumes were reconstructed by importing the 512 adjusted B-scans into the open-source ImageJ software package[48] using the *Volume Viewer* plugin. The “projection” or “slice” display feature was then used to generate *en face* views from the 3-D dataset. Due to the natural curvature of *in vivo*

tissue, a single XY-plane “slice” will not capture the surface but rather a plane within the depth of the tissue; therefore, the “projection” view was saved, in which voxels are projected from the 3-D volume into a 2-D image plane using user-adjustable “alpha” values as weights. With the *in vitro* bovine sample being flat for volume acquisition, the slice at a specific depth (i.e. the surface of the sample) within the volume was saved to provide the *en face* view.

2.3 Results

2.3.1 SD-OCT system characterization

The characterization results for the two commercial SD-OCT systems are shown in **Figure 2.2**. The lateral resolution, calculated as the distance between 10% and 90% signal level across a sharp reflecting edge, at various axial positions is evaluated in **Figure 2.2A**. A steeper drop-off in lateral resolution is observed with the Tel320 compared to the OQ LabScope 1.0. Sensitivity roll-off results for the OQ LabScope 1.0 and the Tel320 are shown in **Figures 2.2B** and **2.2C**, respectively. The sensitivity roll-off in the first 1.5 mm of imaging depth is 1 dB for the OQ LabScope 1.0, and 2 dB for the Tel320. The maximum sensitivity was measured as 95 dB for the OQ LabScope 1.0, and 112 dB for the Tel320 (**Table 2.1**).

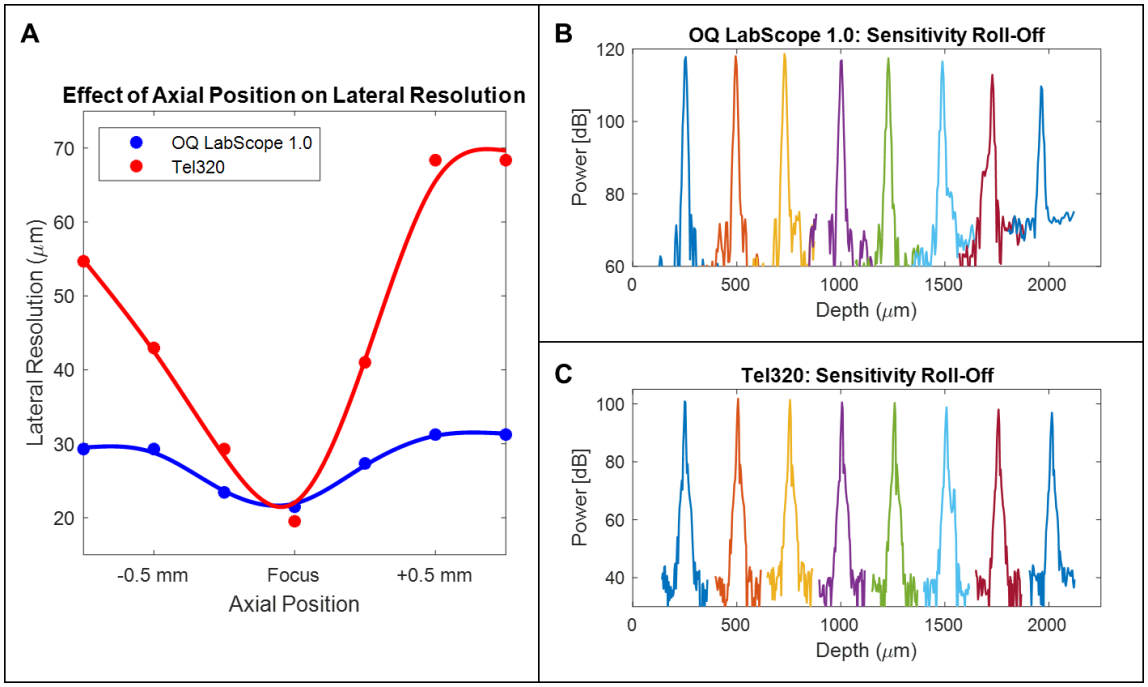

Figure 2.2 Characterization data for commercial SD-OCT systems. **(A)** Lateral resolution measured at axial locations above and below the focal plane for both systems. Sensitivity as a function of depth for **(B)** the OQ LabScope 1.0 with a neutral density filter of OD 1.7 placed in the sample arm, and **(C)** the Tel320 with a neutral density filter of OD 2.0.

2.3.2 Comparison of commercially available SD-OCT systems with healthy enamel samples

Data from OCT volume scans of 10 healthy tooth samples are displayed in **Figure 2.3**. Projected *en face* views (XY plane) for a single representative sample acquired with the OQ LabScope 1.0 and the Tel320 systems are shown in **Figures 2.3A** and **2.3C**, respectively, both corresponding to the tooth sample within the red box in **Figure 3E**. Individual B-scans in **Figures 2.3B** and **2.3D** correspond to the same cross-sectional location (XZ plane) along the orange horizontal line indicated in each *en face* view. The average intensity for all 10 samples as a function of depth is shown for each system in **Figure 2.3E**, with the solid lines representing the mean for the 10 samples, and the shaded areas indicating the standard deviations. These plots illustrate increased imaging depth

with the Tel320 OCT system compared to the OQ LabScope 1.0; based on the depth at which the signal dropped to an *ad hoc* level of 0.02 in the normalized plots, the mean imaging depth in tissue of the Tel320 is 2.6 times greater than that of the OQ LabScope 1.0 (1.6 mm ± 0.1 mm vs. 0.6 mm ± 0.2 mm).

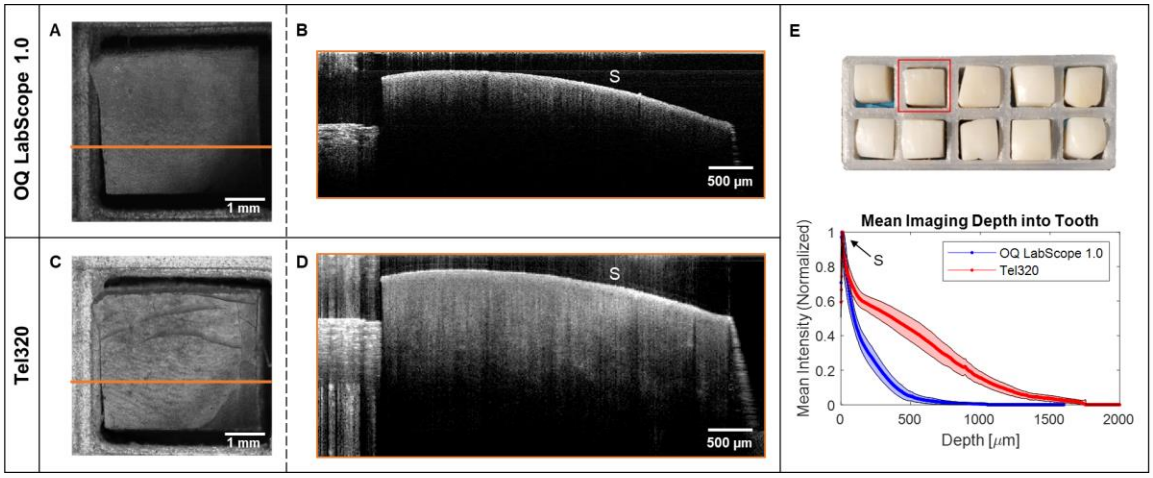

Figure 2.3 *In vitro* comparison of SD-OCT systems. *In vitro* comparisons of the OQ LabScope 1.0 **(A,B)** and the Tel320 **(C,D)** systems using 10 sound human molar samples **(E)**. Panels (A) and (C) show *en face* projections from volumetric OCT datasets acquired from the sample indicated by the red box in (E). Panels (B) and (D) show individual B-scans at the location of the orange line in the *en face* views. The plot in (E) shows the mean imaging depth into tooth for the ten samples for each system, with the standard deviation illustrated as the shaded region around each plot. S = enamel surface.

In vivo data from OCT volume scans of the healthy subject are shown in **Figure 2.4**. Projected *en face* views for both systems are shown in **Figures 2.4A** and **2.4C**, which correspond to the region of interest outlined in red in **Figure 2.4E**, including a portion of the left central incisor and adjacent gingiva. Individual B-scans in **Figures 2.4B** and **2.4D** correspond to cross-sections (XZ plane) along the orange horizontal line indicated in each *en face* view. Individual A-line profiles are displayed in **Figure 2.4E** corresponding to the backscattered intensity as a function of depth along the blue vertical lines indicated in

each B-scan. The *en face* views show clear distinction between gingival tissue and tooth, and in both a crack can be observed in the *en face* views and B-scans (green arrows). Horizontal banding artifacts are more prominent in the OQ LabScope 1.0 *en face* reconstruction (**Figure 2.4A**) compared to the Tel320 *en face* view (**Fig 2.4C**). The increased imaging depth of the Tel320 is apparent in the B-scans and A-line profiles, but the DEJ is visible at this location in both systems in this example, as indicated in **Figures 2.4B,D,E**, though it is less prominent with the OQ LabScope 1.0.

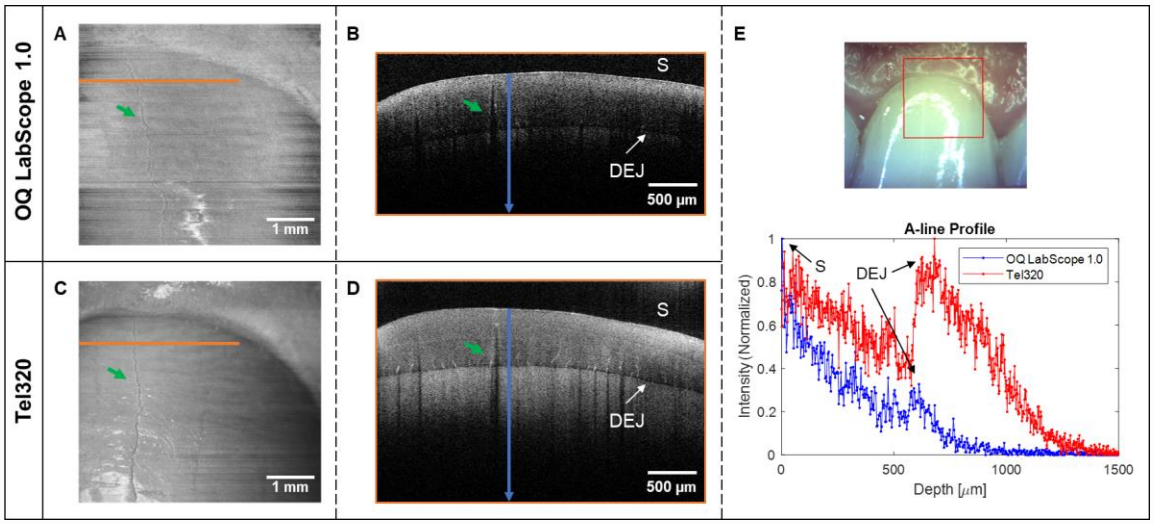

Figure 2.4 *In vivo* comparison of SD-OCT systems. *In vivo* comparisons of the OQ LabScope 1.0 **(A,B)** and the Tel320 **(C,D)** systems. Panels (A) and (C) show *en face* projection views generated from volumetric OCT datasets, corresponding to the red box in the white light image in **(E)**. Panels (B) and (D) are B-scans taken from the dataset at the location of the orange line in the *en face* views. The location of a crack in the tooth is indicated by a green arrow in the *en face* views and B-scans. The plot in (E) shows A-line intensity profiles along the blue lines shown in the B-scans. S = enamel surface. DEJ = dentin-enamel junction.

2.3.3 Effect of OCT sample arm numerical aperture (NA) on lateral resolution

Lateral resolution for high and low NA sample arm lenses was determined by collecting volumetric data from a USAF 1951 resolution target (Edmund Optics, 38-257)

with the 1325 nm SS-OCT system. Resolution was determined as the width of one line-pair at which the contrast is above 26.4% (Rayleigh's criterion). The lateral resolution of the OCT system was measured to be 22.1 μm for the 0.04 NA lens, and 5.5 μm for the 0.15 NA lens. The effect of lens NA on lateral image resolution is demonstrated in **Figure 2.5** using the demineralized bovine sample. For both lenses (**Figures 2.5A,B**), OCT volumes were acquired by scanning the beam over four different sized areas of the sample in the XY plane. As in traditional microscopy, higher NA objective lenses typically have higher magnification and smaller FOV. It is evident that the 0.04 NA lens (**Figure 2.5A**) with its 9.3 mm x 9.3 mm FOV can image the entire 5 mm x 5 mm sample; reducing the scan size effectively "zooms in" on a region of the sample. However, the 0.15 NA lens has a smaller FOV (0.55 mm x 0.55 mm), resulting in only a portion of the sample being imaged at larger scan sizes (**Figure 2.5B**). The increased lateral resolution provided by the 0.15 NA lens is demonstrated by OCT intensity line profiles extracted from across the boundary between sound and demineralized enamel (along the red horizontal lines in **Figures 2.5C,D**). The vertical dashed line in each line profile plot indicates the location of the boundary, with increased contrast to surface roughness evident with the higher NA lens (**Figure 2.5D**), particularly in the demineralized region to the left of the boundary.

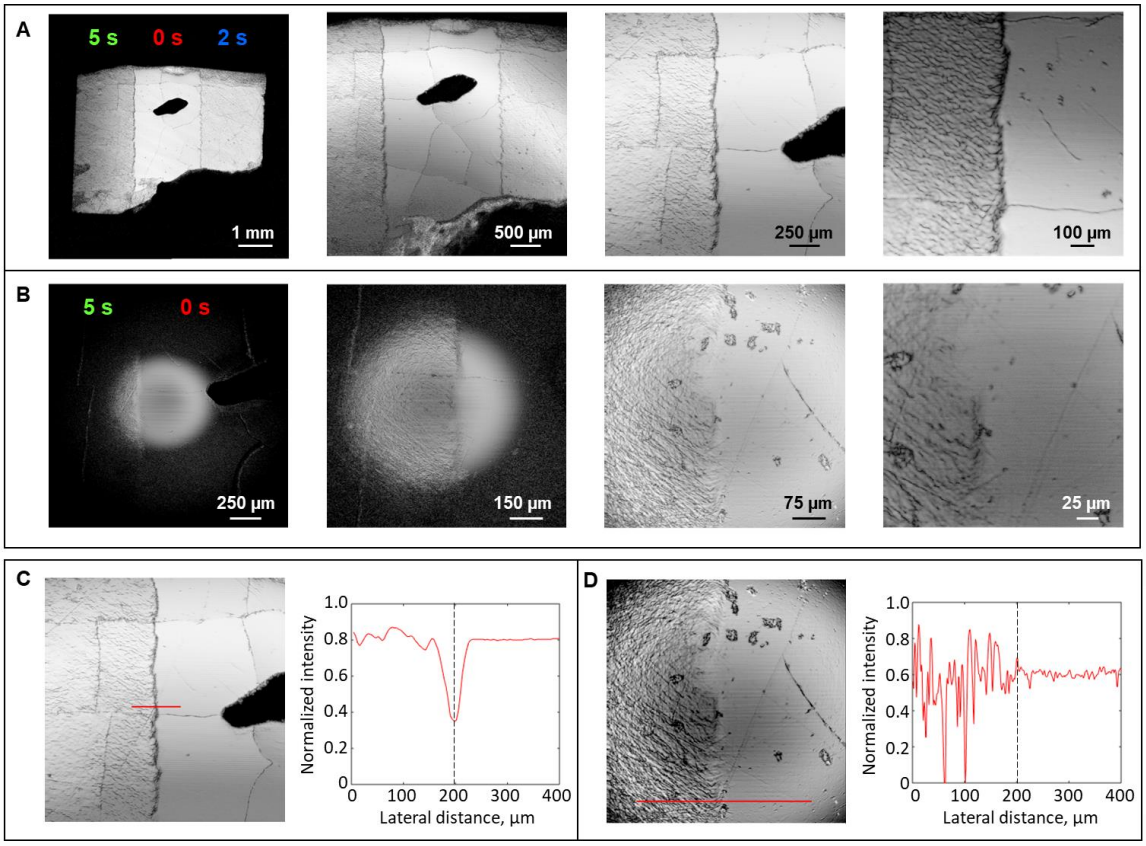

Figure 2.5 *In vitro* comparison of high and low numerical aperture lenses in the OCT sample arm. *En face* views of a demineralized enamel sample imaged with the 0.04 NA lens **(A)**, and 0.15 NA lens **(B)** for increasing scan sizes (left to right). Line profiles for the 2 mm x 2 mm scan settings of the same region with the 0.04 NA lens **(C)** and the 0.15 NA lens **(D)**. The plotted line profile corresponds to the red line in the *en face* slice view.

2.3.4 Use of Polarization-Sensitive OCT (PS-OCT)

The use of a polarization-sensitive OCT detection module for *in vivo* imaging is shown in **Figure 2.6**. Enamel is a birefringent material, which means that it can alter the polarization state of light propagating within it. This effect can lead to unwanted artifacts in OCT images when polarization-sensitive imaging is not used. OCT imaging relies on interference between light returning from different depths within the sample and from the stationary reference mirror. Light returning from near the surface of the sample will be in the same polarization state as light from the reference mirror and will generate a high

contrast interference pattern. Light returning from deeper within a birefringent sample can change to a modified polarization state that is no longer matched to that of light returning from the reference mirror, resulting in reduced modulation depth in the interference fringes and a low-intensity region in the sample (arrows in **Figure 2.6A**). The resulting dark bands in OCT images can be misinterpreted as real tissue structure, but they can be eliminated by using a polarization-sensitive module with two detectors to collect light in both vertical and horizontal polarization states (**Figure 2.6B**). Beyond simply eliminating this artifact, useful information about the tissue's structural properties can be extracted by analyzing the change in polarization state of light with depth in the sample. Tissue with a high degree of structural organization or molecular alignment exhibits higher birefringence, which in turn causes the polarization state of light to change more quickly as it propagates within the material. **Figure 2.6C** shows a "phase retardation" image which displays the change in polarization state as an angle relative to the sample surface (0°). A more highly birefringent sample will quickly alter the polarization state of light which will be apparent as a rapid cycling of phase retardation from 0° (black) to 180° (red) to 360° (black) with depth in the image. Tissue which is not birefringent will present a phase retardation image which is uniformly black (0°). Tissue which randomly scrambles the polarization state of light will generate a phase retardation image with a random mixture of angles from 0° to 360° (colors from black to red).

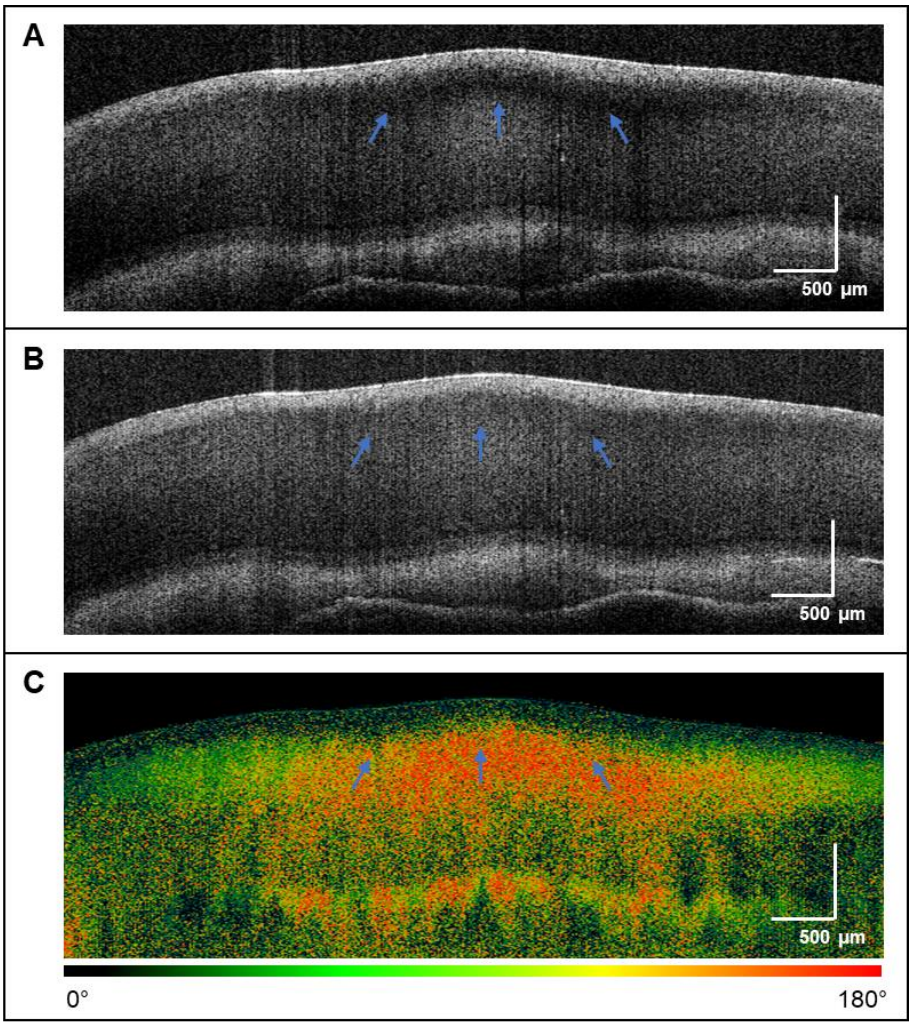

Figure 2.6 *In vivo* comparison of conventional and polarization-sensitive (PS) detection units. (A) Conventional SS-OCT B-scan of *in vivo* tooth corresponding to the red line in Figure 2.1D, with a dark "banding" artifact indicated by blue arrows. **(B)** PS-OCT B-scan of the same region. **(C)** Phase retardation map showing changes in polarization state (angle, degrees) with depth relative to the sample surface (0°).

2.4 Discussion

The goal of this chapter was to demonstrate how commercially available OCT systems employing different light sources, imaging lenses, and detection units affect OCT imaging of dental hard tissue. These hardware components influence the achievable imaging depth, resolution, and contrast, each of which can take on different levels of

importance when using OCT for specific applications in dental imaging. From both *in vivo* and *in vitro* results, the Tel320 system provided greater imaging depth than the OQ LabScope 1.0, with an average imaging depth of 1.6 mm in sound enamel, which is more than double that of the mean imaging depth of 0.6 mm of the OQ LabScope 1.0. This greater imaging depth allows for greater visualization of the full enamel layer and the superficial dentin (**Figure 2.4**). Several factors contribute to the superior imaging depth of the Tel320, with the first being the central wavelength. Enamel is more transparent in the 1300 nm wavelength range than around 800 nm[49], enabling visualization of indications such as dentin caries[4,14], deeper cracks and restoration defects[4], as well as enamel caries such as white spot lesions[50,51]. These white spot lesions have been found to range up to 550 μm in depth based on previous studies[5]. Significant signal drop-off was observed at this depth with the OQ LabScope 1.0 system due in part to greater light attenuation (**Figures 2.3, 2.4**) at 840 nm, making the Tel320 better suited for accurately assessing such lesion depth and severity. Beyond the central wavelengths, differences in backscattered signal intensity can also be attributed to differences in incident optical power for the systems; the sample arm power of the Tel320 is more than ten times greater than that of the OQ LabScope 1.0. Additionally, the sensitivity of the Tel320 is greater than the OQ LabScope 1.0, which can also contribute to the superior imaging depth of this system for dental imaging; however, in situations requiring assessment of superficial indications, either system would be suitable. With the effects of early demineralization being limited to the most superficial surface of the enamel, quantitative analysis has been performed within the first few tens of micrometers[17,21], and often has not exceeded a depth of 150 μm[17]. As observed in **Figures 2.3** and **2.4**, the OQ LabScope 1.0 system provides sufficient imaging depth for this application, and through the use of silicon-based line-scanning detectors, this system is approximately one eighth of the cost of the Tel320, which may influence clinical uptake of OCT imaging. This system also utilizes a liquid

lens, allowing the user to simply adjust the focus with a slider in the accompanying software, which is convenient for *in vivo* imaging.

It is important to note that due to the convoluted topography of occlusal surfaces, a ranging depth spanning several millimeters could be beneficial to accommodate variations in surface height, particularly for the molar teeth. While subsurface imaging depth is primarily determined by the wavelength of the laser source, a greater ranging depth can be achieved by either increasing the spectrometer's resolution in SD-OCT, or narrowing the laser's linewidth in SS-OCT[52]. The subsurface imaging depth within tissue will remain the same, but the distance between the imaging probe and the sample surface can be greater and therefore allow for capture of subsurface structures on highly curved surfaces. Another way that some clinical OCT setups have overcome this issue of decreased signal due to natural curvature is through employment of a multi-channel setup[47], where a multi-beam sample arm probe is used to divide the depth of field into sub-fields by providing a separately focused beam for each sub-division. Typically, lateral resolution is sacrificed in order to achieve an extended depth of focus, but by utilizing such a multi-channel approach, greater lateral resolution can be attained than with a single beam setup.

In this study, lateral resolution was evaluated by using different imaging lenses in the same SS-OCT system, with the 0.15 NA lens providing greater lateral resolution than a 0.04 NA lens, allowing better visualization of enamel surface texture (**Figure 2.5**). Early enamel erosion and remineralization occur within the first few microns of tissue depth, with their effects being observed and quantified through surface assessment as demonstrated in literature through confocal microscopy analysis[53]. Using a high NA lens mimics the optical coherence microscopy technique[45], which generates images similar to confocal microscopy, thus providing multi-functional imaging with one system. While high NA

imaging was demonstrated *in vitro*, the use of such lenses was found to be impractical for *in vivo* applications due to the combination of a small depth-of-field and subject motion. Under these conditions, even small subject movements in the Z-direction caused the tooth to appear out of focus. This combined with small lateral movements resulted in a poor-quality image with blurring when attempting to reconstruct an *en face* view, though this could potentially be corrected through the use of motion-artifact correction algorithms[54]. The 0.04 NA lens, while unable to provide the resolution of the 0.15 NA lens, has lower magnification and can therefore image a larger field-of-view, providing a greater area of tissue for analysis (**Figure 2.5**). Additionally, any subject motion artifact is much less prominent with these larger area scans, and since this lens provides a greater depth of field, good quality *in vivo* volume scans and *en face* reconstructions are possible (**Figure 2.4**).

In the *in vivo* imaging situation, while the Tel320 had a higher NA compared to the OQ LabScope 1.0, the *en face* reconstruction of the OQ LabScope 1.0 contained greater motion artifacts in the form of horizontal banding due to subject motion. While both systems have similar axial scan rates (**Table 2.1**), the data transfer process while acquiring the C-scan volume is slower for the OQ LabScope 1.0 than the Tel320, so while acquisition of a volume for the Tel320 took 30 seconds, the same sized volume required approximately two minutes to complete with the OQ LabScope 1.0. This increased acquisition time and susceptibility to motion artifacts resulted in noisier reconstructions. This could be improved by using additional methods to stabilize the subject, such as the inclusion of a bite bar, or by having a spacer on the probe that is in contact with the subject to reduce movement relative to the probe. Collection of volumetric OCT data is desirable because it can be used in combination with other dental imaging techniques, such as quantitative light fluorescence, intra-oral scanning or cone beam computed tomography,

in order to provide multimodal information on the same region of tooth; image scaling, deformable registration, and fusion methods[55] would have to be implemented in order to superimpose OCT data onto another established 3-D surface generated by these other dental imaging techniques.

As seen with the conventional SS-OCT B-scans, in which signal is captured with a single detector, artificial “banding” due to enamel birefringence can affect the quality of the image, making it unclear if the loss of signal is just an artifact or due to actual tissue structure (**Figure 2.6A**). Enamel is birefringent due to the structured arrangement of the cylindrical enamel crystal prisms perpendicular to the tooth surface; this creates the phase retardation or “banding” between the two orthogonal polarization states relative to the crystal axis[56]. By using polarization-sensitive detection, two orthogonal polarization states are separately collected and then combined to produce an image without this banding artifact, providing a true representation of the enamel tissue (**Figure 2.6B**). The application of PS-OCT to dental hard tissue has been demonstrated in the literature for the assessment of demineralization[57] and remineralization[58], and it has been shown previously that using PS-OCT can enhance image contrast and can better separate the lesion body from sound enamel[27]. Such data collection also can allow for generation of phase retardation images (**Figure 2.6C**) that demonstrate the phase delay between the two polarization states. The degree of enamel birefringence can be evaluated through the frequency of banding in the phase retardation image and these PS-OCT images can provide further information on the health of the tissue beyond that which conventional OCT intensity images can provide[33].

2.5 Conclusions

This chapter presented a head-to-head comparison of two commercially available OCT imaging systems, the OQ LabScope 1.0 from Lumedica and the Tel320 from Thorlabs, a direct comparison of low vs. high system NA, and a comparison of conventional OCT vs. PS-OCT. System evaluations were completed using both *in vitro* and *in vivo* sound tooth samples. These experiments were performed to help clinicians and researchers determine which commercially available OCT configuration would be best for assessing changes in dental hard tissue structure. While the Tel320 provided superior imaging depth and axial resolution, the OQ LabScope 1.0 can provide detailed visualization of the first 500 microns of dental tissue for a fraction of the cost and provides quick and simple adjustment of focus, which can be beneficial for imaging *in vivo* and *in vitro* superficial anomalies. While both systems can generate volumetric data and *en face* views, the projection quality is reduced in the OQ LabScope 1.0 due to the longer acquisition/save time. For birefringent substrates like enamel, PS-OCT is advantageous over conventional OCT because it reduces banding artifacts and provides additional functionality through phase retardation information. Finally, higher NA lenses are preferred for observing greater contrast and improved lateral resolution, while lower magnification lenses provide greater field-of-view and are appropriate for both *in vitro* and *in vivo* use.

Chapter 3: Assessment and quantification of white spot lesion severity, treatment, and heterogeneity using optical coherence tomography

3.1 Introduction

White spot lesions (WSLs) include developmental enamel lesions, such as fluorosis, along with localized areas of demineralization/caries in both orthodontic patients as well as non-orthodontic patients[9]. Carious WSLs are rough, porous lesions that are opaque white in appearance and are the result of demineralization[9]. Non-carious (developmental) WSLs, on the other hand, are shiny and smooth in appearance and are the result of hypomineralization, fluorosis, or hypoplasia[9]. It is important to manage carious WSLs before they progress to cavitated caries, and early identification is critical for halting lesion progression through topical interventions such as fluoride and amorphous calcium phosphate[9,10]. OCT has been previously investigated for noninvasively assessing non-cavitated carious lesions[5,14,59-66]. As demonstrated in the work conducted by Ibusuki *et al.*[5], the white spot lesion appears as an area of higher backscattered intensity below an intact enamel surface in the OCT B-scan; the depth and shape of this lesion appears similar to the assessment of a cross-sectional cut under both confocal scanning light microscopy and light microscopy, suggesting that OCT may be capable of providing a full 3D evaluation of WSLs. The progression to cavitated lesions (surface breakdown) has also been tracked previously with OCT[67], while others have demonstrated that the remineralization of white spot lesions can also be observed with OCT[61], and this remineralization effect varies depending on the type of lesion (carious vs. non-carious). Together, these studies have shown that the ability to assess WSL depth is important both for grading lesion progression[67] as well as for evaluating regression due to treatment[61]. However, these studies were limited in that analysis was typically

performed on single OCT B-scans, and the methods with which lesion depth was assessed varied across studies, often exhibiting heavy user-dependence. Single 2D B-scans do not capture the 3D heterogeneity of the WSL, and therefore such analysis may not be truly representative of the entire lesion. Furthermore, *en face* (XY plane) OCT provides a coronal full structural view of enamel at different depth levels, and this may provide additional anatomic insight of various enamel conditions. Chan *et al.* used volumetric OCT data to clinically track nonsurgical intervention of surface enamel lesions[63], but due to the *in vivo* nature of the study, the accuracy of these depth values was not confirmed with a gold standard measurement.

The studies in this chapter first confirmed the ability of SS-OCT to assess white spot lesion depth and treatment effect by using artificially created lesions in bovine enamel. Based on these data, it was then hypothesized that (1) a volumetric WSL analysis method could be developed, and (2) image-based parameters that consistently quantify lesion depth and treatment effects could be established, for application to naturally occurring WSLs in intact human teeth. Experiments were conducted to acquire volumetric OCT data from natural lesions in extracted human teeth. *En face* depth maps were generated for each sample. It is hypothesized that having a full-field assessment of WSLs will allow for better understanding of lesion development and treatment compared to single B-scan analysis methods.

3.2 Artificial WSL formation assessed through OCT depth measurements

In order to identify metrics for confirming WSL formation and quantifying lesion severity, a set of bovine enamel samples were used, with an artificial lesion created on one half of each sample. From the mean OCT intensity profiles within the lesion region,

a metric for quantifying lesion severity was determined based on the depth-dependent backscattered light intensity.

3.2.1 Sample selection and preparation

For this experiment, a set of 10 polished bovine enamel samples (approximately 5 mm x 5 mm x 2 mm) were used. Baseline stereomicroscope images and OCT volumes were collected (described in detail in the sections below). Half of each sample was protected with vinyl tape to create a control or "sound" side. These samples then underwent a demineralization-remineralization cycle to create a subsurface, white spot lesion. After this cycle, the samples were rinsed, the tape was removed, and the samples were stored in deionized water in the refrigerator until post-lesion stereomicroscope and OCT images were acquired.

3.2.2 White light stereomicroscopy

To capture what the samples looked like under visual inspection, white light, cross-polarized stereomicroscope images were acquired using the system shown in **Figure 3.1**. A neutral white light LED (Thorlabs MNWHL4) was collimated using a 30 mm focal length lens (AC254-030-A) onto the fiber for the ring illuminator, and a color camera (PointGrey Grasshopper3 GS3-U3-123S6C-C) was used to capture the image. Linear polarizers were used to remove specular reflection from the polished tooth surface through cross-polarization, with a polarizing sheet (Edmund Optics) placed on the ring illuminator and a second linear polarizer (Thorlabs LPVISA050) placed before the camera lens.

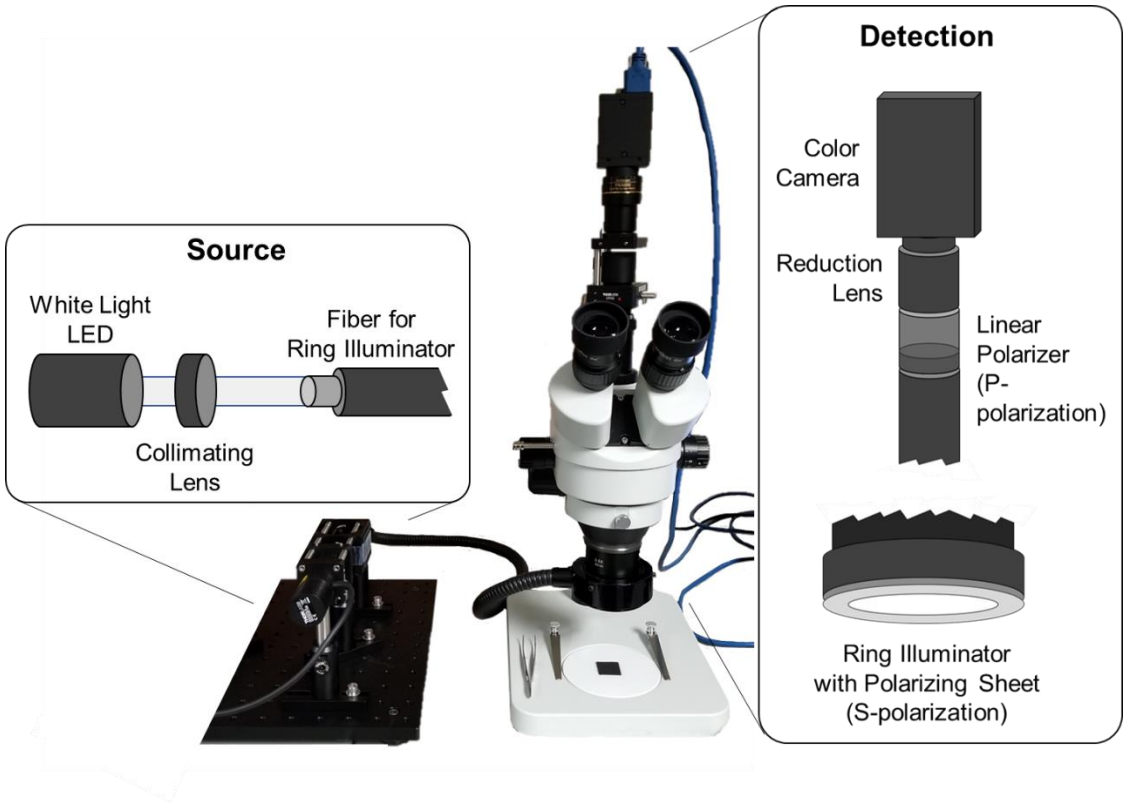

Figure 3.1 Cross-polarized white light stereomicroscope setup. The white light imager used for this study, with a white light LED used for illumination through a ring illuminator, and a set of linear polarizers to remove specular reflection. Images were captured with the color camera.

3.2.3 OCT imaging and analysis

Volumetric OCT datasets were collected, with 512 A-lines over a 7 mm wide B-scan, and 512 B-scans over a 7 mm transverse scan. The bovine samples were placed into a 3D-printed holder that tilted each sample by a few degrees about the x-axis when acquiring single B-scan images to reduce “echo” artifacts due to the strong specular reflections generated near normal incidence (**Figure 3.2A**). B-scan images were saved as 8-bit grayscale images. These B-scans were loaded into MATLAB to create volumes of XZ-views, YZ views, and XY-views. For analysis, B-scans were realigned to the sample surface and the eighth XY slice was selected for *en face* views of the samples, which corresponds to a depth of 25 microns below the surface. This just-below surface slice

was selected because it provided the greatest contrast between sound enamel and lesion. Due to the uniform nature of the artificially-created lesions, rectangular regions-of-interest (ROIs) for both sound and lesion were selected manually from these *en face* views. These selections were then automatically applied to the baseline and post-lesion volumes of B-scans to generate mean intensity profiles, with approximately 150 A-lines within 200 B-scans per ROI averaged together to reduce noise. This data acquisition and selection method is illustrated in **Figure 3.2B** and the analysis shown in **Figure 3.4A**. From these mean intensity profiles, the "lesion depth" was defined as the depth at which the slope of the intensity profile approaches a plateau, which was designated as a slope greater than or equal to -1. These lesion depth calculations were performed for both the lesion and sound regions; for the sound tissue, the depth measurement is ultimately just capturing the intact, immediate surface peak. All depth calculations are corrected with the enamel refractive index (1.6).

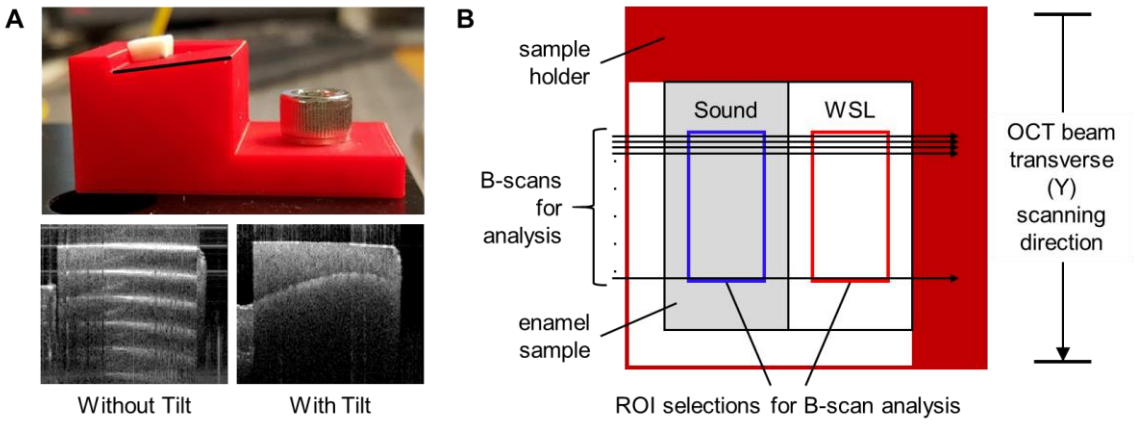

Figure 3.2 Titled holder and visualization of OCT data acquisition. (A) Side view of the titled sample holder, and the resultant OCT scans with and without tilt. (The B-scan direction is parallel to the holder's tilt axis). High specular reflection is apparent as an echo artifact when the sample is not tilted. **(B)** Birds-eye depiction of the sample holder, with the scanning direction and data selection for analysis indicated.

3.2.4 Results

The imaging results for a single representative sample (Sample 5) are shown in **Figure 3.3**. White spot lesion formation was confirmed and visualized with white light imaging (**Figure 3.3A**), OCT *en face* reconstructions (**Figure 3.3B**), and OCT B-scans (**Figure 3.3C**). As can be seen in the white light image, the lesion region has a marked color difference from the sound region, with that distinctive white color for which it is named. The lesion is also very apparent in the OCT views as higher backscattered intensity and a resultant reduced signal from below the lesion compared to the sound region.

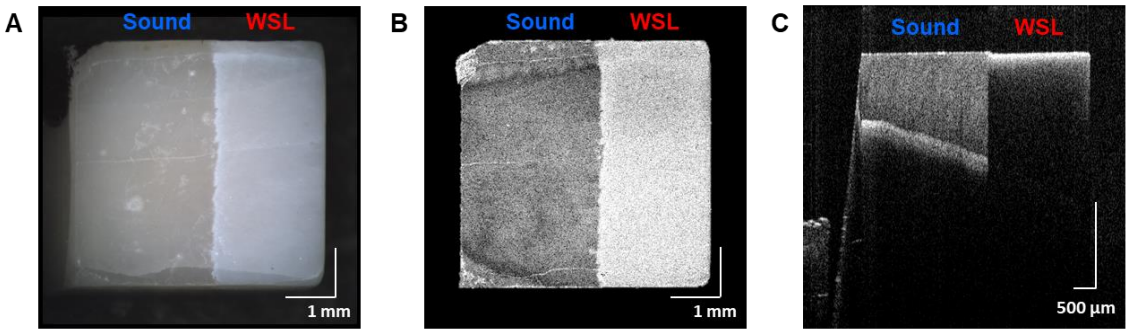

Figure 3.3 Lesion formation visualized with white light and OCT. (A) Stereomicroscope image, **(B)** *en face* OCT reconstruction of a plane just below the sample surface, **(C)** OCT B-scan of Sample 5, across the sound and WSL regions.

The results of the OCT lesion depth analysis are shown in **Figure 3.4**. **Figure 3.4A** shows the mean intensity profile for Sample 5 averaged over the 200 B-scans, with approximately 150 A-lines averaged in each region per B-scan. The starred points in this plot represent the depth calculations made with the method described in Section 3.2.3. The mean intensity profile of the lesion region up to this depth measurement is broader and of higher intensity compared to the sound enamel. The lesion severity is quite consistent across samples, with an average lesion depth of 78 µm ± 10 µm (red line in

Figure 3.4B). Sound surface depth measurements are included in **Figure 3.4B** as a reference for lesion depth values, with a mean value of 24 µm ± 3 µm. Some surface loss was noted, as can be seen in the B-scan (Figure **3.3C**), which deviates from natural WSLs in which the lesion forms beneath an intact surface.

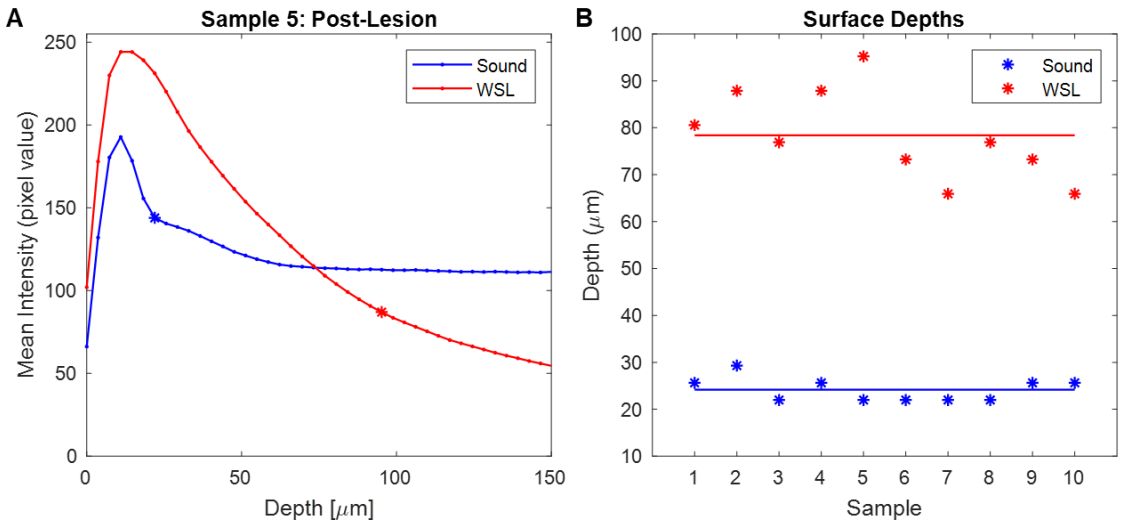

Figure 3.4 Lesion formation established through OCT depth measurements. (A) Mean intensity profile for the sound and WSL regions for Sample 5, post-demineralization. The stars indicate the measured "lesion depth", defined as the depth beyond the surface peak at which the slope of the intensity profile first becomes greater than -1. **(B)** Depth measurements for the WSL region from baseline (blue stars) and post-demineralization (red stars) OCT analysis for all samples; the solid horizontal lines represent the mean depth values for baseline (blue) and post-demineralization (red) surface/lesion depths.

3.2.5 Discussion

This artificial WSL study in bovine enamel demonstrated the capability of OCT to detect lesion formation using an automatically extracted parameter, defined as the point where the slope of the intensity vs depth profile is greater than or equal to -1. This point indicates the deep boundary of a highly backscattering region (i.e. lesion). While the lesion creation method did not create truly subsurface lesions, the OCT methodology developed above can still be implemented to assess both erosive and subsurface lesions.

These OCT results and visualization of the surface loss in this experiment allowed for modification of the sample creation methods to ensure that future white spot lesion experiments were more representative of natural lesions.

3.3 Assessment of artificial white spot lesion treatment with OCT

In this section, OCT imaging with the same analysis methods from Section 3.2 was used to assess the effect of treatment on artificially created white spot lesions. These samples each have three regions: sound enamel, an untreated white spot lesion, and a treated white spot lesion. From the OCT mean intensity profiles of each, metrics for assessing treatment efficacy and for distinguishing between the three distinct regions were investigated and established.

To confirm white spot lesion formation and treatment, quantitative light fluorescence (QLF) was included in this study. QLF is a visible light imaging method that exploits the autofluorescence of enamel by using blue excitation light and capturing the green emissions[68]. The dentin enamel junction (DEJ) is believed to be the source of the autofluorescence, with studies showing that just a small layer of dentin is needed to produce fluorescence, and removal of this dentin layer results in a complete loss of fluorescence[69]. Demineralization of the overlying enamel results in decreased fluorescence by two mechanisms: (1) the demineralized tissue causes an increase in scattering of the excitation light and therefore reduces the excitation intensity at the DEJ, and (2) fluorescence emitted from the DEJ is attenuated by backscattering on propagation through the lesion[68]. These factors lead to a clear distinction of lesion from the highly fluorescent sound enamel. As a result, QLF has been used for the detection of enamel lesions[69-71], and while studies have correlated the loss of QLF fluorescence to depth of demineralization[72], the technique does not provide direct visualization of the depth of these

lesions as OCT does. Additionally, QLF is capturing the effect of scattering variations on the fluorescence whereas OCT is directly analyzing the scattering effect[69,70,73].

3.3.1 Sample Preparation and Selection

A set of 4 polished bovine enamel samples (approximately 5 mm x 5 mm x 2 mm) were used for this pilot experiment. The sample creation method is illustrated below in **Figure 3.5**. First, one third of each sample was protected with vinyl tape to create a control or "sound" region. The samples then underwent a demineralization-remineralization process to create a white spot lesion on the remaining two thirds (**Figure 3.5A**). After the cycle, the samples were rinsed, and the tape was removed from the sound region. Half of the newly created lesion was then covered with vinyl tape in order to preserve a "lesion" region, and the samples were then exposed to a treatment solution in order to create a "repair" region (**Figure 3.5B**). After repair, the samples were rinsed and the tape was removed, and the samples were stored in deionized water in the refrigerator until imaging availability. The final result was a set of four samples, where each was split into three regions: sound, lesion, and repair (**Figure 3.5C**).

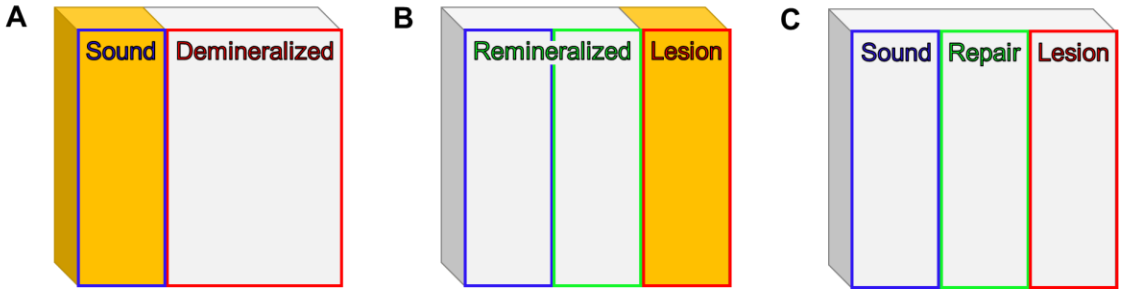

Figure 3.5 Sample creation process. (A) One third of the sample is protected with tape, while the remaining two thirds is exposed to a demineralization process to create a white spot lesion. **(B)** Half of the lesion is protected with vinyl tape to preserve a lesion region, and the remaining two thirds is exposed to a remineralization treatment. **(C)** The final result with three distinct regions: sound, lesion, and repair.

3.3.2 White Light and Quantitative Light Fluorescence Imaging

To capture the appearance of each sample under visual inspection, white light, cross-polarized stereomicroscope images were acquired using a modified version of the system shown in **Figure 3.1**. To enable this imager to perform quantitative light fluorescence (QLF) as well, a second illumination arm was added to the system (**Figure 3.6**). For white light illumination, the neutral white light LED was collimated and transmitted through a 427 nm long-pass dichroic mirror (Semrock LaserMUX LM01-427-25) onto the fiber for the ring illuminator; for QLF, a 405 nm LED (Thorlabs M405L4), further filtered with a 390/40 nm bandpass filter (Semrock BrightLine FF01-390/40-25), was collimated and reflected off the 427 nm dichroic and onto the fiber input for the ring illuminator. This setup allowed for the samples to remain in the same position, and to switch between white light and QLF, just a few short steps were taken. For the white light images, the white light LED was switched on, and the same detection configuration described in Section *3.2.2* was used. For QLF, the 405 nm LED was switched on, the polarizers were removed, and a 500 nm longpass emission filter (Thorlabs FEL0500) was inserted to capture the fluorescence of the enamel samples. This modified setup is shown below in **Figure 3.6**. For the QLF images, manual ROIs were selected, and the average green pixel value was calculated for each region to quantify the fluorescence intensity.

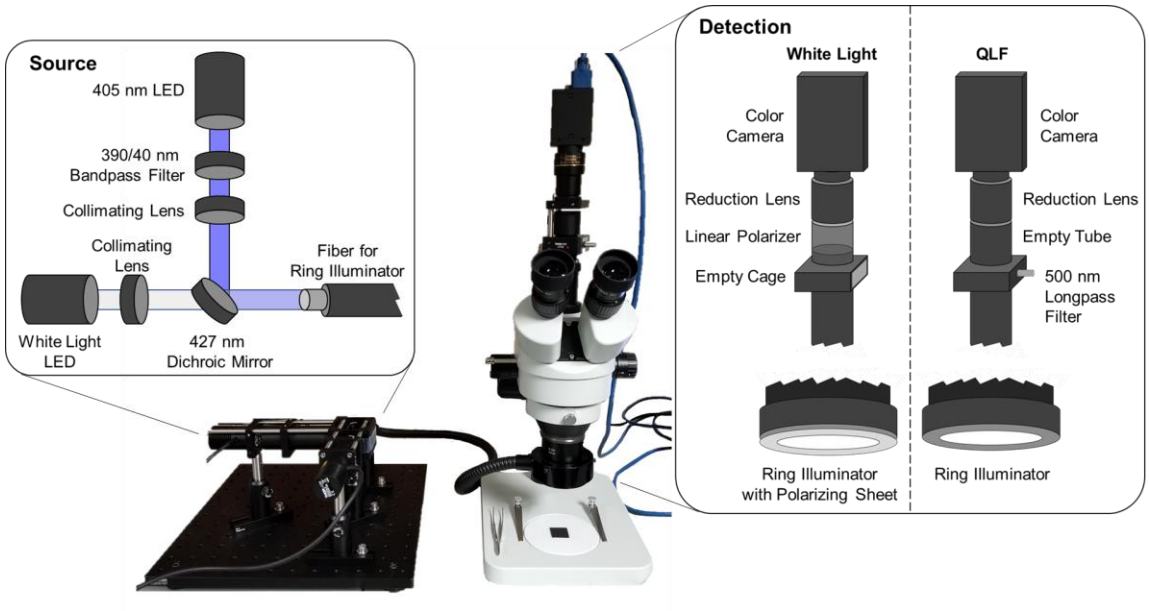

Figure 3.6 White light / QLF imager. A white light stereomicroscope was modified to allow for QLF imaging. To do so, a dichroic mirror was used to transmit most of the white light spectrum while reflecting blue light (for fluorescence excitation) into the fiber for the ring illuminator. For white light imaging, two linear polarizers were used to remove specular reflection and the image was captured with a color camera following white balancing in software. For QLF, the linear polarizers were removed, and a green emission filter was used to collect the fluorescence onto the color camera.

3.3.3 Optical coherence tomography

Just as was done in Section 3.2, volumetric OCT data sets were collected, with 512 A-lines over a 7 mm wide B-scan, and 512 B-scans over a 7 mm transverse scan. The bovine samples were placed into a 3D-printed holder that tilted each sample by a few degrees about the x-axis when acquiring single B-scan images to reduce “echo” artifacts due to specular reflection. B-scan images were saved as 8-bit grayscale images. These B-scans were loaded into MATLAB to create volumes of XZ-views, YZ views, and XY-views. For analysis, B-scans were realigned to the sample surface and the eighth XY slice was selected for *en face* views of the samples. This just-below surface slice was selected because it provided the greatest contrast between sound and lesion. From these *en face* views, rectangular regions-of-interest (ROIs) for both sound and lesion were selected

manually. The mean intensities of the ROIs were calculated from the saved *en face* views. These ROI selections were then automatically applied to the volume to generate mean intensity profiles, with approximately 150 A-lines within 200 B-scans per ROI averaged together to reduce noise.

From these mean intensity profiles, the lesion depth was calculated as the point in which the slope approaches a plateau, which was designated as a value greater than or equal to -1, as was done in Section 3.2. These lesion depth calculations were performed for the sound, lesion, and repair regions. From these plots, the area-under-the-curve (AUC) up to the depth value established in the previous step was calculated for each region and compared.

3.3.4 Results

The imaging results for all four samples are shown in **Figure 3.7**. In the white light images (**Figure 3.7A**), the lesion region is well-defined by its white color. The repair region, on the other hand, does not have that distinctive color and more closely resembles the sound region. A marked decrease in fluorescence is observed in the lesion region in the QLF images (**Figure 3.7B**), with the repair region again more closely resembling the sound enamel. For both the white light and QLF images, the distinction between the repair and sound regions is not as apparent as between lesion and sound, and lesion and repair. In the OCT *en face* reconstructions (**Figure 3.7C**), there are three clear regions, with the lesion having the highest backscattered intensity, followed by the repair region, and finally the sound region.

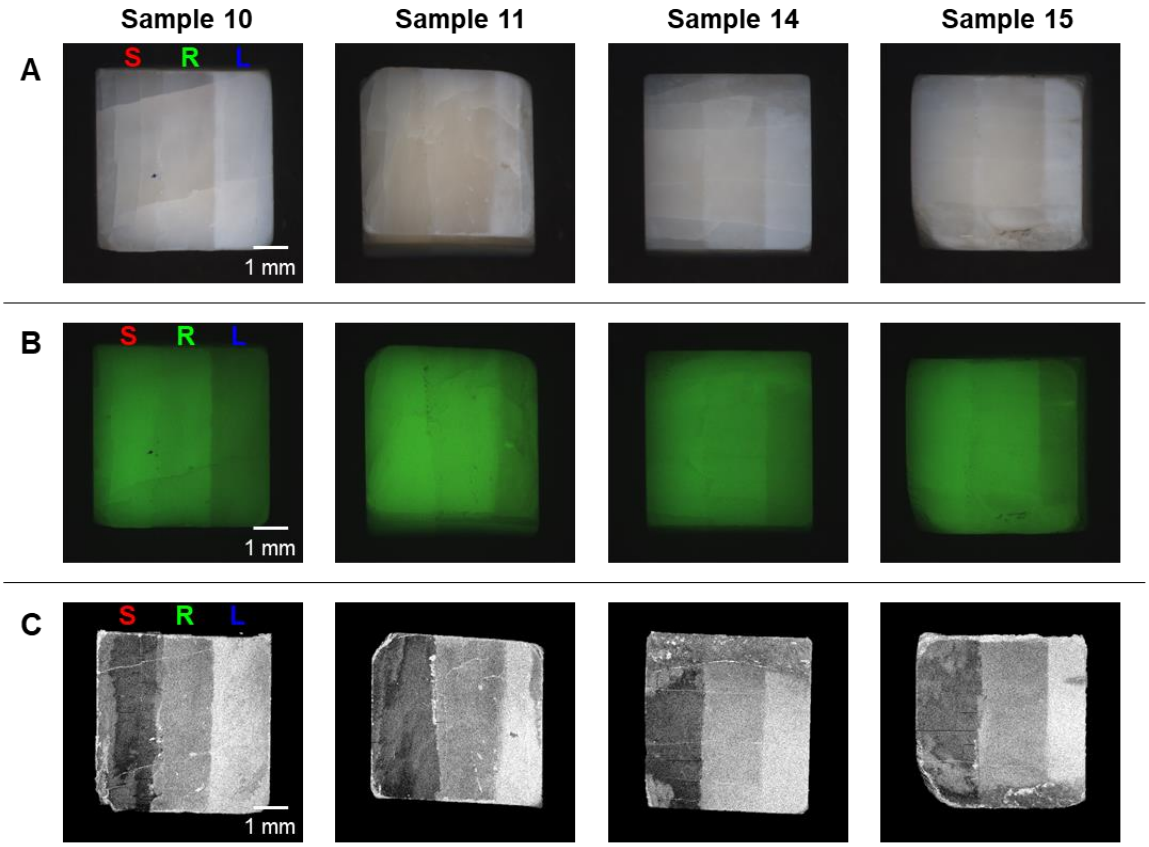

Figure 3.7 *En face* views of WSL treatment samples. Surface views of the four WSL samples with **(A)** Cross-polarized white light imaging, **(B)** QLF, and **(C)** OCT reconstructions. S = sound, R = repair, and L = lesion.

The OCT B-scans, or cross-sectional views, for two of the samples shown in **Figure 3.7** are provided in **Figure 3.8**, along with the mean intensity profiles for each region. Again, as in Section 3.2, the lesion region has hyper-reflectivity at the surface, leading to a loss of signal from within the enamel and dentin layers below the lesion. In the sound region, there is no hyper-reflectivity beneath the surface, and there is visualization of the full enamel layer and the dentin enamel junction. In the repair region, some of that sub-lesion signal is regained and the backscattered intensity at the lesion near the surface is reduced compared to the lesion region. These results are further visualized in the mean intensity profiles in **Figure 3.8**, with the lesion and repair regions

having broader and higher peaks compared to the sound region. While for Sample 10 the depth measurement can alone distinguish between lesion and repair regions, that is not the case for all samples, as demonstrated with Sample 11.

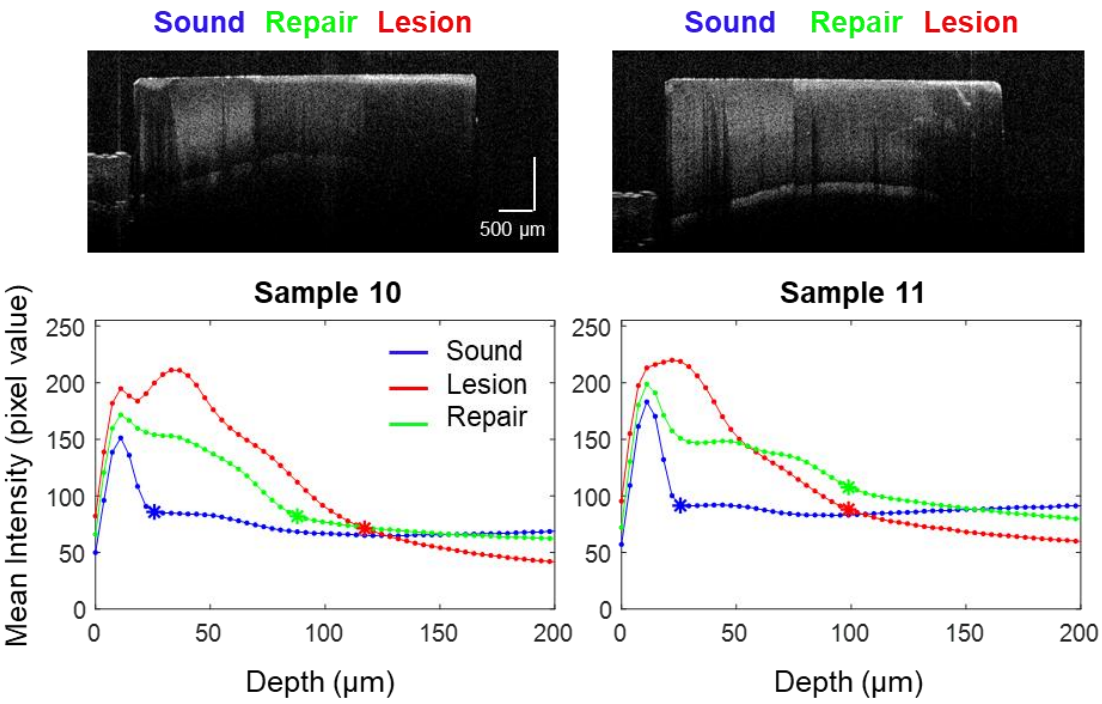

Figure 3.8 B-scans and mean intensity profiles for two WSL treatment samples. Visualization of the area-under-the-curve (AUC) calculations for the WSL samples.

To assess treatment effect, the area-under-the-curve (AUC) up to the depth measurement was calculated. This is visualized for all four samples in **Figure 3.9**, and from these plots it can be observed that the lesion region has the largest AUC, followed by the repair region, and finally by the sound region.

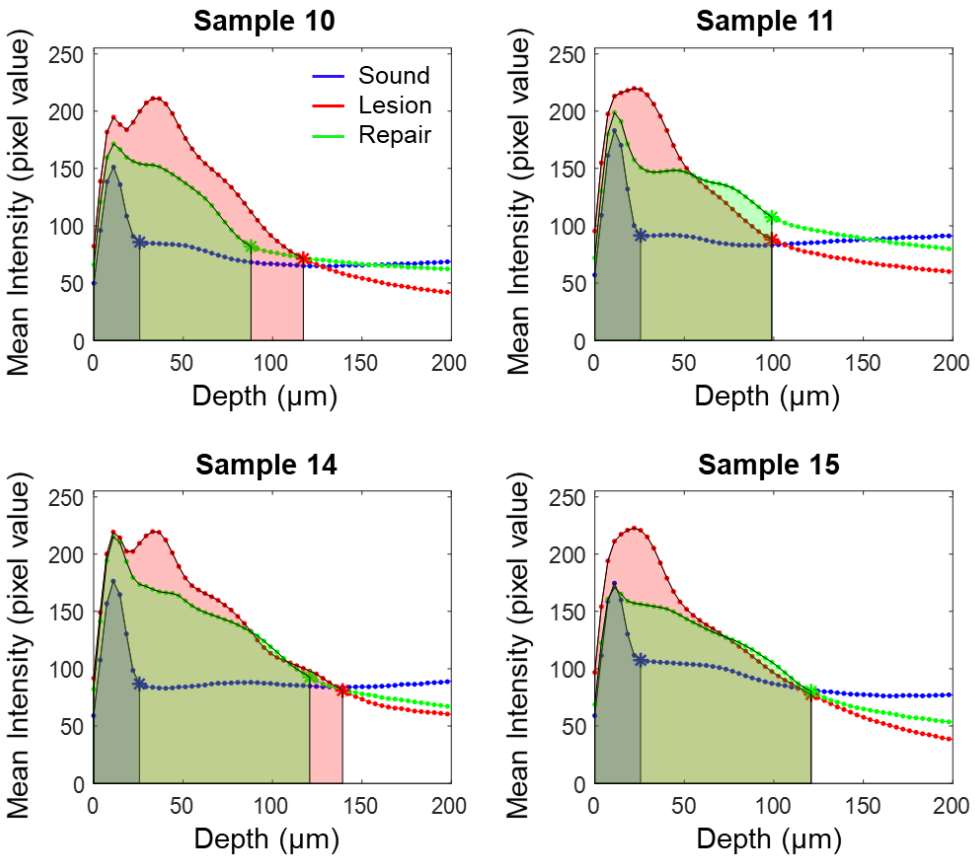

Figure 3.9 AUC plots for the WSL treatment samples. Visualization of the area-under-the-curve (AUC) calculations for each region for the WSL samples.

The quantitative results for the QLF images, the OCT *en face* views, and the AUC calculations are provided below in **Table 3.1** and plotted together in **Figure 3.10**. For each measurement type, the values were normalized to the sound value (i.e. sound = 1), and the mean value over the four samples is provided, with the error bars representing the standard deviation. For OCT intensity, OCT AUC, and QLF intensity, the repair values all exhibit a trend toward the sound value from the lesion value. With the OCT *en face* intensity results, there was a 2.3-fold increase in intensity with lesion formation, and this dropped to 1.7 with repair. Similarly, the OCT AUC lesion value decreased from a 5.4-fold increase to 4.6 with repair. With QLF, the fluorescence decreased by 0.7 with lesion formation, and with repair the fluorescence intensity returned to the sound value of 1.

Table 3.1 Quantitative results for WSL treatment samples (n = 4)

	OCT Intensity	OCT AUC	QLF Intensity
Sound	1	1	1
Lesion	2.30 ± 0.16	5.54 ± 0.85	0.66 ± 0.06
Repair	1.73 ± 0.23	4.55 ± 0.61	0.97 ± 0.06

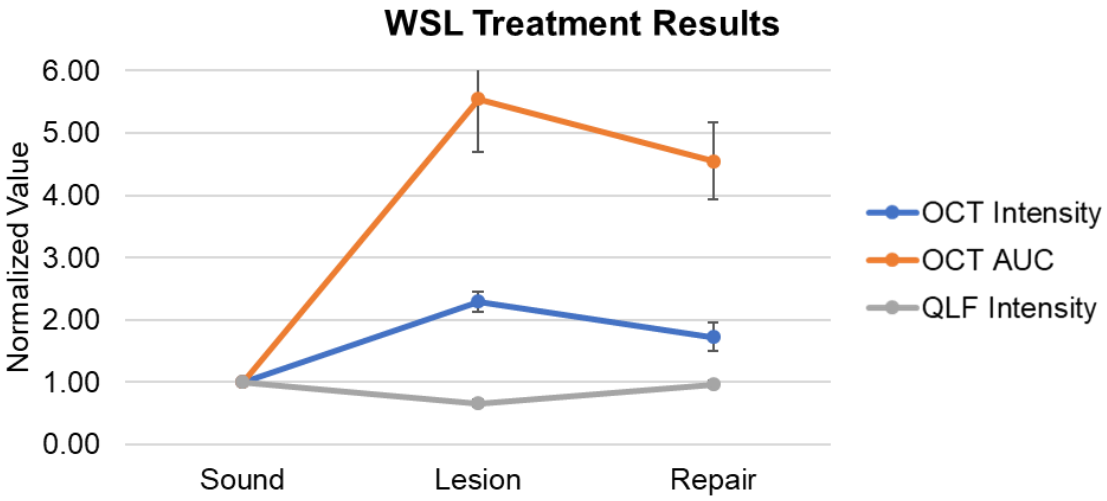

Figure 3.10 Quantitative results for WSL treatment samples. Quantitative measurements of OCT intensity, OCT AUC, and QLF intensity values, each normalized to the sound measurement. Data points represent the mean value for each group; error bars represent the standard deviation (n = 4).

3.3.5 Discussion

The findings of this pilot bovine artificial WSL study confirm the capability of OCT to detect and quantify the treatment of white spot lesions. While measurement of lesion depth alone could not distinguish repair, it provided a region in which to perform the area-under-the-curve analysis, which more robustly captures the overall intensity differences between the three regions. In previous literature[63], a similar analysis method was performed and referred to as “integrated reflectivity” over the lesion depth; in the clinical study, this metric was used to quantify lesion severity during nonsurgical intervention of smooth surface enamel lesions[63].

In this study, there was no difference in depth measurements between the lesion and repair regions for some samples; however, there was a decrease in AUC for the repair region compared to the lesion. This makes sense, as a treatment would be working from the surface down, remineralizing the lesion in the upper region first, filling in this porous lesion and causing less backscattering of incident light. This is reflected in the OCT and QLF results, with a decrease in backscattering intensity and increased signal from the depths of the tissue and an increase in the measured fluorescence, respectively. Therefore, the deep boundary of the lesion would remain the same while the above region was being repaired if the depth-of-effect of the treatment did not reach the entire lesion. This appears to be the case for this experiment.

While the QLF results indicate almost complete repair of the lesion, the OCT metrics do not suggest full repair. This could be due to several reasons, with the first being that QLF is indirectly measuring scattering through its effect on fluorescence[69,70,73], and the remineralizing agent/mechanism could be affecting fluorescence in an unexpected way that would result in discrepancies in QLF and OCT results. Additionally, repair to the lesion may not ultimately result in a return to the appearance of sound tissue for OCT. Future studies are needed to continue treatment of lesions until either full recovery or a plateau of effect in order to make firm conclusions on expected results for OCT. These types of studies are helpful for understanding mode of action for lesion repair and for establishing accurate quantitative metrics and visualization of the treatment methods. When trying to understand and quantify the depth of effect of the lesion and treatment, OCT is advantageous as it provides direct visualization of the changes in scattering in the depth of the tissue and has increased penetration depth due to the use of NIR wavelengths compared to QLF, which provides an indirect assessment of scattering through changes in fluorescence and only gives surface views of the lesion[69,70,73].

3.4 Natural white spot lesion heterogeneity and depth mapping with OCT

For the white spot lesions in the previous two sections, many A-lines and B-scans were averaged together to provide mean intensity profiles and depth measurements; this was acceptable because the artificially created lesions were quite uniform in formation and severity. Natural white spot lesions, on the other hand, have been characterized to have several different types of shapes: bowl type, layered type, and complex type[5]. The artificial lesions closely resemble the layered type of lesion, which presents as a homogenous band of increased backscattering of a certain depth[5]. The bowl type lesion has a round shape, presenting shallower at the borders and deepest in the middle, and the complex type lesion has a combination of layer and bowl shape[5]. While these various types look different in the depth of the lesion, these lesions appear largely uniform in color upon visual inspection (white light imaging) and even with QLF. Having a clinical method to observe the true depth of a lesion could be an invaluable tool to help guide clinicians in how to approach and monitor treatment. In this section, lesion depth maps were created using the entirety of the volumetric OCT scans to provide an *en face* visualization and quantification of the depth and heterogeneity of natural white spot lesions. Such a tool could allow for longitudinal tracking of lesion state (active or inactive) and progression, as well as for determining treatment efficacy and whether or not methods need to be adjusted accordingly.

3.4.1 Sample selection and imaging methods and analysis

For the assessment and depth mapping of natural WSLs, four extracted human molars with natural white spot lesions were used as samples; these lesions were confirmed visually by an experienced observer. Volumetric OCT data sets were collected with the 1300 nm SD-OCT Tel320 system described and characterized in Chapter 2, with 512 A-lines over a 10 mm wide B-scan, and 512 B-scans over a 10 mm transverse scan.

This system was chosen over the 1325 SS-OCT system used in the previous two sections because of its greater imaging depth and higher resolution. Stereomicroscope and QLF images were also taken of each sample using the setup shown in **Figure 3.6**. To confirm OCT depth measurements, micro-CT scans were acquired for each sample using the Bruker Skyscan 1272, with a pixel size (resolution) of 5.5 µm. Micro-CT imaging was used to provide a gold standard measurement of WSL depth, as was done by Espigares *et al.*[64]. The lesions appear as radiolucent in micro-CT[64], meaning there is a lack of signal (dark regions) where there is a lesion, compared to the bright surrounding sound tissue; this is the opposite of how lesions appear in OCT, where the lesion is an area of increased signal.

This process is illustrated as a flow chart in **Figure 3.11**. First, the 512 B-scans were loaded into the Volume Viewer plugin of ImageJ, and the projection view was saved; in this view, the white spot lesion is clearly identifiable. The lesion was then manually segmented in this projection view using MATLAB, and the resulting area was saved as a binary mask. To generate the depth map for each sample, the volume was analyzed B-scan per B-scan, with each row in the binary mask applying to its corresponding B-scan. The masked, realigned B-scan was then binarized with a threshold value of 0.4. This threshold was determined empirically by comparison with the micro-CT measurements. Then going column-by-column, the location of the deepest thresholded pixel was determined and the depth map (512 x 512 matrix) was updated with this value. This was done for all B-scans in the volume (rows in the depth map), and the entire map was median filtered to reduce noise and generate a final depth map. The depth map matrix values were converted from pixel number to microns by accounting for the imaging depth and refractive index of enamel (1.6). This code is provided in the Appendices. Finally, this was displayed with a false-color map to display differences in lesion depth, and this map was overlaid onto the stereomicroscope images to assist in visual orientation.

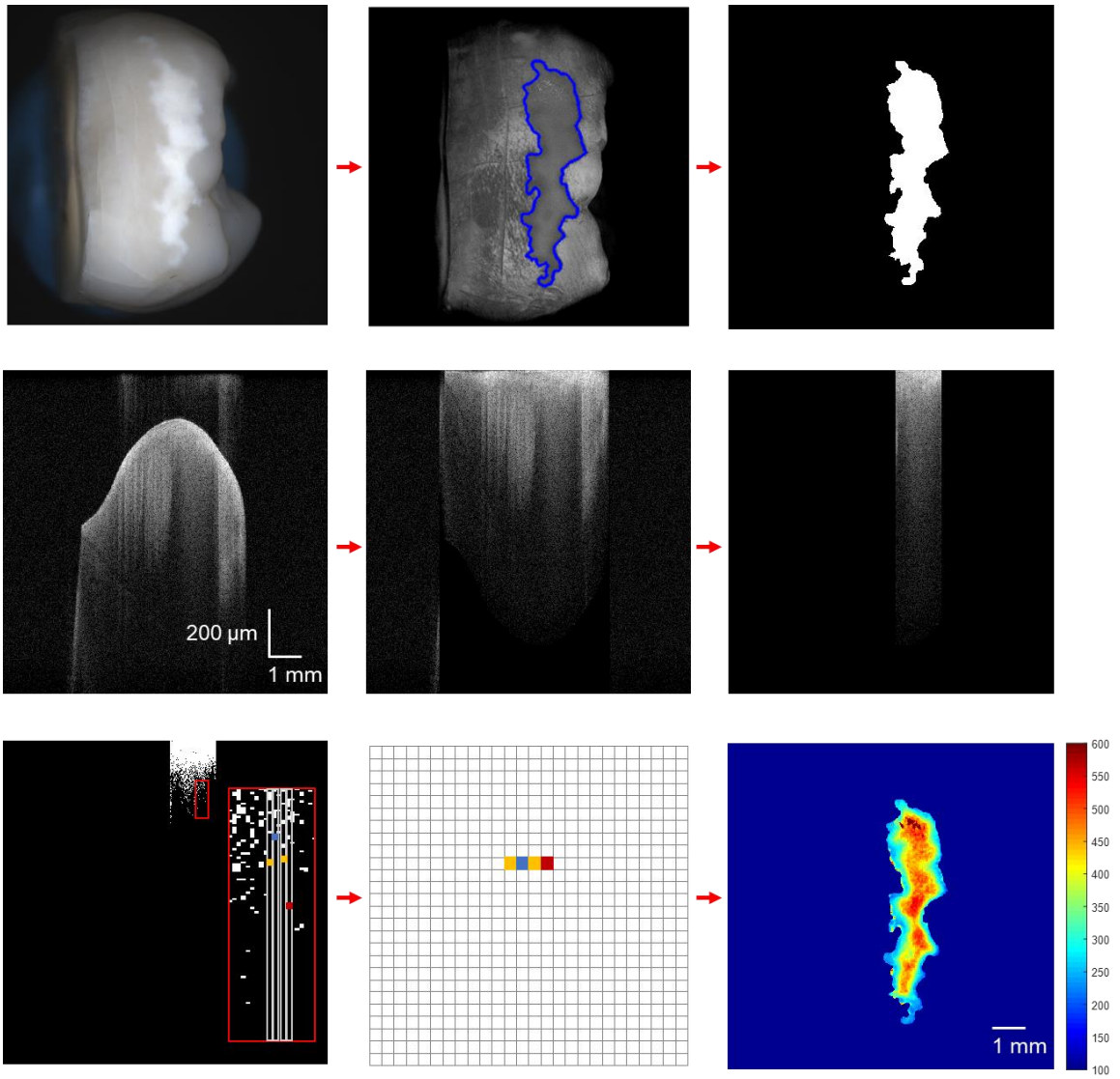

Figure 3.11 Flowchart of data analysis for OCT depth map generation. The workflow for how *en face* depths maps were generated. The lesion was manually segmented in MATLAB using the *en face* reconstruction from the Volume Viewer ImageJ plugin. This segmentation was converted into a binary mask and applied to the OCT volume, B-scan by B-scan. For each B-scan, the scan was realigned to the enamel surface, the mask was applied to the image to isolate the lesion, and the resultant scan was binarized using a threshold of 0.4. Then, column-by-column, the depth of the lesion was determined as the last white pixel in the column, and this pixel value was converted to microns. This was performed for all B-scans to generate a final, *en face* OCT depth map of the lesion.

3.4.2 Results

The white light and QLF images along with OCT reconstructions generated through the ImageJ Volume Viewer plugin are shown in **Figure 3.12A**, **B**, and **C**,

respectively. As with the artificial lesions shown in Section 3.3, the lesion is chalky white in the white light images, and there is a marked decrease in fluorescence at the location of the lesion in the QLF images. The lesions are most prominent in the QLF images. In all three views the white spot lesions are distinguishable, but depth information is not visible as there is no indication of differences in lesion severity apparent from these views.

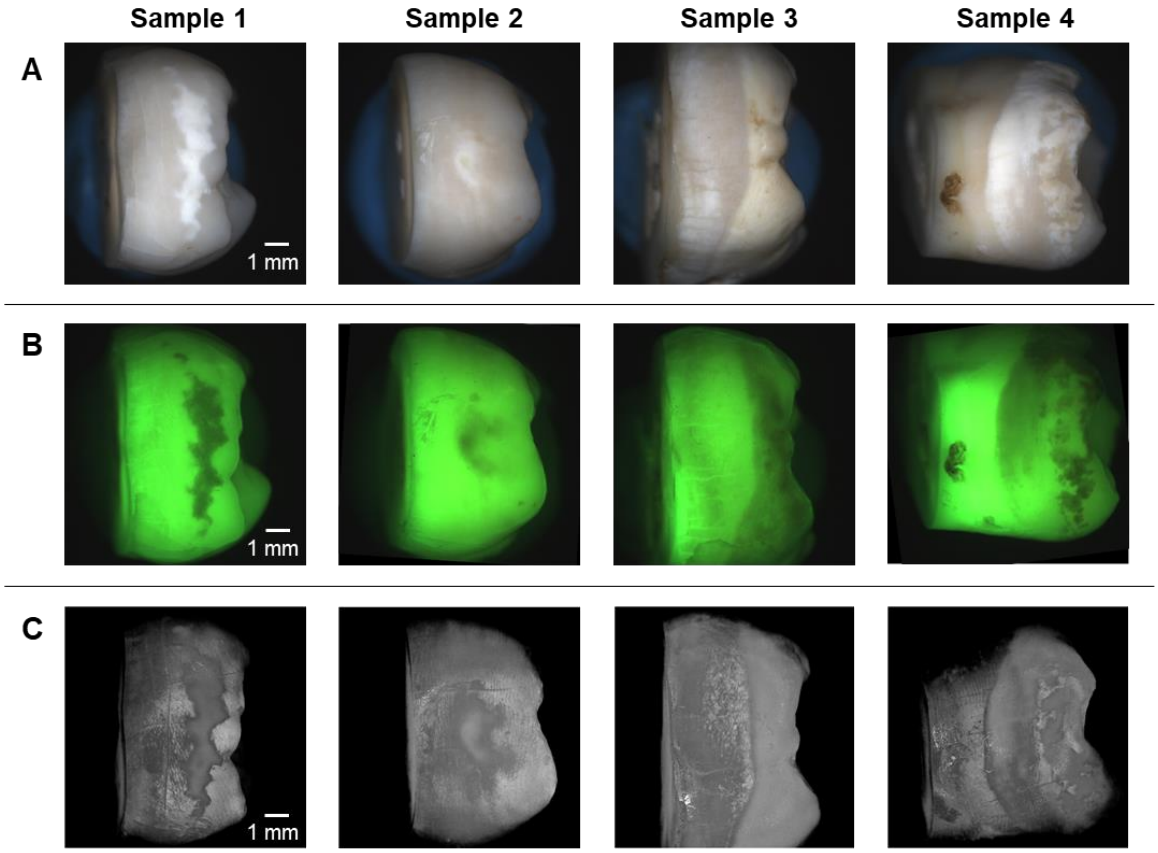

Figure 3.12 *En face* views of natural WSL samples. Surface views of the four WSL samples with **(A)** Cross-polarized white light imaging, **(B)** QLF, and **(C)** OCT reconstructions.

To determine the threshold for binarizing the OCT data for depth measurements, two samples were used to determine the threshold value, and two samples (**Figure 3.13A,D**) were used to test this threshold. Micro-CT scans (**Figure 3.13C,F**) were

compared to corresponding B-scans (**Figure 3.13B,E**) from the acquired OCT volume. This was done for multiple locations within the segmented lesion, and for two out of the four samples. The threshold was then set and applied to the OCT volumes of the remaining two samples. These depth maps were then confirmed with the corresponding micro-CT scans.

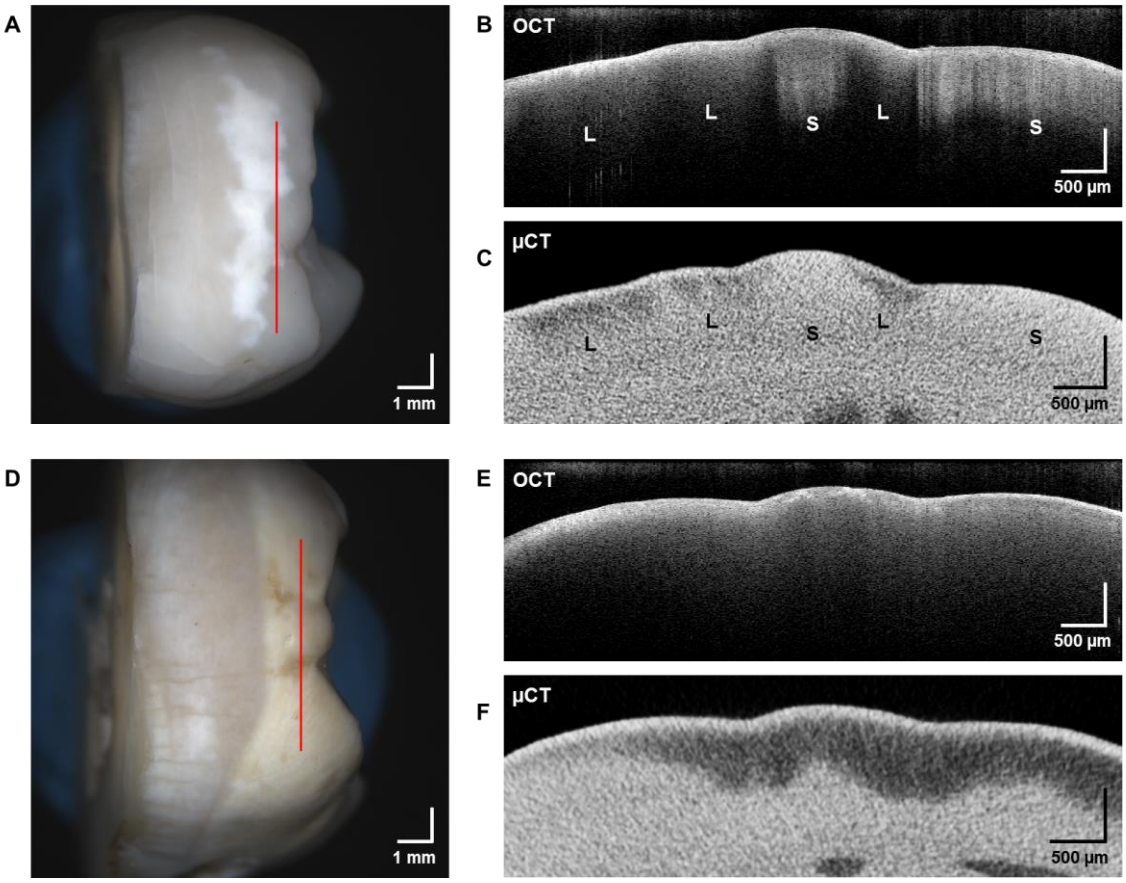

Figure 3.13 Comparison of OCT and micro-CT results for samples 1 and 3. (A,D) OCT-generated depth map overlaid onto stereomicroscope image. **(B,E)** OCT B-scan and **(C,F)** Micro-CT slice corresponding to the dashed red line in A,D. L = lesion, S = sound enamel.

The OCT-generated depth maps are overlaid on the onto the white light images for each sample in **Figure 3.14**. These depth maps showcase the heterogeneity of the

lesions both within each sample and across the four samples, with some areas measuring at around 200 µm and others up to 500 µm in depth.

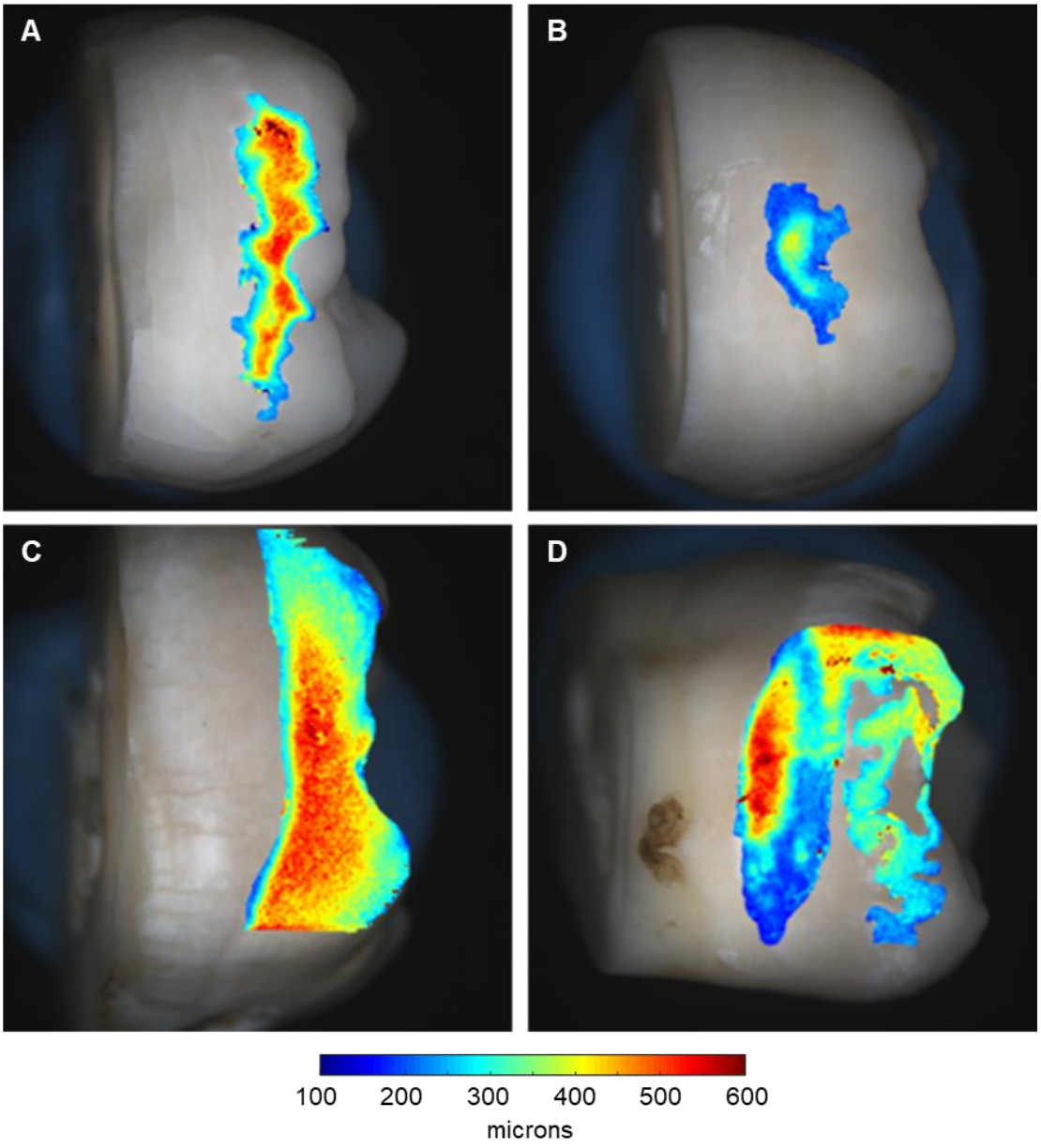

Figure 3.14 OCT depth mapping of natural WSLs. OCT-generated depth maps overlaid onto the white light images for **(A)** Sample 1, **(B)** Sample 2, **(C)** Sample 3, and **(D)** Sample 4.

A comparison of lesion depth measurements with OCT vs. micro-CT is provided in **Figure 3.15**. For this comparison, six depth measurements per lesion were sampled, for a total of 24 measurements; the OCT and micro-CT depth calculations were made at approximately the same location in the lesion for each of the data points.

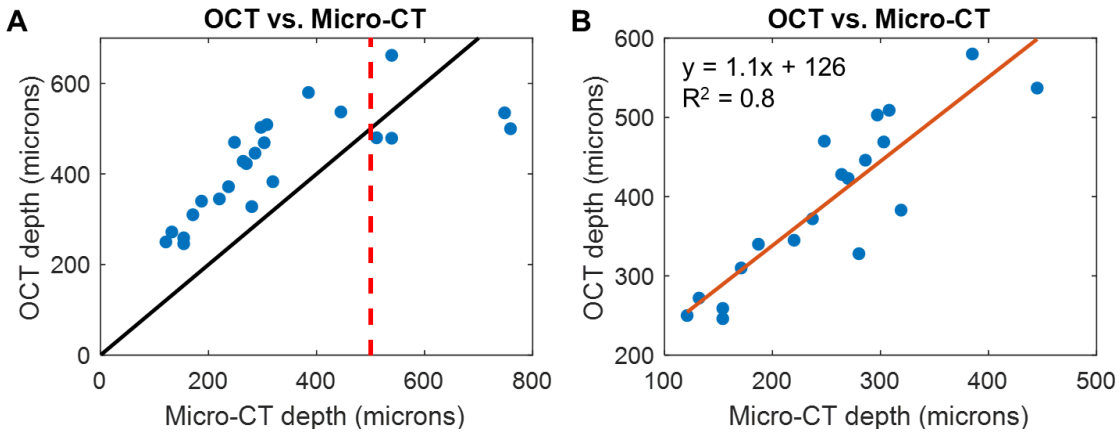

Figure 3.15 OCT vs. micro-CT lesion depth measurements for natural WSLs. A comparison of lesion depth measurements made with OCT and micro-CT results. Depth calculations were made at the same location in the lesion for each of the data points. **(A)** All data points plotted, along with the ideal result line in black. **(B)** Data points under micro-CT depth of 500 microns, and the corresponding trendline.

Figure 3.15A shows all data points in blue, and the black line indicates the ideal case where micro-CT and OCT depth measurements were perfectly equivalent. From this representation, it is clear that OCT overestimated the depth of the lesion compared to micro-CT measurements for lesion depths up to 500 µm. After 500 µm, the OCT measurements mostly underestimated the depth of the lesion when compared to micro-CT measurements. **Figure 3.15B** is a plot of all data points below a lesion depth of 500 µm in micro-CT and the corresponding trendline with a slope of 1.1, y-intercept of 126, and an R^2 value of 0.8.

3.4.3 Discussion

This work demonstrated the capability of full-field natural WSL depth mapping with OCT, a technique that can be used both *in vitro* and *in vivo* for the assessment of lesion severity as well as for treatment. The final overlaid view of the OCT-generated depth maps is helpful for orienting the observer with what is seen through visual inspection. This method also showcased the heterogeneity of white spot lesions, both within a single sample as well as across samples, with some areas being as shallow as 100 µm, and others reaching beyond 500 µm deep as measured with OCT (**Figure 3.14**). From the y-intercept of the trendline, these OCT depth measurements on average were 126 µm greater than the measurements made with micro-CT (**Figure 3.15**) using the thresholding methods described in this study. This technique is also limited in that it can only provide accurate depth measurements for lesions up to 500 µm deep; after this, the OCT measurements seemed to plateau as the micro-CT depth measurements continued to increase. Other image processing and segmentation techniques can be investigated in future work to determine if there is method that leads to more accurate depth results with OCT. Due to the maximum imaging depth of 1.6 mm in sound enamel with the SD-OCT system, depth mapping with OCT has some limitations due to the restricted imaging depth compared to what is possible with micro-CT, particularly if the lesion progresses to the dentin; however, previous studies[64] demonstrated a typical lesion depth range of about 100 to 700 µm, confirming that OCT imaging range would be adequate for typical early enamel lesions, which are of particular interest since they are more susceptible to treatments and are harder to detect with the gold standard methods of visual inspection and x-rays.

Additionally, while the OCT depth measurements may not be capturing the full effect of lesions deeper than 500 microns, they provide (1) an *en face* view that shows relative differences between lesion severity within the sample, and (2) a cutoff point for

area-under-the-curve calculations, as was done for quantifying treatment of WSLs in Section 3.3. As was seen in the previous section of this chapter, treatment effects did not necessarily result in a change in the lesion depth value, but rather the AUC decreased with treatment (**Figure 3.9**) for all samples. The AUC depth maps for the four natural WSL samples are displayed below in **Figure 3.16** and were generated using the depth measurements shown in **Figure 3.14** as the cutoff values.

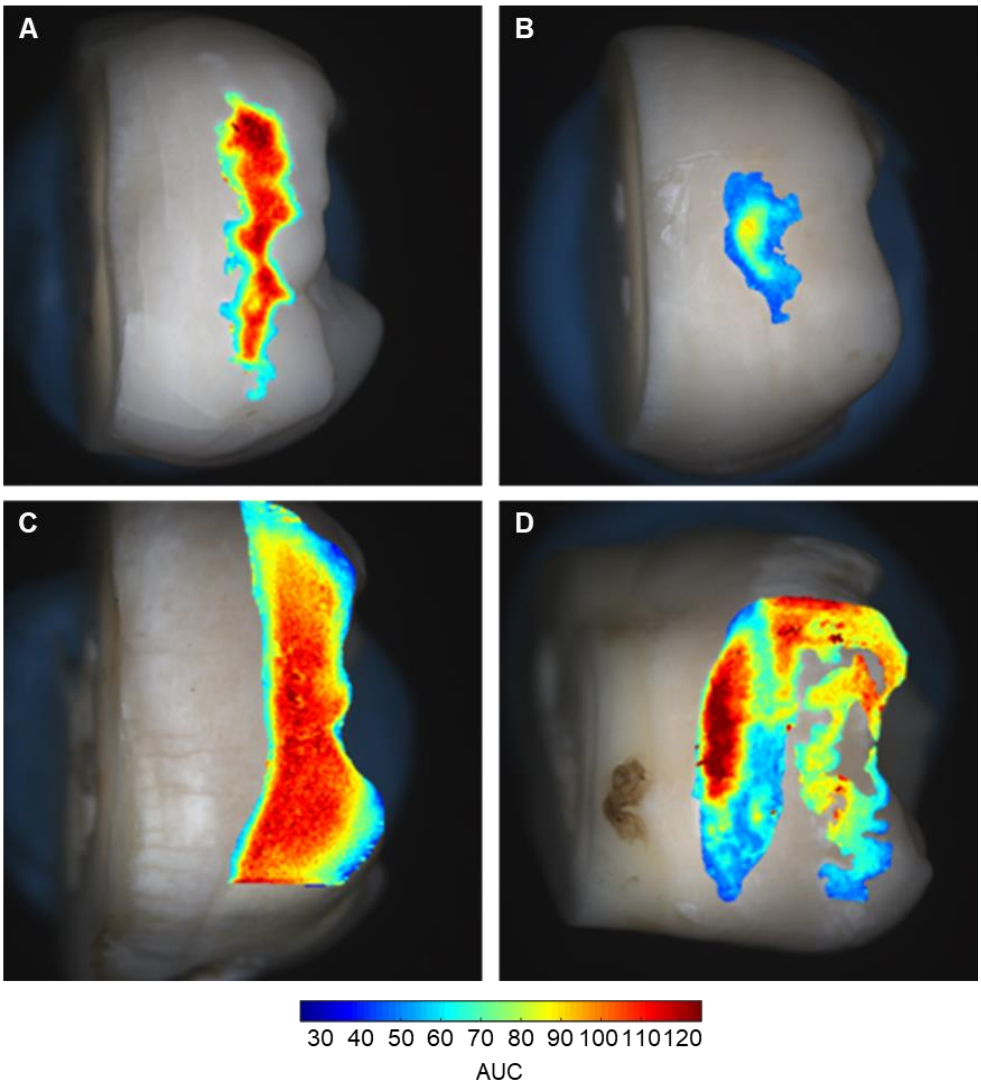

Figure 3.16 OCT AUC maps of natural WSLs. OCT-generated AUC maps overlaid onto the white light images for **(A)** Sample 1, **(B)** Sample 2, **(C)** Sample 3, and **(D)** Sample 4.

Such plots could be used in future longitudinal studies to determine and quantify effects due to treatment for natural lesions, and this can be done both *in vitro* and *in vivo* depending on the ease of access of the tooth containing the lesion. With orthodontic appliances, such as braces, contributing to an increased risk and prevalence of lesion formation[9], white spot lesions can develop on the incisors, which are easy to image *in vivo* with the typical forward-facing OCT probe configuration used in Chapter 2 (**Figure 2.1B**). For harder to access areas such as the molars, a handheld OCT probe could potentially be modified for this application.

The next steps for this work would be to (1) perform depth mapping on a more substantial cohort of samples, and (2) automate the WSL segmentation to reduce user-input and the associated errors. Having a larger sample size would allow for fine-tuning of the segmentation and depth mapping parameters to generate more accurate results, and for a greater understanding of white spot lesions to help research on developing treatment methods. More samples could also assist in the automation of lesion segmentation through machine learning, but this would require many samples (> 100) and would be a cumbersome approach. While various intensity-based methods for segmentation were investigated in this work, sample-to-sample variability made it challenging to find a group of settings that worked for all samples. Lesion contrast is greatest in the QLF image, which would make segmentation easiest, but using this view would add another layer of complexity in that the QLF and OCT views would have to be co-registered for accurate extraction results.

3.5 Conclusions

This chapter demonstrated the ability of OCT to quantify white spot lesion severity, treatment, and heterogeneity using both artificial and natural WSL samples. The bovine artificial WSL studies confirmed the capability of the OCT system to detect and quantify

lesion severity for enamel white spot lesions using an automatically extracted parameter lesion depth. While the depth measurement alone could not distinguish repair, it provided a region in which to perform the area-under-the-curve analysis, which captured the overall intensity differences between the three regions. The OCT and QLF results reflected a "top-down" treatment effect, with a decrease in backscattering intensity and increased signal from the depths of the tissue and an increase in resultant fluorescence, respectively for non or less demineralized tissue. While the QLF results indicated almost complete repair of the lesion, the OCT assessment method provides a more robust and accurate assessment of lesion treatment mode of action and efficacy. Full-field lesion depth and AUC mapping with OCT was also demonstrated in this chapter with the natural WSL study. The final overlaid views of the OCT-generated depth and AUC maps (**Figures 3.14** and **3.16**, respectively) showcased the heterogeneity of natural white spot lesions, both within a single sample as well as across samples, ranging between 200 and 500 μm in depth as measured with OCT. These natural lesions are much more severe than the artificially created lesions, which had an average depth of around 80 μm. This discrepancy could have implications in treatment efficacy differences between artificial and natural lesion studies.

OCT can directly visualize the subsurface dental tissue and allow for true quantification and assessment of the depth of effect, as demonstrated in this chapter, with an imaging technique that can be used both *in vitro* and *in vivo* for point-of-care assessment of lesion severity and treatment. OCT cross-sectional scans appear markedly different from the radiographs clinicians are familiar with viewing. In order to ensure successful clinical uptake of OCT, training would have to be available to provide dentists with the tools they need to effectively identify lesions with this unfamiliar imaging modality.

Chapter 4: Short-wave Infrared Spatial Frequency Domain Imaging for Quantification of Water and Lipid Content

4.1 Introduction

Spatial frequency domain imaging, or SFDI, is a non-contact imaging technique that works by illuminating a sample with spatially modulated light and measuring the diffusely reflected light, the magnitude of which depends on (i) the optical properties of the sample (absorption and reduced scattering coefficients), and (ii) the spatial frequency of the projected pattern. By measuring the diffuse reflectance under illumination with different spatial frequencies, the absorption and scattering coefficients of the sample can be determined. Since these optical properties vary with wavelength, taking measurements at multiple wavelengths provides the overall absorption spectrum of the tissue sample. This spectrum can then be treated as a linear combination of the major tissue chromophores, such as oxy-hemoglobin, deoxy-hemoglobin, water, and lipid, allowing absolute concentrations of each component to be determined.

The majority of the current SFDI literature describes systems operating in the VIS/NIR wavelength range, focusing on absorption effects due primarily to oxy- and deoxy-hemoglobin, which then enables parameters such as blood oxygen saturation and total hemoglobin concentration to be extracted. This capability has been used in clinical applications such as preoperative mapping for carcinoma removal[74], tumor resection[75], burn wound severity[76], and pressure ulcers[77]. The current state of SFDI has been recently reviewed by Gioux *et al.*[38].

While oxy- and deoxy-hemoglobin have absorption peaks in the visible and near-infrared wavelength ranges, other tissue components such as water and lipid have distinctive absorption peaks in the short-wave infrared (SWIR) range[78,79], as seen in **Figure 4.1**. The ability to quantify water content has significance for conditions such as

edema, burns, and wound healing, and can also have significance in oral health for conditions such as dry mouth and gingival inflammation.

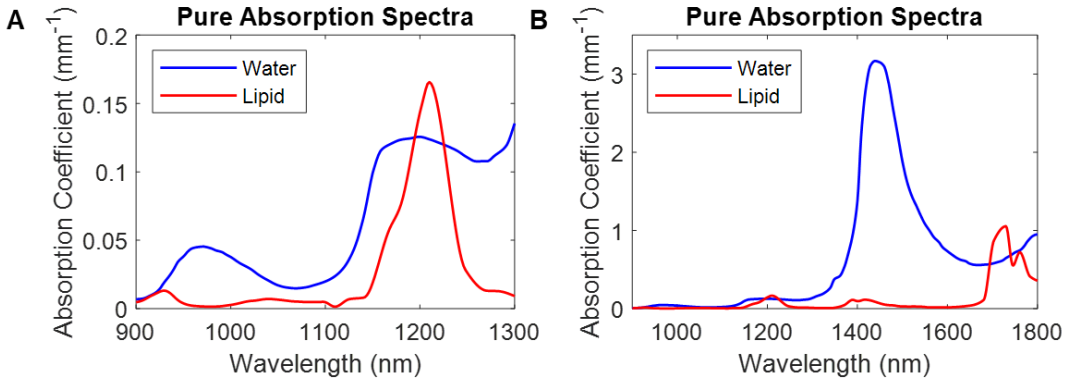

Figure 4.1. Absorption spectra of pure water and lipid. The absorption spectra for pure water[78] and pure lipid[79], showing distinct absorption peaks in the SWIR region. The absorption peaks near 1,450 nm and 1,700 nm (B) are much stronger than those in the 900 – 1,300 nm region (A).

Previous literature on implementing SFDI at SWIR wavelengths conducted by Wilson *et al.* combined VIS/NIR SFDI data with planar imaging at SWIR wavelengths in order to provide absorption maps at 1,350 nm[41], since water absorption is greater than other constituents at this wavelength (**Figure 4.1B**). True SFDI data was collected in the VIS/NIR range between 850 and 1,050 nm to determine absorption and reduced scattering coefficients, and then the μ_s' data were extrapolated over the 1,100 – 1,800 nm SWIR range[41]. These extrapolated reduced scattering values were then used along with the planar illumination images to extract absorption maps[41]. Assessment of the absorption maps generated for the 1,350 nm data showed greater absorption in skin following a controlled burn injury compared to pre-burn tissue, which was attributed to increased water content due to edema[41]. There appears to be only one report directly performing SFDI at SWIR wavelengths for the extraction of water and lipid content, but this work is based on hyperspectral imaging within the 900 – 1300 nm range to extract chromophore

concentrations[80]. In this chapter, a SWIR-SFDI system is constructed and its configuration is investigated for the direct quantification of water and lipid content. A pair of illumination wavelengths that allows for the most accurate extraction of these chromophores was predicted through condition number analysis and simulated data, and these theoretical results were then confirmed with *in vitro* experimentation. Accurate measurement of the main tissue chromophore concentrations including water can be of great importance for assessing oral soft tissue, i.e. gingivitis and dry mouth.

4.2 Wavelength optimization for chromophore extraction

SFDI requires multispectral measurements in order to extract chromophore contributions, and the more wavelengths used, the more accurate the results; however, this increases both the image acquisition and processing time. Work has been done in the visible-NIR range to determine the optimum pair of wavelengths that can be used to extract oxy- and deoxy-hemoglobin concentrations[39,81]. In this section, the same approaches used for wavelength optimization with VIS-NIR SFDI systems are applied to the extraction of water and lipid concentration with SWIR-SFDI. Determining the minimum set of illumination wavelengths required for accurate chromophore measurement will enable development of compact, cost-efficient instrumentation, simplify data processing, and allow for measurements to be taken in a fraction of the time. These factors are all important for *in vivo* applications when capturing physiological events and trying to minimize errors from motion artifacts[39].

4.2.1 Condition number analysis

As just mentioned, chromophore concentrations can be determined through absorption measurements made by SFDI. The overall optical absorption of a sample at a

single wavelength, λ_i, can be described as a linear sum of concentration-dependent contributions from individual chromophores[39]:

$$\mu_a(\lambda_i) = \sum_{n=1}^{N} \varepsilon_n(\lambda_i) c_n \tag{4.1}$$

where μ_a is the sample's absorption coefficient, $\varepsilon_n(\lambda_i)$ is the extinction coefficient of chromophore "n" at a designated wavelength, λ_i. c_n is the chromophore concentration, and N is the total number of chromophores being considered. If measurements of a sample's absorption coefficient are taken by SFDI at multiple wavelengths, and the extinction coefficient matrix is obtained from pre-existing literature, each chromophore concentration can be determined through the following matrix equation[39,81]:

$$\begin{bmatrix} \mu_a(\lambda_1) \\ \vdots \\ \mu_a(\lambda_j) \end{bmatrix} = \begin{bmatrix} \varepsilon_1(\lambda_1) & \cdots & \varepsilon_N(\lambda_1) \\ \vdots & \ddots & \vdots \\ \varepsilon_1(\lambda_j) & \cdots & \varepsilon_N(\lambda_j) \end{bmatrix} * \begin{bmatrix} c_1 \\ \vdots \\ c_N \end{bmatrix} \tag{4.2}$$

with N representing the number of chromophores and j being the number of measured wavelengths. In order to separate chromophore concentration values, the condition $j \geq i$ must be met. The contribution of each chromophore c_n to the overall absorption is proportional to the "smoothness" of the singular-value distribution of the coefficient matrix[81] in equation 4.2. The smoothness of the extinction matrix is measured as the condition number, $\kappa(\varepsilon)$, which is defined as the ratio of the maximum and minimum singular values (SVD) of the matrix[39,81]:

$$\kappa = \frac{SVD_{max}}{SVD_{min}} \tag{4.3}$$

A small condition number indicates that the singular vectors have similar contributions from each chromophore, while a large condition number means that the measurements are considerably more sensitive to some chromophores over others[81].

Therefore, a low condition number indicates that the system of equations represented by equation 4.2 is well-conditioned, i.e. their solutions are relatively insensitive to errors on the input values (measured tissue absorption coefficients)[39]. All possible wavelength pairs in the range of 1100 – 1700 nm were analyzed to determine the wavelength pair with the lowest condition number, for extraction of water and lipid concentration with SWIR-SFDI.

4.2.2 Simulated physiological data

In addition to condition number analysis, the optimal wavelength pair can be determined through simulation of physiological data. For this analysis, 292 water-lipid concentration pairs in the physiological range (16.6 – 100% for water, and 40 – 80% for lipid)[82-84] were generated to create pairs ranging from 40% lipid, 60% water to 80% lipid, 20% water. For each pair, the corresponding absorption coefficient was calculated using absorption spectra for pure water and lipid, then Gaussian noise with zero mean and a standard deviation of 1% of the absorption value was added to mimic *in vivo* measured data. Then for each of these simulated measurements of absorption, the water and lipid concentrations were predicted by solving equation 4.2 for each wavelength pair in the range of 1100 – 1700 nm. The percent error for both water and lipid concentration estimation were calculated for each wavelength pair. This was done for all 300 water-lipid pairs. The extraction error was then determined as the standard deviation of the percent errors for each wavelength pair. To provide an overall extraction error that incorporates both chromophores of interest, the water and lipid extraction errors were combined as the square root of the sum of the squared individual error values.

4.2.3 Instrumentation and in vitro measurements

A SWIR-SFDI system was constructed using a SuperK EXTREME supercontinuum laser (NKT Photonics, Denmark) with the SuperK SELECT multi-channel

tunable filter. The filter unit contains two acousto-optic tunable filters (AOTFs), providing output into two separate single-mode fiber-coupled channels. The system used here was equipped with one AOTF covering the wavelength range from 500 – 900 nm, with an output bandwidth of 3.5 – 14 nm, and a second AOTF covering the 1100 – 2000 nm wavelength range with an output bandwidth of 6.4 – 19.8 nm. The output from the second AOTF channel was collimated with a 100 mm focal length lens (Thorlabs, AC254-100-C-ML) onto a digital micromirror device (DMD) (DLP LightCrafter 6500 EVM, Texas Instruments, Dallas, TX). The DMD is an array of individually controllable mirror elements that can be used for SFDI pattern generation, but this structure also has 2D diffractive properties that must be addressed when a coherent or partially coherent light source is used[85]. The location of the diffracted orders is dependent on incident angle, grating (mirror) pitch, and wavelength[85]; if the incident angle and pitch are held constant, then the order locations will be different based on which wavelength of light is used. Since this study involves a wide range of wavelengths (1100 – 1700 nm), the diffraction orders will not be captured by the projection optics for all wavelengths. Therefore, the incident angle must be changed with wavelength in order for light to be collected and relayed to the sample plane. To do this, the laser fiber and collimation optics were mounted on a rotation stage to allow for the incident angle to be easily changed with wavelength so that each wavelength diffracted off the DMD at the same angle and illuminated the sample plane at the same location. For the longer wavelengths, the entire illumination arm needed to be translated as well in order to properly illuminate the DMD. Adjustment of the incident angle for the different wavelengths allowed for the imaging optics and camera to remain unchanged for all measurements. The DMD was used to generate three phase-shifted (0°, 120°, 240°) sinusoidal patterns of spatial frequencies 0 mm^{-1} (DC) and 0.1 mm^{-1}, which were focused onto the sample plane with a 50 mm focal length, 1-inch diameter lens (Thorlabs, AC254-50-C-ML). This spatial frequency combination is frequently used in the

literature for VIS/NIR SFDI[86,87]. Samples were illuminated with wavelengths in the SWIR range of 1100 nm to 1700 nm, selected by the computer controlled AOTF. The diffuse reflectance from the sample plane was captured with a 1280x1024 pixel InGaAs camera (UTC Aerospace Systems, GA1280JS), which is sensitive to wavelengths in the range 900 – 1700 nm, and a 25 mm fixed focal length, f/2.1 SWIR lens (Edmund Optics, 83-160). A pair of orthogonal linear polarizers (Thorlabs, LPNIR050-MP2) was used in the illumination and imaging paths to reduce collection of specular reflection from the sample surface. This setup is shown in **Figure 4.2**.

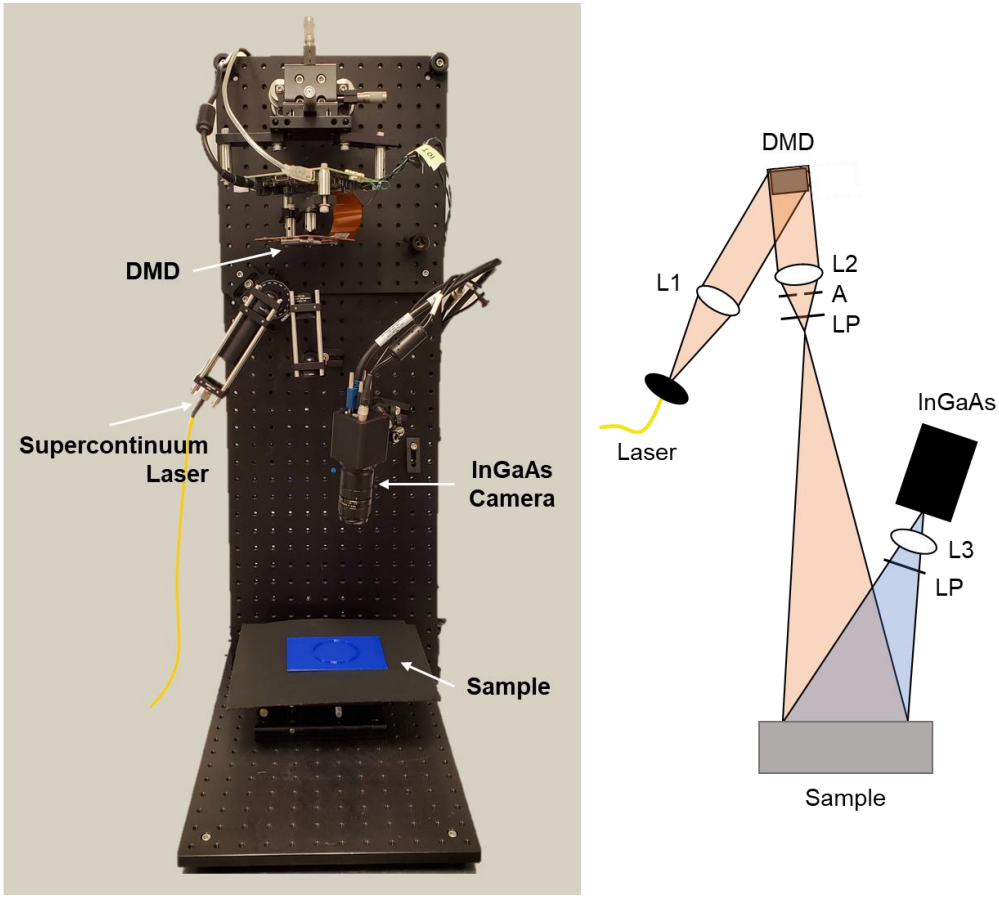

Figure 4.2. The SWIR-SFDI system. The supercontinuum laser was collimated and directed onto the DMD, which was used to project sinusoidal patterns onto the sample plane. Diffuse reflectance from the sample was captured with the InGaAs camera. L1 = 100 mm focal length lens. L2 = 50 mm focal length lens. A = aperture. LP = linear polarizer. L3 = 25 mm focal length camera lens.

The setup is controlled with LabView code that allows for the capture of the three spatially modulated images at each spatial frequency. Exposure times of 50 – 150 ms were used for data acquisition depending on the wavelengths used due to signal differences; the exposure time was kept as a multiple of the inverse of the DMD refresh rate (for 8-bit patterns, the pattern rate can be up to 247 Hz). In order to convert measured pixel values (12-bit, 0-4095) into absolute diffuse reflectance values (0-100%), and subsequently determine absorption and reduced scattering coefficients, a sample with known optical properties at the illuminating wavelengths was used for calibration. A 10% Intralipid phantom (10% lipid, 90% water) was used, with absorption and scattering coefficients from 1100 nm to 1700 nm determined from the pure spectra and experimentally derived equations available in the literature[88,89]. Spectralon standards with known diffuse reflectance under planar illumination were imaged with the system to test the accuracy of this calibration for planar (DC) illumination. The accuracy of the subsequent step of calculating optical properties from diffuse reflectance measurements using look-up tables (LUTs) generated through Monte Carlo simulations was tested using the 10% Intralipid calibration phantom as the sample. These LUTs are four-dimensional and consist of predicted diffuse reflectance values for samples over a range of absorption and reduced scattering values at the two specific spatial frequencies used. Once the diffuse reflectance is measured at the two spatial frequencies with the SFDI system, the LUTs are used to estimate the absorption and reduced scattering values that would produce those diffuse reflectance values.

To test the wavelength optimization analyses detailed in Sections 4.2.1 and 4.2.2, the concentrations of 5%, 10%, 15%, and 20% Intralipid titrations were determined with a few wavelength pair combinations selected from the optimization analysis, some with low predicted error, and some with high predicted error.

4.2.4 Results

Results from the condition number analysis and simulated data analysis are shown in **Figures 4.3A** and **B**, respectively. From these results, the wavelength pair with both a low condition number and a low chromophore extraction error is the 1200/1300 nm wavelength combination (white asterisk in **Figure 4.3**). This pair provides a condition number of 2.62 and an extraction error of 3.01% through simulation.

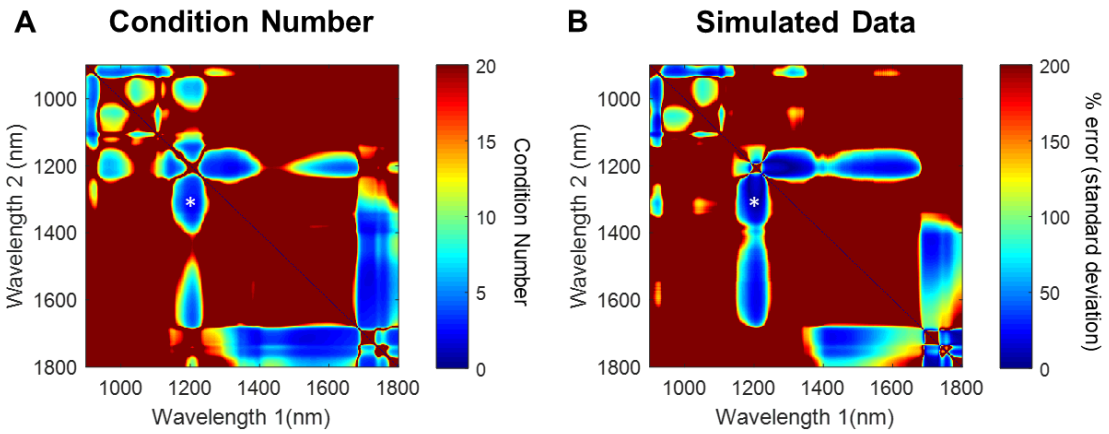

Figure 4.3. Wavelength optimization results. (**A**) Condition number analysis results, and (**B**) simulated data analysis results for the SWIR wavelength range of 900 – 1800 nm. White asterisk indicates the 1200/1300 nm pair where condition number and extraction error are lowest.

The simulation results were tested experimentally with the SWIR-SFDI system at a few select wavelengths within this range: 1200, 1300, 1450, 1550, and 1650 nm. For each water-lipid sample (80:20, 85:15, 90:10, 95:5), the concentrations of each component were estimated and the percent error for both water and lipid was calculated for each wavelength pair, as was done with the simulated data analysis. The extraction error was then determined as the standard deviation of the percent errors for each wavelength pair. To provide an overall extraction error that incorporates both chromophores of interest, the

water and lipid extraction errors were combined as the square root of the sum of the squared individual values.

The experimental results for all possible combinations of the five chosen wavelengths are shown in **Figure 4.4A**, with the same wavelength combinations from the simulated data analysis shown in **Figure 4.4B** for ease of comparison. From these results, the 1200/1300 nm wavelength combination provided the lowest extraction error both experimentally and in simulation. While the experimental extraction error is lower than the theoretical, the same trends are observed, where the 1200/1300 nm combination provides the lowest error, followed by the 1200/1650 nm, then the 1200/1550 nm, and finally the 1200/1450 nm pair. All other combinations provide very high extraction error (> 600%) for both the experimental and theoretical results. Discrepancies in the actual error values could be due to the differences in lipid/water ranges used for each; for experimental data, the error is calculated for samples ranging between 5% lipid / 95% water to 20% lipid / 80% water, while the theoretical calculations are based on samples ranging from 40% lipid / 60% water to 80% lipid / 20% water.

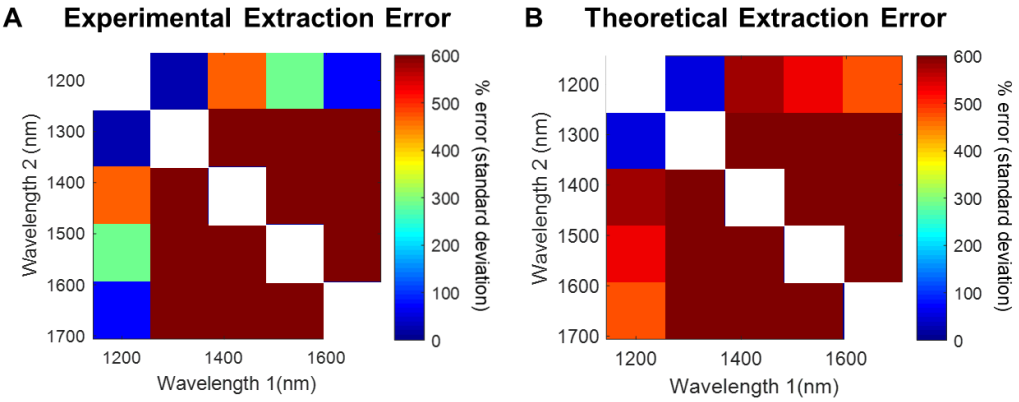

Figure 4.4. Experimental extraction error results. Extraction error calculated as the standard deviation of percent error for all Intralipid titrations at each wavelength pair, for (**A**) experimental data and (**B**) simulated data. The diagonal squares are where the two wavelengths are the same, which is not a feasible combination since the number of wavelengths must be greater than or equal to the number of chromophores in order to solve Equation 4.2 and extract concentrations.

The results for the extracted water and lipid concentrations for this wavelength combination are shown in **Figure 4.5A** and **4.5B**, respectively. As can be seen from these plots, the measured values (black asterisks) are close to the expected concentrations for water (blue) and lipid (red) for the Intralipid titrations, with a mean percent error of 1.7% for water and 31.3% for lipid extraction.

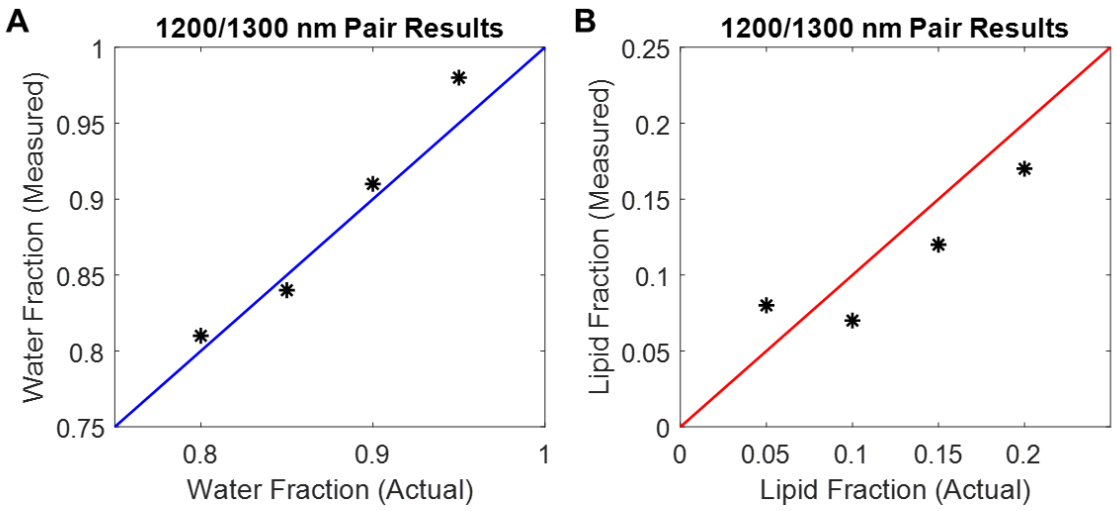

Figure 4.5. Experimental concentration extraction for the 1200/1300 nm pair. Extracted concentration of **(A)** water and **(B)** lipid for the 5%, 10%, 15%, and 20% Intralipid titrations. The blue and red lines are the expected results for water and lipid concentration, respectively. The black asterisks are the measured data points.

Since the 1200/1300 nm wavelength combination provided the lowest extraction error in this initial test, additional data were collected with a finer wavelength increment near this range. For the second round of data collection, SFDI measurements were taken from 1200 to 1400 nm in 10 nm increments, as well as at 1210 nm due to the presence of a lipid absorption peak at this wavelength. As was done in the first round of analysis, an extraction error map was calculated and is compared to the theoretical, simulated analysis results in **Figure 4.6**.

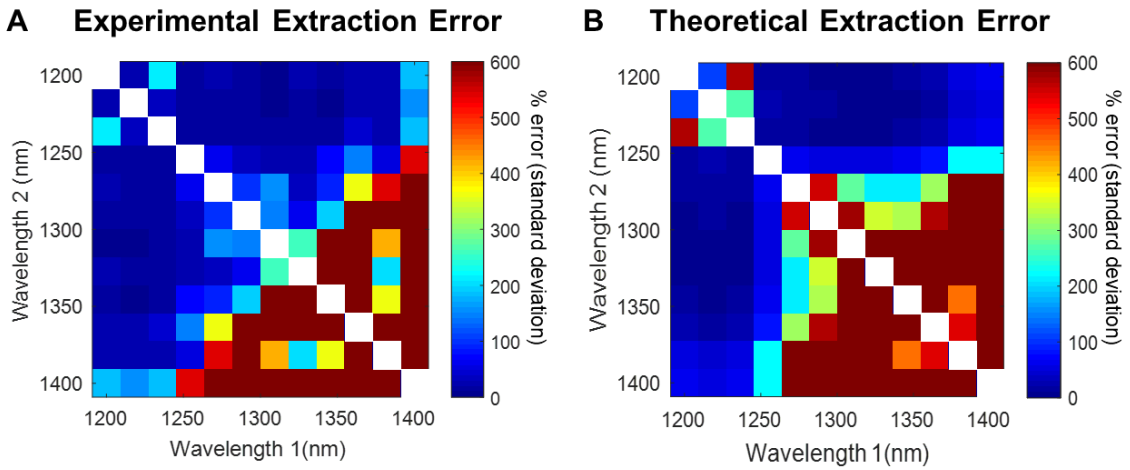

Figure 4.6. Experimental extraction error for all wavelength pairs between 1200 and 1400 nm. Extraction error calculated as the standard deviation of percent error for all Intralipid titrations at each wavelength pair, for (**A**) experimental data and (**B**) simulated data.

These results demonstrate that using one wavelength between 1200 – 1220 nm in combination with a second wavelength in the 1240 – 1340 nm range will provide concentration estimates with low extraction error. The combination of 1200 nm with 1220 nm provides a high extraction error because the absorption values of water and lipid are approximately equivalent at these wavelengths, as seen in **Figure 4.7**. The ideal combination includes a wavelength in which the lipid absorption is higher than water, and a second wavelength in which the water absorption is higher than that of the lipid.

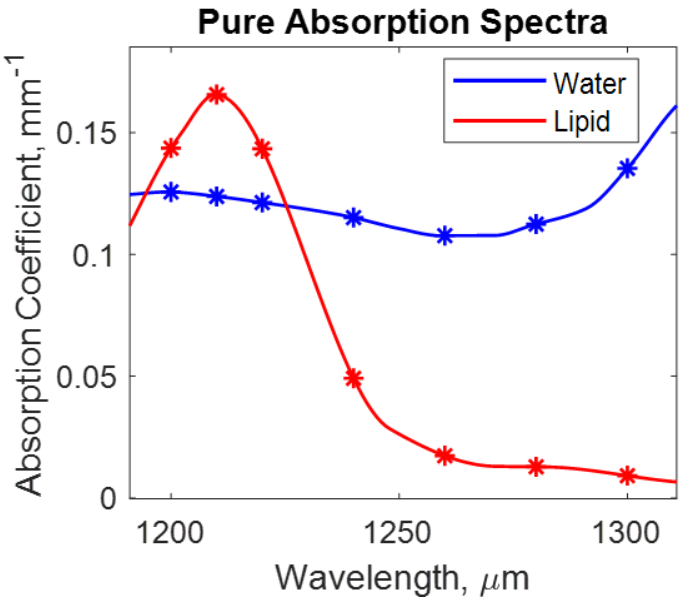

Figure 4.7. Pure lipid and water spectra in the 1200 – 1300 nm wavelength range. Absorption of water and lipid is approximately the same at 1200 nm and 1220 nm, which leads to high extraction error.

4.2.5 Discussion

As determined through the simulated condition number and wavelength analysis results, illumination with wavelengths longer than 1350 nm results in high condition numbers and high extraction errors for measuring water and lipid content (**Figure 4.3**). This is attributed to the fact that the measurements at these wavelengths are considerably more sensitive to water over lipid due to the significantly greater water absorption up to around 1700 nm (**Figure 4.1B**). For the 1200/1300 nm pair, one chromophore does not significantly overpower the other at these wavelengths (**Figure 4.1A**), resulting in a low condition number and low extraction error. The experimental results support the simulated results, with the 1200/1300 wavelength pair providing concentration extractions with the lowest error, with a mean percent error of 1.7% for water extraction, and 31.3% for lipid extraction. The measured extraction error was high for all other wavelength-pairs. The high water absorption of the 10% intralipid results in a very low diffuse reflectance

measurement for calibration; the expected R_d values for the 10% Intralipid phantom for the 0 mm^{-1} and 0.1 mm^{-1} spatial frequencies were determined by putting the absorption and reduced scattering coefficients of the 10% Intralipid into the LUT and are shown in **Figure 4.8**.

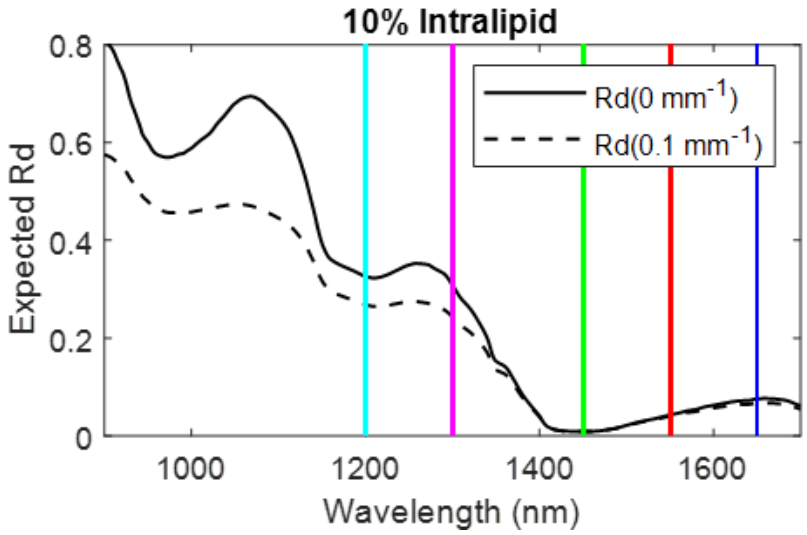

Figure 4.8. Theoretical diffuse reflectance of 10% Intralipid for the 0 mm^{-1} and 0.1 mm^{-1} spatial frequencies. The diffuse reflectance is particularly low at the 1450 nm wavelength.

Even with the laser power at a maximum, the signal measured from 10% Intralipid is very low/close to camera background levels, which makes the calibration particularly sensitive to noise and unreliable. This is confirmed by the measurements of Spectralon reflectance standards shown in **Figure 4.9**. The measured diffuse reflectance for these standards is accurate for 1200 nm and 1300 nm but significantly underestimates the true diffuse reflectance values for the 1450 nm wavelength, indicating poor calibration at this wavelength. With the current laser, higher illumination intensities are not possible at these longer wavelengths, and there are limitations to increasing exposure time with the InGaAs camera due to the high dark current of these cameras.

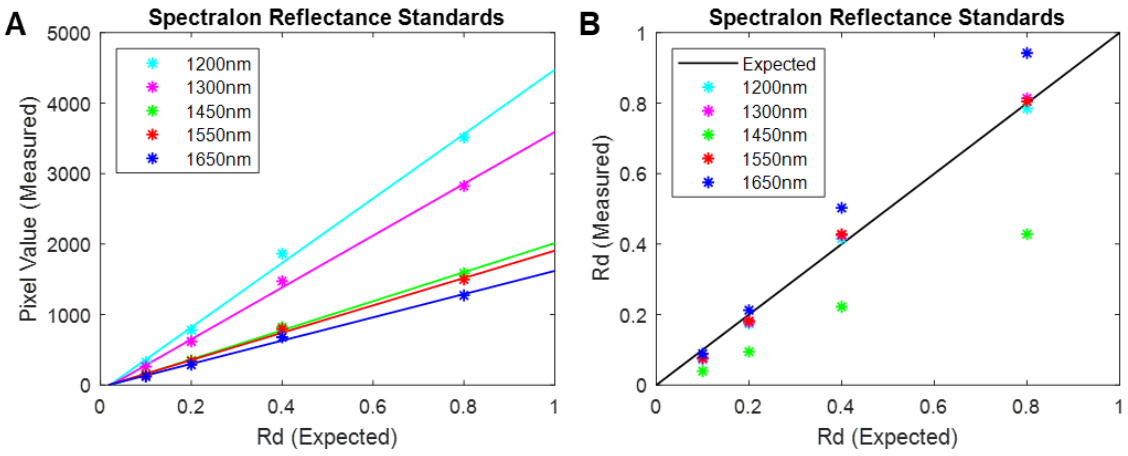

Figure 4.9. Measured camera pixel values (0-4095) and diffuse reflectance (0-1) for Spectralon reflectance standards for calibration with 10% Intralipid. (A) Measured pixel values and (B) measured diffuse reflectance values for 10%, 20%, 40%, and 80% reflecting Spectralon standards at 1200, 1300, 1450, 1550, and 1650 nm. The expected measurements are indicated by the black line.

To further test if the calibration phantom is a source of error for the 1450 nm and 1650 nm results, one of the Spectralon standards was used as the calibration phantom rather than the 10% Intralipid. This was done using the 20% reflecting standard (**Figure 4.10A**) and the 40% reflecting standard (**Figure 4.10B**). With this calibration, there is better agreement for the 1450 nm and 1650 nm results with both cases, and the measured diffuse reflectance is closer to the expected values with the 40% reflecting standard than with the 20% reflecting standard. These results indicate that accurate R_d calculations are obtained when calibration is performed with a sample that has significant signal (i.e. greater R_d) at the investigated wavelengths. Such findings motivate the need for a better calibration phantom for the longer wavelengths, where the diffuse reflectance will provide calibration images that have adequate signal above background and are less susceptible to noise. Intralipid has also been found to vary from batch to batch and can become moldy

and lumpy with time after opening, so it would be preferable to have a more stable calibration phantom with a less finite shelf life.

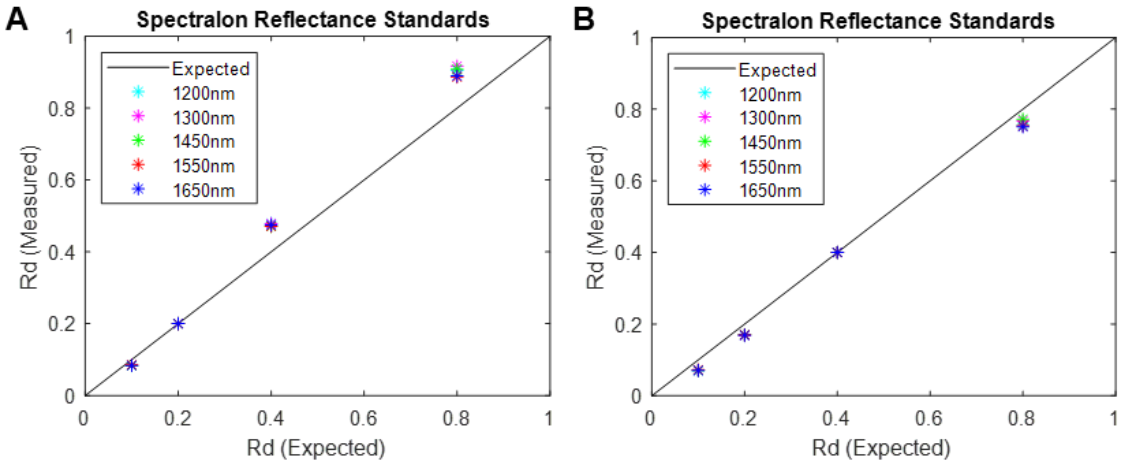

Figure 4.10. Measured diffuse reflectance for Spectralon reflectance standards for calibration with reflectance standard. Measured diffuse reflectance values for 10%, 20%, 40%, and 80% reflecting Spectralon (RS) standards at 1200, 1300, 1450, 1550, and 1650 nm **(A)** when calibrated with the 20% RS and **(B)** when calibrated with the 40% RS. The expected measurements are indicated by the black line.

While wavelength optimization is crucial for accurate chromophore extraction, there are other aspects of SFDI acquisition and processing that can be optimized in order to improve concentration extraction, such as spatial frequency selection and use of accurate extinction coefficients for the pure chromophores of interest. These areas will be investigated in the next two sections of this chapter.

4.3 Optimization of calibration source data for chromophore extraction

The accuracy of the pure extinction spectra of water and lipid is another important factor that can introduce errors in chromophore concentration measurement. These values are used in two important steps of the SFDI process: (1) for predicting the diffuse reflectance of the 10% Intralipid calibration phantom, and (2) for calculating chromophore

concentrations from the measured absorption coefficients for the sample. Concentration extraction errors will be compounded if these values are not accurate and representative of the pure chromophore components (water and lipid). There are several sources for water and lipid absorption and extinction spectra available in the literature. In this section, the use of different combinations of literature values is investigated for the extraction of water and lipid content in Intralipid titrations. The values that provide the lowest errors in estimation of water and lipid content are identified. For this study, two water spectra[78,90] and two lipid spectra[79,91] were used for calibration and chromophore concentration extraction. The data from these sources are compared graphically in **Figure 4.11**.

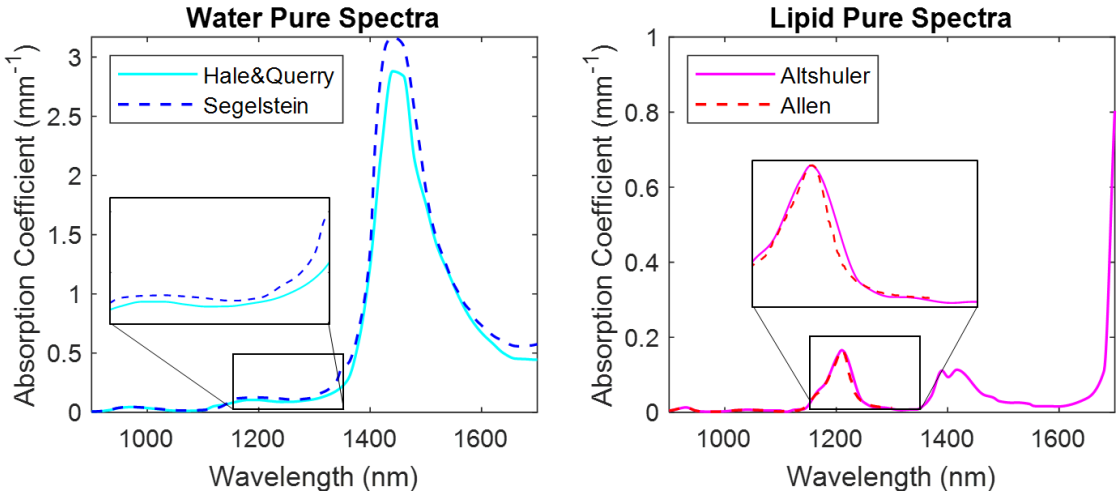

Figure 4.11. Comparison of pure spectra from different studies. Water absorption spectra from Hale & Querry[90] and Segelstein *et al*.[78]. Lipid absorption spectra from Allen *et al.*[91] and Altshuler *et al.*[79].

SFDI processing was performed using the four possible combinations of these spectra for the 1200/1300 nm wavelength pair data, and the extracted concentrations of water and lipid were compared (**Figure 4.12**). The difference in lipid / water extraction results arising from use of these different source spectra was found to be minimal. The Segelstein *et al.* water spectra[78] in combination with the Altshuler *et al.* lipid spectra[79]

provided the most accurate results with the lowest error for both water and lipid extraction, with a mean extraction error of 1.7% for water and 31.3% for lipid. It is worth noting that these findings apply to the 1200/1300 nm wavelength combination, where the source spectra are very similar (insets of **Figure 4.11**). There may be greater differences if SFDI calculations were made at wavelengths where the source spectra have larger differences (i.e. 1450 nm).

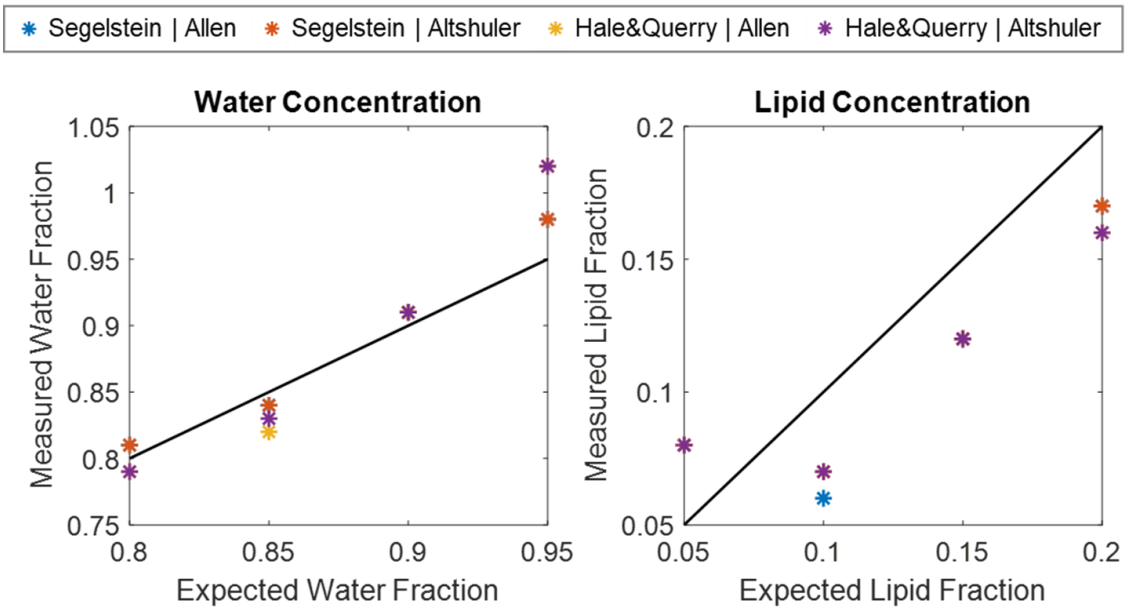

Figure 4.12. Experimental results for water and lipid concentration extraction using absorption/extinction coefficients from different literature sources. Water and lipid fractions were determined for (5/95, 10/90, 15/85, and 20/80) Intralipid / water titrations using the 1200/1300 nm wavelength pair and a 0 + 0.1 mm^{-1} spatial frequency pair. Results are shown for the four combinations of available absorption and extinction coefficients from the literature.

4.4 Spatial frequency optimization for chromophore extraction

For SFDI operating in the VIS/NIR range, most reports in the literature use the spatial frequency combination of 0 mm^{-1} (DC) and 0.1 mm^{-1}. Mainly, lower spatial frequencies (including 0 mm^{-1}) are sensitive to both absorption and scattering, whereas higher spatial frequencies are primarily sensitive to scattering and probe shallower tissue depths[86,92].

Tabassum *et al.* investigated the selection of spatial frequencies to establish a frequency pair that accurately extracted oxy- and deoxyhemoglobin for *in vivo* tumor monitoring[86]. To determine the optimal spatial frequency pair, the DC frequency (0 mm^{-1}) was paired with a second, higher AC spatial frequency, and each combination was compared over a physiologically relevant range of optical properties for the wavelength range of interest[86], which covered a μ_a range of 0.003 to 0.055 mm^{-1}, and a μ_s' range of 0.5 to 3 mm^{-1}. For tissues with optical properties in these ranges, the ideal spatial frequency pair was determined as 0 and 0.1 mm^{-1} and the resulting look-up table was relatively evenly distributed. However, other spatial frequency combinations led to optical property isolines collapsing on each other, which made the extraction of optical property pairs highly sensitive to even small errors in either of the two diffuse reflectance measurements[86].

To-date, there has been no published research on how these LUTs perform in the SWIR wavelength range, where tissue absorption due to the presence of water and lipid can significantly exceed the range encountered at VIS/NIR wavelengths studied by Tabassum *et al*[86]*.* In this section, the use of different spatial frequency pairs is investigated to establish the ideal pair for accurate extraction of absorption and reduced scattering at SWIR wavelengths. The same SFDI setup described in Section 4.2.3 was used, and sinusoidal patterns of spatial frequencies 0 mm^{-1} (DC), 0.1 mm^{-1}, 0.2 mm^{-1}, and 0.4 mm^{-1} were projected onto the sample plane. Spectral data was taken at the same wavelengths as the previous sections: 1200, 1300, 1450, 1550, and 1650 nm, and the same phantoms containing 5, 10, 15, and 20% Intralipid (95, 90, 85, and 80% water) were used.

4.4.1 Results

SFDI analysis was performed for four different spatial frequency combinations: DC (0 mm^{-1}) combined with 0.1 mm^{-1}, 0.2 mm^{-1}, 0.3 mm^{-1}, and 0.4 mm^{-1}. The extracted absorption coefficients for the different spatial frequency pairs for each Intralipid titration

are compared to the expected values in **Figure 4.13** below. For each titration, these expected values were calculated as the water fraction multiplied by the pure water absorption coefficient plus the lipid fraction multiplied by the pure lipid absorption coefficient for the wavelength range of 900 – 1700 nm[89].

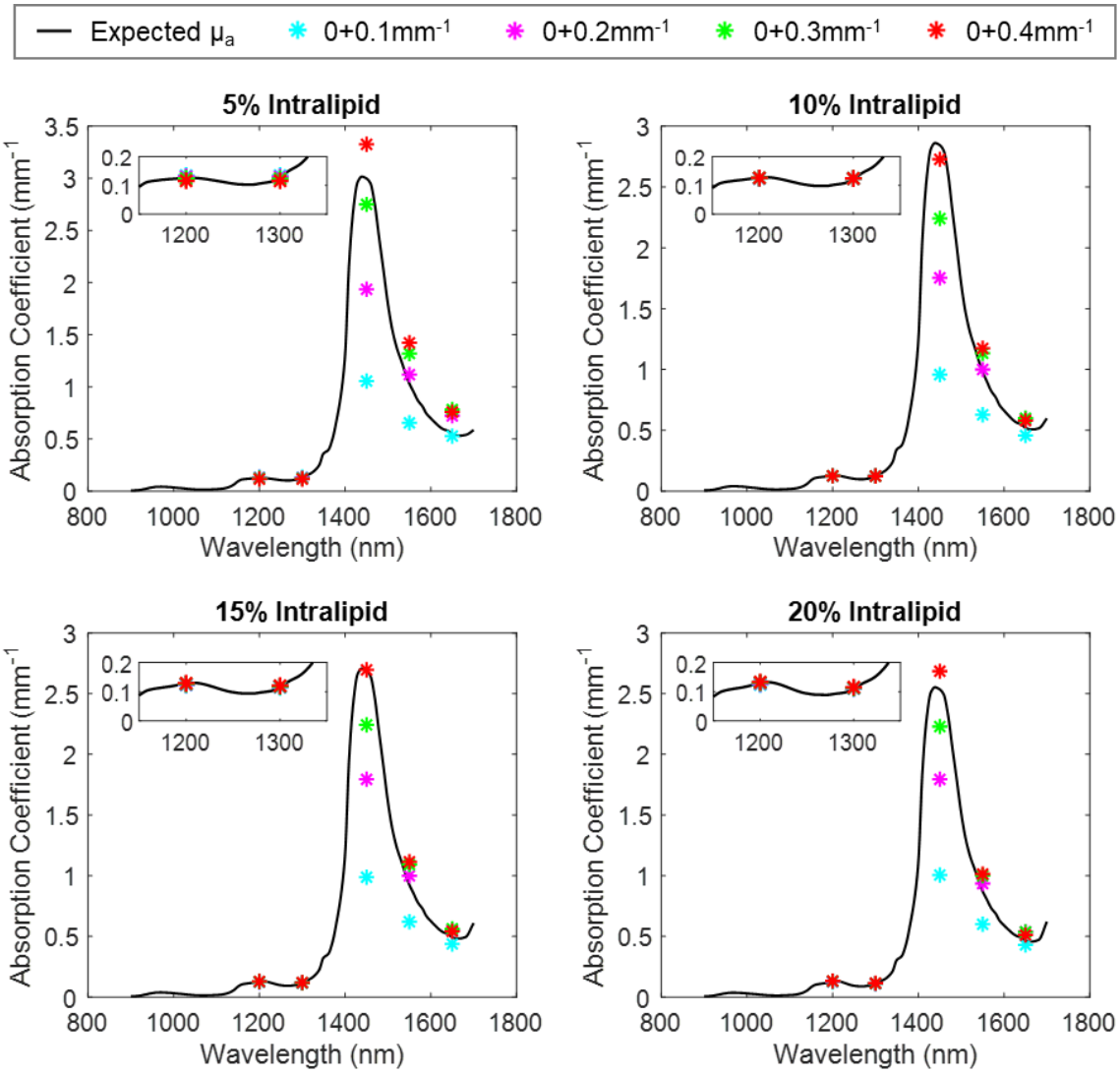

Figure 4.13. Measurement of sample absorption coefficient using different spatial frequency combinations. Absorption coefficients were determined for 5%, 10%, 15%, and 20% Intralipid phantoms. At the 1200 and 1300 nm wavelengths, all spatial frequency combinations yielded accurate measurements of μ_a (insets). At the 1450, 1550, and 1650 nm wavelengths, use of 0 mm^{-1} with a higher spatial frequency resulted in more accurate absorption coefficient measurements.

For the 1200 and 1300 nm wavelengths, the extracted absorption coefficients are all accurate and consistent for all four spatial frequency pairs. For the 1450, 1550, and 1650 nm wavelengths, the higher spatial frequencies provide more accurate estimates of absorption coefficient.

To investigate why pairing the 0 mm^{-1} spatial frequency measurement with a spatial frequency higher than 0.1 mm^{-1} provides more accurate absorption coefficients at longer wavelengths, the corresponding LUTs were generated for diffuse reflectance values (R_d) likely to be encountered in skin at SWIR wavelengths[93]. These R_d values were based on absorption (μ_a) in range of 0.05 to 2.5 mm^{-1}, and reduced scattering (μ_s') in the range of 0.5 – 1.5 mm^{-1}. **Figure 4.14** provides a side-by-side comparison of the 0 + 0.1 mm^{-1} LUT and the 0 + 0.4 mm^{-1} LUT.

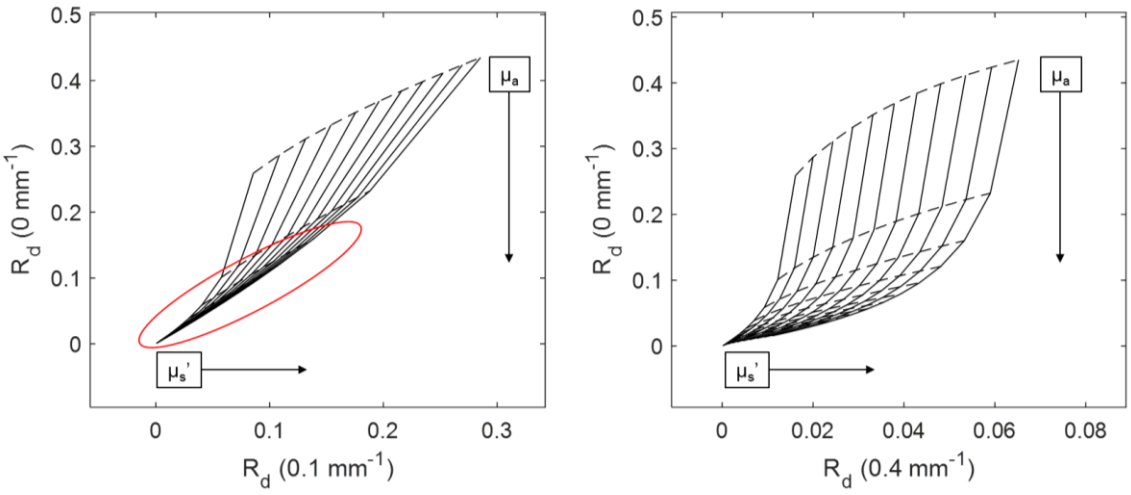

Figure 4.14. Comparison of LUTs with different spatial frequency combinations. Comparison of a 0+0.1mm^{-1} LUT with a 0+0.4mm^{-1} LUT for a physiologically relevant range of optical properties at SWIR wavelengths[93]. μ_a values span the range 0.05 to 2.5 mm^{-1}, and μ_s' values cover the range from 0.5 – 1.5 mm^{-1}.

When absorption becomes high and scattering becomes low (as is expected at wavelengths near the strong water and lipid absorption bands in the SWIR region), the

diffuse reflectance of tissue will become very low, placing measurements into the lower left region of the LUT. The optical property isolines can be seen to collapse on each other in this region (**Figure 4.14**), with the effect being worse for the 0 + 0.1 mm^{-1} LUT. A consequence of this is that when pairs of R_d measurements are made and the LUT is used to identify the corresponding μ_a and μ_s' combination, even small errors in either R_d measurement can lead to large errors in optical property estimates. To see how the selection of spatial frequencies affects the accuracy of extracted chromophore concentrations, data for three selected wavelength pairs are shown in **Figure 4.15**, with the measured water and lipid fractions for each spatial frequency pair plotted against the expected values.

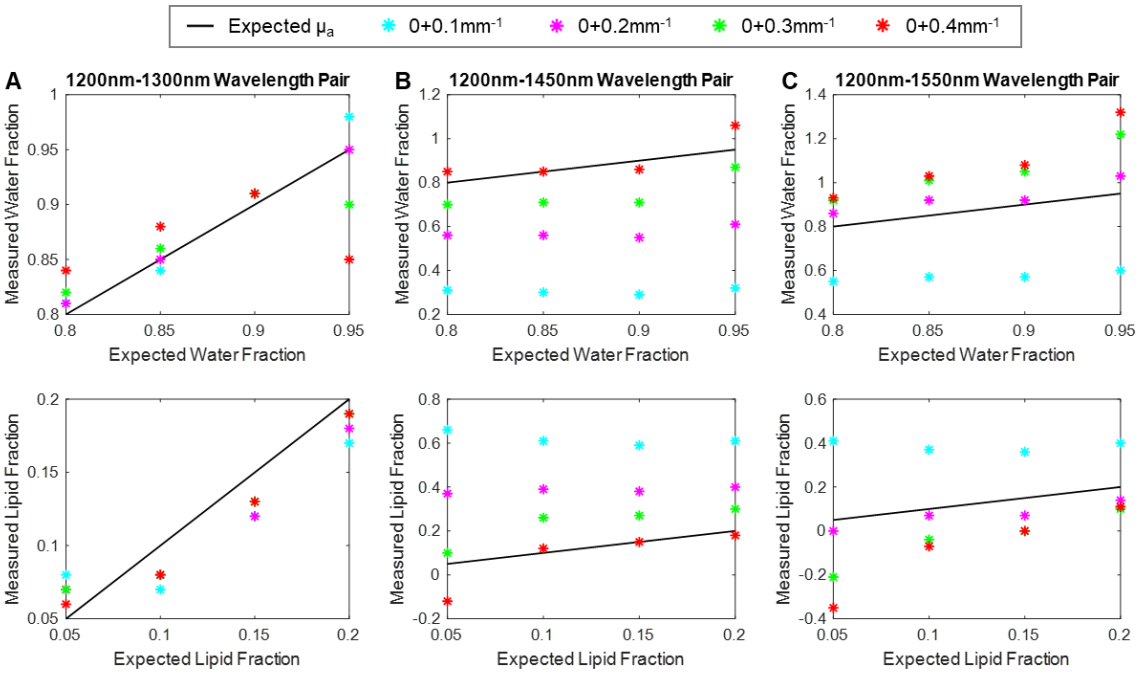

Figure 4.15. Comparison of measured and expected lipid and water fractions for different spatial frequency combinations. Extracted concentration of water and lipid for the 5%, 10%, 15%, and 20% Intralipid titrations for three different wavelength pairs: **(A)** 1200 & 1300 nm, **(B)** 1200 & 1450 nm, and **(C)** 1200 & 1550 nm. For each of these wavelength combinations, a different spatial frequency pair gives the most accurate concentration extractions.

As expected from the underlying absorption coefficient data (**Figure 4.13**), there is generally not a large difference between the measured and expected water / lipid concentrations when different spatial frequencies are used at the 1200 and 1300 nm wavelengths (**Figure 4.15A**). However, when wavelength pairs of 1200/1450 nm or 1200/1550 nm are used (**Figure 4.15B,C**), the use of higher spatial frequencies provides better agreement between measured and expected chromophore fractions. The 0 + 0.4 mm^{-1} spatial frequency pair was the most accurate for 1200/1450 nm illumination (**Figure 4.15B**, red markers), and the 0 + 0.2 mm^{-1} was the most accurate for 1200/1550 nm illumination (**Figure 4.15C**, pink markers).

4.4.2 Discussion

The choice of spatial frequencies used in SFDI can affect the accuracy of sample optical property measurement when pairs of spatial frequencies are used with a look-up table based inversion approach. Inaccurate absorption coefficients will then lead to inaccurate extraction of chromophore concentrations. The look-up table approach works well when pairs of measured R_d values map to distinct values of optical absorption and scattering. Look-up tables generated for certain ranges of optical property values have regions with poorly separated isolines, and this is more apparent with lower AC spatial frequencies. The use of such LUTs to estimate sample optical properties is thus prone to error when the diffuse reflectance values map to these regions, as was the case for the 1450 nm wavelength (**Figure 4.14**). This situation can be improved by generating LUTs for the same optical property ranges but using different spatial frequency pairs. In this study, a single spatial frequency pair did not provide the most accurate absorption coefficient extraction across all tested wavelengths, as demonstrated in **Figure 4.13**. While the extracted absorption coefficients were all accurate and close in value for all four spatial frequency pairs for the 1200 and 1300 nm wavelengths, spatial frequency choice

had a greater impact on absorption coefficient estimates for the 1450, 1550, and 1650 nm wavelengths. Depending on the application, it may be desirable to incorporate additional wavelengths beyond the 1200 and 1300 nm pair. In such a situation, it would be important to acquire raw images using spatial frequency pairs that are not necessarily the same for each wavelength, but instead are chosen to be optimal for each wavelength used. This should lead to measurement of absorption coefficients with minimum error at each wavelength, which in turn will enable extraction of chromophore concentrations with maximum accuracy.

Spatial frequency pairs can also be selected in such a way to sample different depths. Low spatial frequency waves predominantly undergo isotropic scattering and their structure is preserved several millimeters into tissue, while higher spatial frequency wave propagation is influenced by scattering anisotropy and the subsurface fluence pattern is only preserved to sub-millimeter depths[94]. Depending on the application, different depths of tissue can be probed through the specific selection of spatial frequencies, allowing for measurements to come from a certain layer of tissue. For example, if measuring superficial hydration is of interest, higher spatial frequencies can be selected for acquisition and analysis.

4.5 Visual *In Vitro* Example

The benefit of using SFDI over other methods such as point spectroscopy for quantifying chromophore concentration is that it provides a spatially resolved map of the sample, rather than single point measurements. To demonstrate this capability with the SWIR-SFDI system, a phantom was made with two separate regions, one containing vegetable shortening and one containing 20% Intralipid / 80% water. The main ingredient of vegetable shortening is soybean oil, which is also the lipid component of Intralipid. Data was collected at the 1200 nm and 1300 nm wavelengths, with the spatial frequency

combination of 0 and 0.1 mm^{-1}. The chromophore extraction results are shown in **Figure 4.16**.

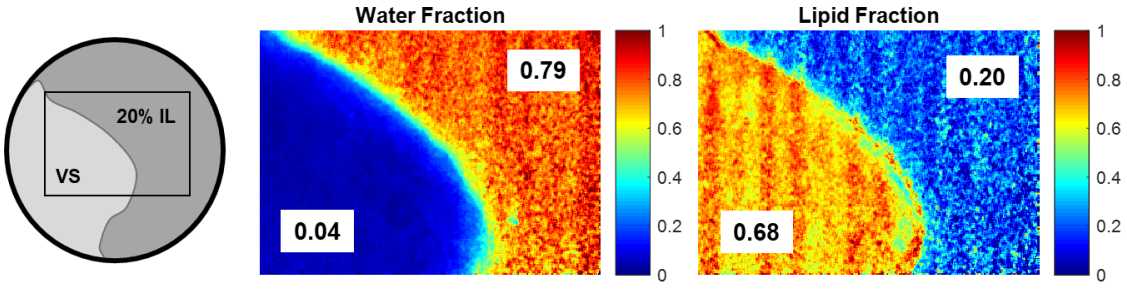

Figure 4.16. Extraction of water and lipid fractions for a vegetable shortening – Intralipid phantom using SWIR-SFDI. Illustration of the vegetable shortening (VS) and 20% Intralipid (IL) phantom, and the water and lipid fraction results corresponding to the rectangular ROI.

The 20% Intralipid region was measured to have a mean water concentration of 80% and a mean lipid concentration of 20%, while the vegetable shortening region (which contains no water in the ingredients list), was measured to have a mean water concentration of 4% and a mean lipid concentration of 68%. These water and lipid fraction images also provide a clear visualization of the different regions, which can be a useful tool for clinical applications.

Point spectroscopy of the vegetable shortening and 20% Intralipid components was performed with the DLP® NIRscan™ Nano Evaluation Module (Texas Instruments, Dallas, TX) to provide an independent measurement to support the SWIR-SFDI measurements. The measured absorbance spectra are provided in **Figure 4.17**. These results confirm that the vegetable shortening has a greater lipid content due to the greater absorbance at the 1210 nm wavelength (lipid absorption peak), and that the 20% Intralipid has a greater water content due to the markedly greater absorbance at the 1450 nm water absorption peak.

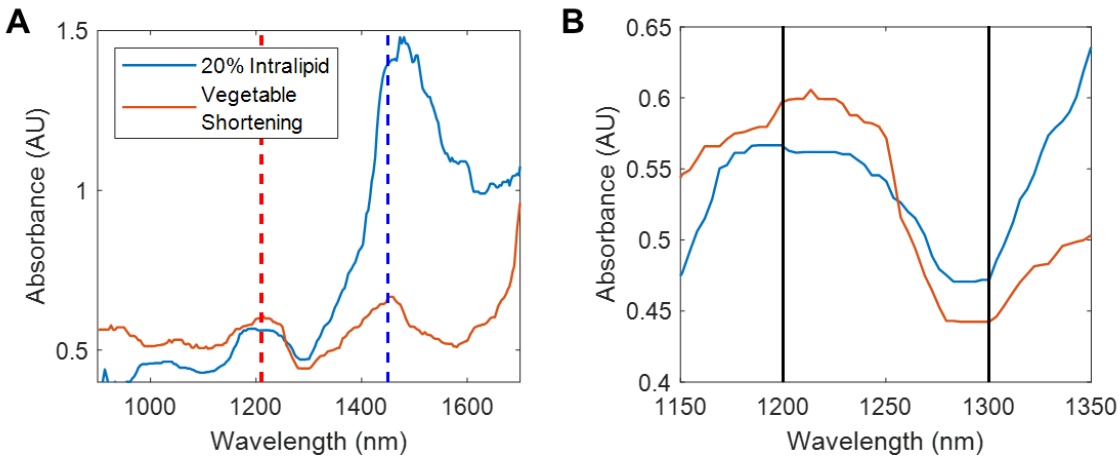

Figure 4.17. Absorbance spectra of vegetable shortening and 20% Intralipid. (A) Absorbance spectra from point spectroscopy results for the entire SWIR range, with the lipid and water peaks highlighted with the red and blue dashed lines, respectively. The lipid absorbance for the vegetable shortening is greater than the 20% Intralipid, supporting the SFDI results. (B) Zoomed in plots, focusing on the SFDI wavelengths of 1200 and 1300 nm, showing greater absorbance of the vegetable shortening at the lipid peak (1200 nm), and greater absorbance of the 20% Intralipid at the water peak (1300 nm).

Figure 4.18 shows the planar illumination results, which help demonstrate why the 1200/1300 nm wavelength pair provides the most accurate extraction of water and lipid content and echoes the spectroscopy results in **Figure 4.17B**. At 1200 nm, the absorption of lipid is greater than that of water, as seen in pure spectra of **Figure 4.18**, and in the planar illumination of the vegetable shortening / Intralipid phantom; the vegetable shortening absorbs the 1200 nm light more, and results in a lower signal compared to the Intralipid portion. At 1300 nm, the absorption of water is greater than lipid absorption and results in lower signal from the Intralipid section compared to the vegetable shortening.

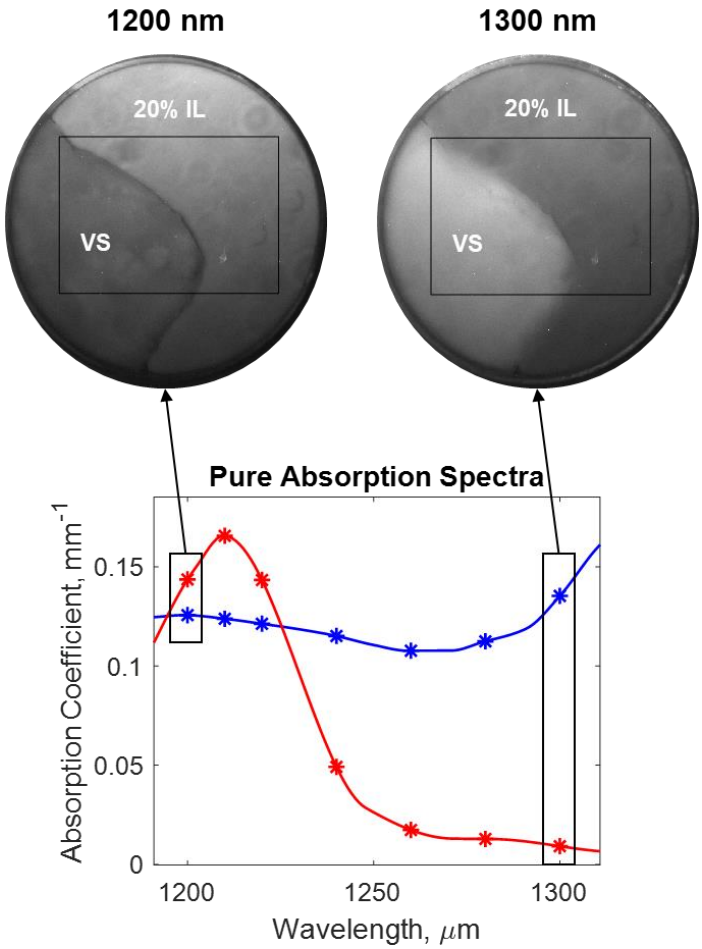

Figure 4.18. Planar illumination of the vegetable shortening – Intralipid phantom. Planar illumination results of the vegetable shortening – Intralipid phantom at 1200 nm and 1300 nm, highlighting the differences in water and lipid absorption between the two wavelengths.

4.6 Conclusions

In this chapter, a SWIR-SFDI system was successfully constructed and multiple factors determining the ability to accurately determine lipid and water content were explored. Condition number and wavelength analysis results demonstrated that wavelengths longer than 1350 nm provided high condition numbers and high extraction errors, which was attributed to the fact that the measurements at these wavelengths are considerably more sensitive to water over lipid due to the significantly greater water

absorption. A low condition number and low extraction error was calculated for the 1200/1300 nm pair, where there are similar contributions from each chromophore at these wavelengths. The experimental results from the Intralipid titrations supported these simulations, demonstrating that accurate chromophore extraction could be achieved with just two wavelengths: 1200 and 1300 nm.

Wavelength selection is just one aspect of the SFDI setup that can influence the accuracy of chromophore concentration extraction; the structure of the LUT is another important factor, which can be adjusted for a range of optical properties by using different spatial frequency pairs. While a wavelength may seem ideal based condition number analysis alone, the resultant diffuse reflectance values might land in a collapsed part of the LUT and would therefore be prone to higher extraction errors. Using higher spatial frequencies in combination with the DC frequency improved the separation of isolines for wavelengths that landed in this problem area and resulted in more accurate optical property estimates for the 1450, 1550, and 1650 nm wavelengths. Since the reflectance after a spatial frequency of 0.3 mm^{-1} is considered sub-diffusive[95], a spatial frequency between 0.1 and 0.3 mm^{-1} in combination with the DC frequency would be the ideal choice to proper extraction of optical properties of water and lipid concentrations.

In addition to optimizing imaging parameters, it will also be important to measure the spatial resolution of the system for future studies, keeping in mind that SFDI is a diffuse imaging technique based on spatial differences in an object's optical properties. This can be accomplished through a contrast-resolution study, as demonstrated by Cuccia *et al.*[92]. For this method, two phantoms of different optical properties are placed adjacent to each other with their edges in direct contact. These phantoms have a large difference in either absorption or scattering, and are measured both directly, and through a homogenous layer with uniform optical properties and thickness (i.e. 2 mm)[92]. The edge-response profile is then determined by measuring the absorption and scattering coefficient values across

these samples, with spatial resolution defined as the distance over which there is a 90% reduction in edge-response contrast[92]. This can be done for both the direct measurement, and for the image acquired through the overlying homogenous layer in order to quantify lateral resolution at different tissue depths[92]. This same type of experiment can be performed with the SWIR-SFDI system presented in this chapter in order to determine the resolution of the system, how it changes with depth, and the differences in resolution between absorption and scattering measurements.

Wavelength optimization analysis was possible due to the tunable supercontinuum laser with a range of 1100 – 2000 nm, but this laser is bulky and expensive and would not be ideal for clinical uptake. LEDs with nominal wavelengths of 1200 nm and 1300 nm are available for just a few hundred dollars each (Thorlabs), and a dichroic mirror could be used to transmit one and reflect the other onto the DMD so that once properly aligned, the illumination arm does not need to be adjusted as it was with the laser. An additional benefit is that the use of incoherent light with the LEDs would eliminate both the speckle and the diffraction issues seen when using a coherent laser source with the DMD. As mentioned in Chapter 1, dry mouth is characterized by decreased saliva secretion, and treatment is focused mainly on symptom management through the use of salivary stimulators and/or oral moisturizers[12]. The efficacy and duration of effects of oral moisturizers on dry mouth patients could potentially be assessed clinically with a simplified SWIR-SFDI system through direct quantification of oral hydration at baseline, directly after treatment, and the subsequent hours to determine the effectiveness of these treatments.

Chapter 5: SWIR reflectance imaging and SFDI for enamel scattering quantification

5.1 Introduction

Multispectral imaging in the NIR/SWIR spectral range can reveal disease-related alterations in soft and hard dental tissues. Narrowband SWIR reflectance imaging has been investigated previously for distinguishing lesions and composites from sound enamel[34-37,96]. These studies found that demineralized enamel and enamel lesions have greater contrast when imaged with SWIR wavelengths beyond 1,300 nm compared to white light illumination[34-37]. The reason for these contrast differences is still under debate, with some attributing higher contrast to increased water absorption of the sound enamel and underlying dentin at the investigated wavelengths. As discussed in Chapter 4, water has high absorption in the SWIR wavelength range beyond 1300 nm (**Figure 5.1A**). Sound enamel and dentin are approximately 10% and 22% water by volume, respectively; the water in these layers can absorb the incident light, and the high water absorption coefficient at SWIR wavelengths likely reduces the intensity of reflected light coming back from the sound tooth[34]. The porous structure of the demineralized enamel can also fill with water and reduce the scattering from the lesion; arrested lesions have vastly reduced water permeability compared to active lesions, so water content of the lesion can be used to distinguish between the two lesion types[34,97,98]. Imaging at wavelengths where water exhibits strong absorption can also be beneficial when assessing dental tissue surrounding restorations due to the low water content of composites[35,96].

To determine the influence of tissue water on contrast results, a study was conducted by Chan *et al.* using select SWIR wavelengths where (i) the absorption coefficient of pure water was similar, and (ii) where the absorption coefficient of pure water was markedly different[34]. The results from this study are shown below in **Figure 5.1B**.

While water absorption is higher at 1470 nm compared to 1860 nm, the 1860 nm results had significantly greater contrast, suggesting that the increased contrast is not necessarily due to increased water absorption of the surrounding sound tissue[34]. Additionally, the absorption coefficient of water is similar at 1470 nm and 1880 nm, but lesion contrast under 1880 nm illumination was significantly greater than with 1470 nm light[34]. The highest contrast achieved was with illumination at the longest wavelength tested of 1950 nm[34]. They therefore attributed the greater contrast at longer wavelengths to be from a decrease in scattering in sound enamel and in the underlying dentin rather than from increased water absorption of the sound tissue[34], as has also been suggested by other studies[35,37].

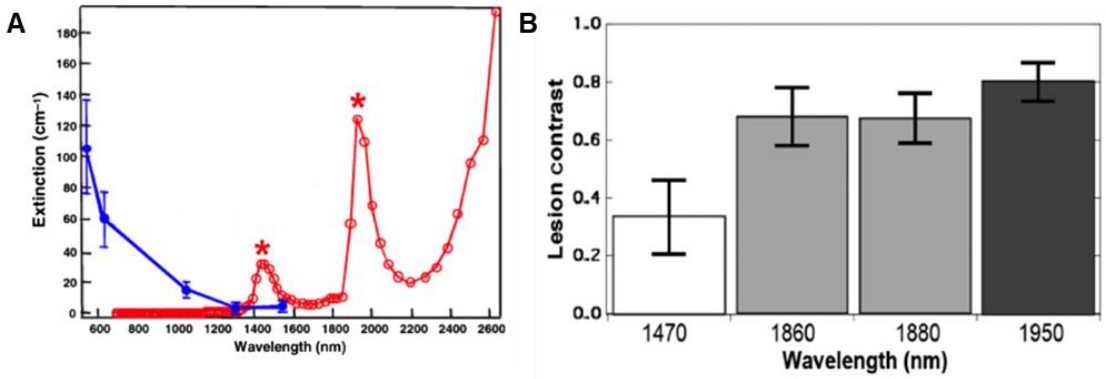

Figure 5.1 Water absorption and reflectance imaging of enamel lesions. (A) Pure water absorption spectrum in red, and the enamel attenuation spectra shown in blue, with notable water absorption peaks starred at 1450 nm and 1950 nm. **(B)** Contrast results from Chan *et al.*[34], showing highest lesion contrast at 1950 nm. (A) and (B) are reproduced Figure 1 and Figure 4, respectively, from Chan *et al.*[34] used under CC BY 4.0.

In the previously mentioned enamel reflectance imaging studies, a singular contrast value calculated as a ratio of the lesion and sound intensities was the metric used for quantification and comparison of illumination at different wavelengths. In order to provide further quantification, Zakian *et al.* used multispectral imaging at various

NIR/SWIR wavelengths to extract parameters based on ratios of the reflectance from the spectral images in order to score the severity of the lesion[37]. This parameter was used to generate a false-color caries map, providing a two-dimensional representation of caries severity[37]. They used reflectance values at 1440 nm and 1610 nm to calculate this parameter since these wavelengths were most affected by water absorption and scattering[37], and these findings for these wavelengths are in agreement with SWIR reflectance imaging results from Fried *et al.*[36]. Zakian *et al.* suggest that the reduced scattering beyond 1450 nm might be due to increased absorption by hydroxyapatite and/or collagen; since lesions have reduced mineral content, there would be greater reflectance at these wavelengths[37].

While such reflectance-based imaging methods allow for inferences to be made about what is contributing to contrast differences, they do not directly quantify the scattering coefficient of the tissue. Due to the design of previous studies and the limitations of current SWIR imaging methods, it is very difficult to decouple the contributions of tissue absorption and scattering to planar reflectance images[34,99]. SFDI is advantageous because it can separate absorption and scattering contributions, and it has been used previously to quantify scattering[100-103]. The work presented in this chapter is the first to use SFDI for imaging of enamel and enamel lesions to directly quantify enamel scattering. By directly quantifying scattering, the actual mechanism behind the observed contrast differences with SWIR reflectance imaging may be determined. Additionally, it is hypothesized that SFDI could provide *en face* views of lesion severity in a manner similar to that of OCT, but over larger fields of view *in vivo* and without having to collect volumetric data. In this chapter, the SWIR SFDI system developed in Chapter 4 was used to determine optimal imaging settings for direct quantification of absorption and reduced scattering in hard dental tissue using the same natural white spot lesion samples from Chapter 3.

5.2 SWIR reflectance imaging of WSLs

In this section, SWIR reflectance imaging of the same natural white spot lesion samples from Chapter 3 (see sections 3.4.1 and 3.4.2 for details) was performed to investigate the limitations of previous studies reported in the literature. Reflectance imaging and SFDI was completed at the same SWIR wavelengths to directly compare the differences in performance and quantification capabilities of the two imaging methods. This chapter provides an initial exploration into whether SFDI can measure the scattering changes in enamel that are known to occur with demineralization. It is well known that drying the tooth provides greater lesion contrast in reflectance measurements[35]. As a result, for simplicity, dehydrated samples with minimal absorption due to water were used in this chapter. In subsequent studies, hydrated samples should be used to introduce absorption effects from water and to better mimic an *in vivo* situation.

5.2.1 Methods

For reflectance imaging, the illumination arm was mounted to directly illuminate the sample as depicted in **Figure 5.2**.

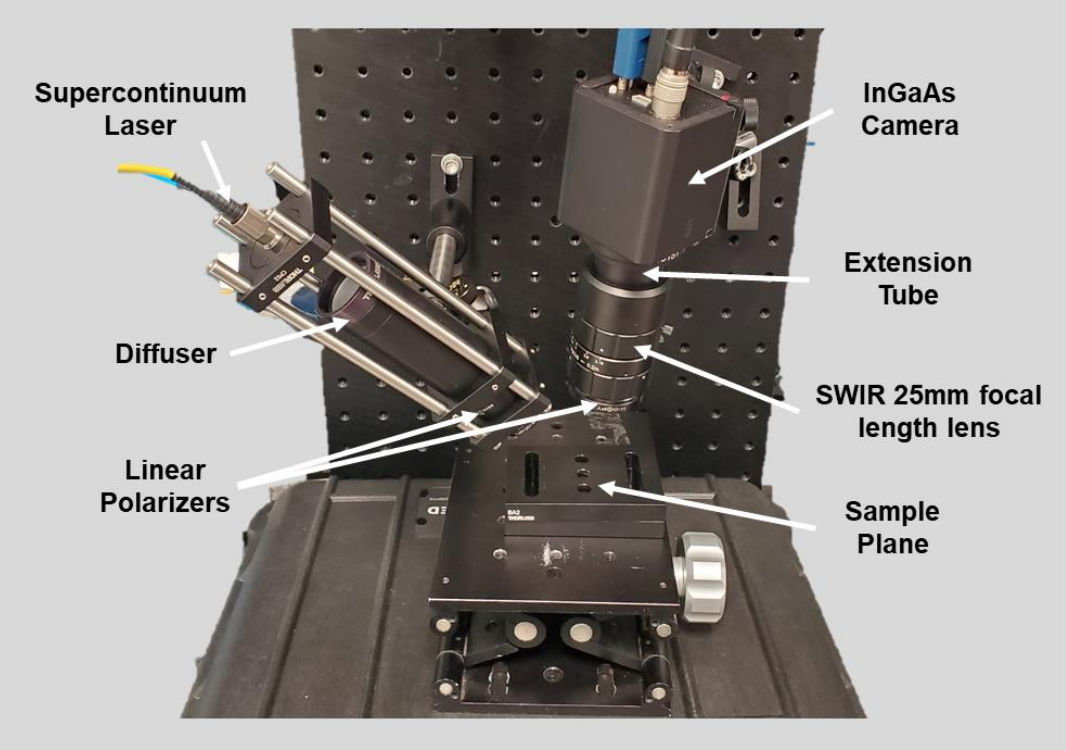

Figure 5.2 SWIR reflectance imaging setup. A supercontinuum laser was collimated and directed onto the sample and reflectance images were captured with an InGaAs camera. To increase the magnification of the camera lens, an extension tube was used, allowing the camera to be moved closer to the sample.

A fiber-coupled SuperK EXTREME supercontinuum white light laser (NKT Photonics, Denmark) was collimated to a diameter of 2.5 cm using a 100 mm focal length lens (Thorlabs, AC254-100-C-ML); a ground glass diffuser was used to increase the illumination uniformity across the sample plane. To increase magnification of the setup for imaging WSL samples, a 10 mm extension tube (Thorlabs, CML10) was added between the InGaAs camera (UTC Aerospace Systems, GA1280JS) and the 25 mm fixed focal length lens (Edmund Optics, 83-160). The camera was then moved closer to the sample plane until proper focus was obtained, resulting in a 5.4 mm diameter field-of-view. A pair of orthogonal linear polarizers (Thorlabs, LPNIR050-MP2) was used in the illumination and imaging paths to reduce specular reflection from the sample surface.

The same white spot lesion samples from Chapter 3 (see sections 3.4.1 and 3.4.2 for details) were imaged with this setup. Reflectance images of each sample were taken at 1200, 1300, 1450, 1550, and 1650 nm. In order to maximize signal at each wavelength, the power of the laser was adjusted to bring the signal at the lesion site to just below saturation. A camera exposure time of 20 ms was used for all images. As described in previous literature[34-36], the contrast for each sample was calculated as:

$$Contrast = \frac{I_{lesion} - I_{sound}}{I_{lesion}} \quad (5.1)$$

For each sample, the measured pixel values within 15 x 15 pixel regions of lesion and sound enamel were averaged and inserted into equation 5.1 to calculate a singular contrast value for each sample, at each wavelength. To generate contrast images, the mean value from the 15 x 15 pixel region of sound enamel was used, and contrast was calculated on a pixel-by-pixel basis as:

$$Contrast = \frac{I_{pixel} - I_{sound}}{I_{pixel}} \quad (5.2)$$

Contrast images were generated and compared for each sample at each wavelength. The same analysis was also performed on grayscale white light images obtained with the stereomicroscope setup described in Chapter 3 (section 3.2.2, figure 3.1) as a baseline for comparison with the contrast derived from narrowband reflectance imaging at the five SWIR wavelengths tested.

5.2.2 Results

The reflectance images for all four WSL samples at all tested wavelengths are shown in **Figure 5.3**, along with grayscale white light images for each sample; the lesion, as identified through visual inspection, is manually outlined in red in the white light images.

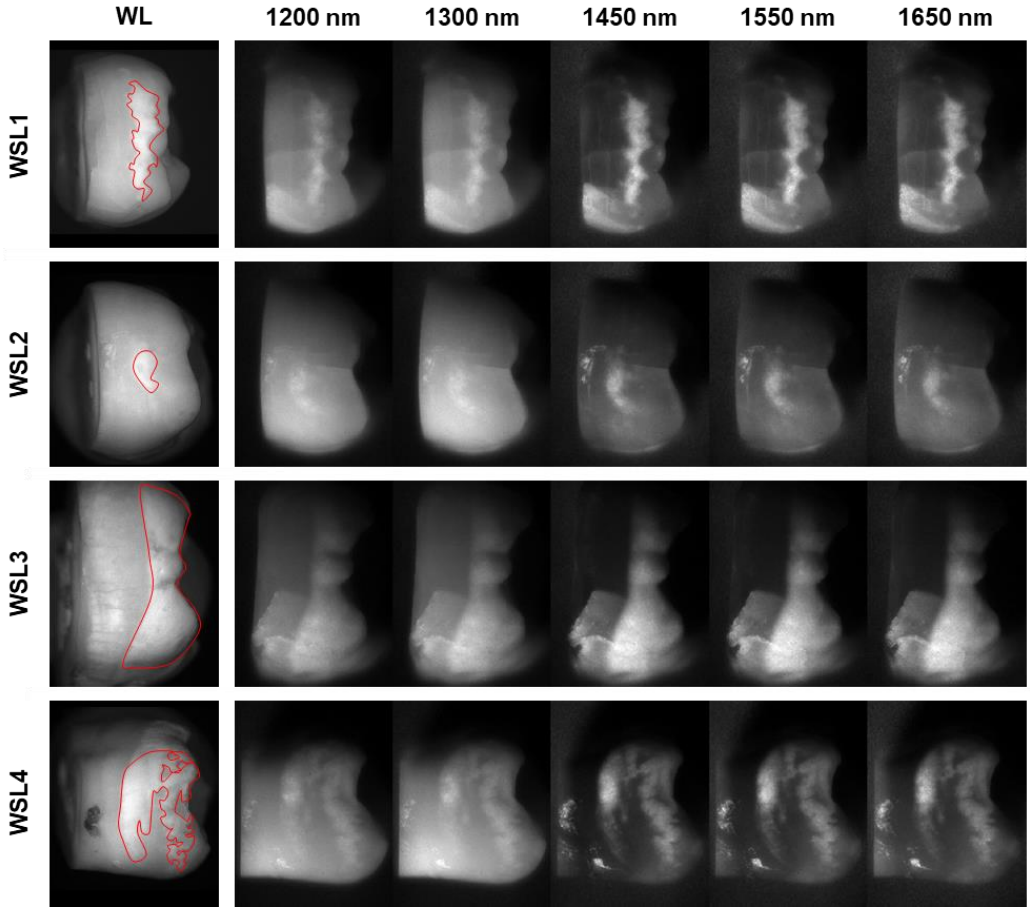

Figure 5.3 SWIR reflectance images of the WSL samples at different wavelengths. Reflectance images of the four WSL samples for white light (WL), 1200, 1300, 1450, 1550, and 1650 nm.

As can be seen in all four samples, the lesion contrast is greater with the 1450, 1550, and 1650 nm results than with the 1200 and 1300 nm wavelengths. Visually, the contrast is similar for the 1200 and 1300 nm images, and for the 1450, 1550, and 1650 nm images. For the 1450, 1550, and 1650 nm results, the signal from the sound tissue has markedly decreased in comparison to the 1200 and 1300 nm results. The differences in contrast are demonstrated quantitatively in the color-mapped contrast images shown in **Figure 5.4**.

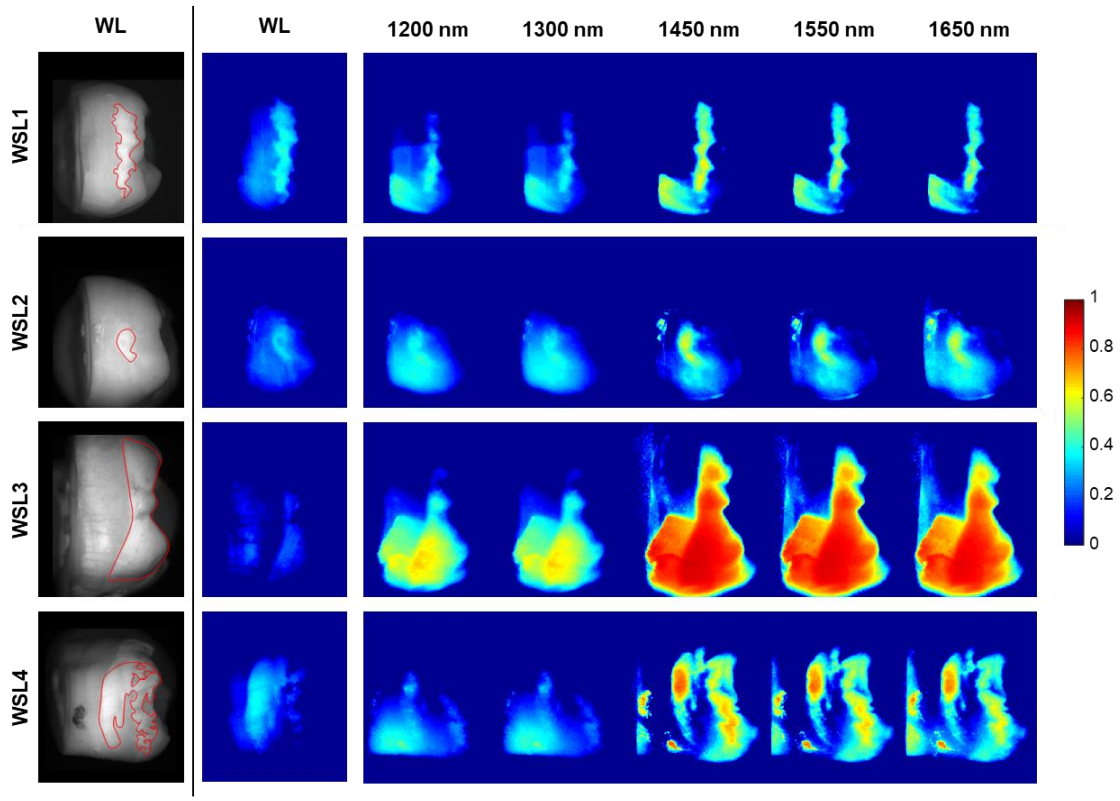

Figure 5.4 Contrast images of the WSL samples at different wavelengths. White light images, followed by contrast images of four WSL samples for white light (WL), 1200, 1300, 1450, 1550, and 1650 nm. All contrast images are displayed on the same color range (0 – 1).

The contrast between white spot lesions and sound enamel is greater with the 1450, 1550, and 1650 nm illumination compared to the 1200 and 1300 nm wavelengths, and the differences in contrast within the 1200 and 1300 nm results and within the 1450, 1550, and 1650 nm results are minimal. Quantitatively, the results are displayed as bar graphs in **Figure 5.5**. **Figure 5.5A** shows the contrast as a function of sample, with each colored bar representing the contrast for each investigated illumination wavelength. **Figure 5.5B** plots contrast against wavelength, with each bar representing the mean contrast value for all four samples, and the error bars signifying the standard deviation.

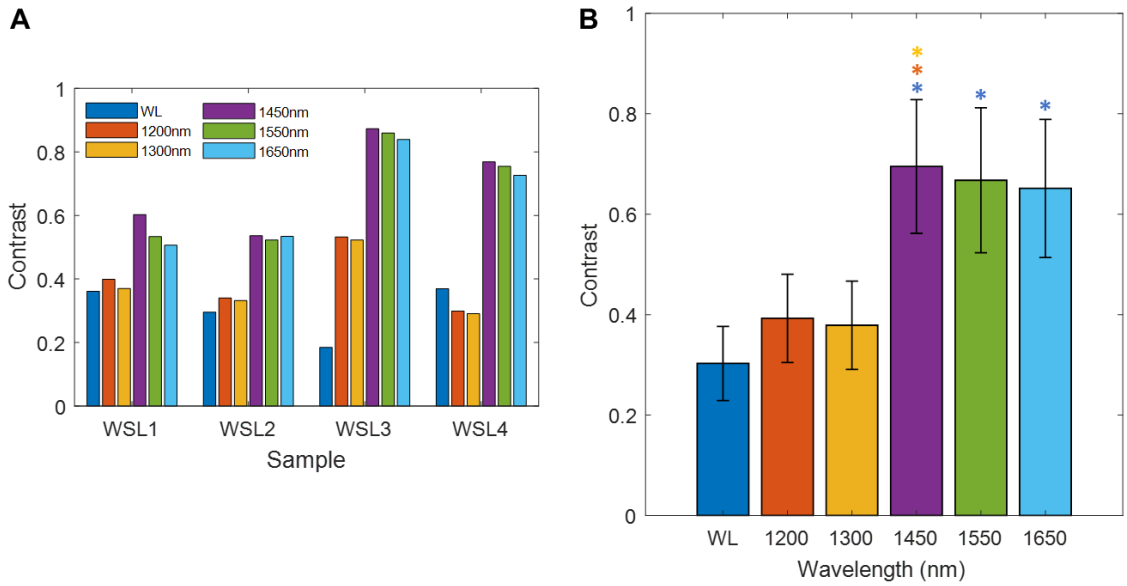

Figure 5.5 Quantitative results for the contrast reflectance imaging of WSLs. (A) Contrast values for each sample, and the results for each wavelength shown as different bar colors. **(B)** The mean contrast value for all samples (n = 4) at each wavelength. * p<0.05, color-coordinated to corresponding bars.

Due to the small sample size (n = 4), the nonparametric Mann-Whitney U-test was performed between each wavelength pair. From these results, there was a statistically significant ($p<0.05$) difference in contrast between the white light results and the 1450, 1550, and 1650 nm contrast results. Additionally, there was a statistically significant increase in contrast between the 1200 and 1450 nm results, and between the 1300 and 1450 nm results.

5.2.3 Discussion

Greater lesion contrast was achieved at 1450, 1550, and 1650 nm compared to the 1200 and 1300 nm results, and the contrast was similar at these three wavelengths. These results, and the decrease in signal from sound enamel at these wavelengths (**Figure 5.3**) are in agreement with the conclusions made by Chan *et al.*[34] that the

differences in lesion contrast are not due to water absorption but rather differences in sound and lesion enamel scattering at the test SWIR wavelengths; by using dehydrated samples, the influence of water absorption was eliminated from the results. While this work and previous studies have demonstrated that lesion contrast increases with illumination at longer wavelengths, the true reason behind the contrast differences can only be inferred due to the inability to decouple absorption and scattering effects with reflectance imaging methods. Direct quantification of enamel scattering is necessary to better understand what is causing the differences lesion contrast and better understand the changes that are happening to the tissue with demineralization, and such quantification can potentially be achieved with SFDI.

5.3 SWIR SFDI for quantifying enamel and WSL scattering

To determine the absorption and reduced scattering coefficients and the contributions of each to the differences in lesion contrast with wavelength, SFDI was performed at the same SWIR wavelengths investigated in Section 5.2 for the same set of white spot lesion samples.

5.3.1 Methods

The same SFDI setup depicted and described in Section 4.2.3 was used for imaging of the white spot lesion samples, with one modification; a longer focal length camera lens was used in order to achieve higher magnification without having to change the optics and alignment of the system. A 50 mm fixed focal length lens (Thorlabs MVL50M23) was to achieve this. All four samples were placed within the field-of-view, and data was collected at 1200, 1300, 1450, 1550, and 1650 nm. SFDI analysis was performed for four different spatial frequency combinations: DC (0 mm^{-1}) combined with 0.1 mm^{-1}, 0.2 mm^{-1}, 0.3 mm^{-1}, and 0.4 mm^{-1}. Absorption and reduced scattering coefficient maps were generated for each wavelength through calibration with a 10% intralipid phantom at each of the spatial frequency combinations.

5.3.2 Results

The absorption and reduced scattering coefficient maps at 1200, 1300, 1450, 1550, and 1650 nm for the four WSL samples are shown in **Figure 5.6** for the 0 and 0.3 mm^{-1} spatial frequency combination. These results exhibited the least noise at the longer wavelengths and were therefore chosen for display purposes. At all wavelengths, the lesions are clearly distinguishable in the reduced scattering coefficient (μ_s') maps, with the lesions having higher scattering coefficients compared to the surrounding sound enamel.

Scattering from within the lesion increases at longer wavelengths, while scattering in the surrounding sound tissue appears similar across all wavelengths.

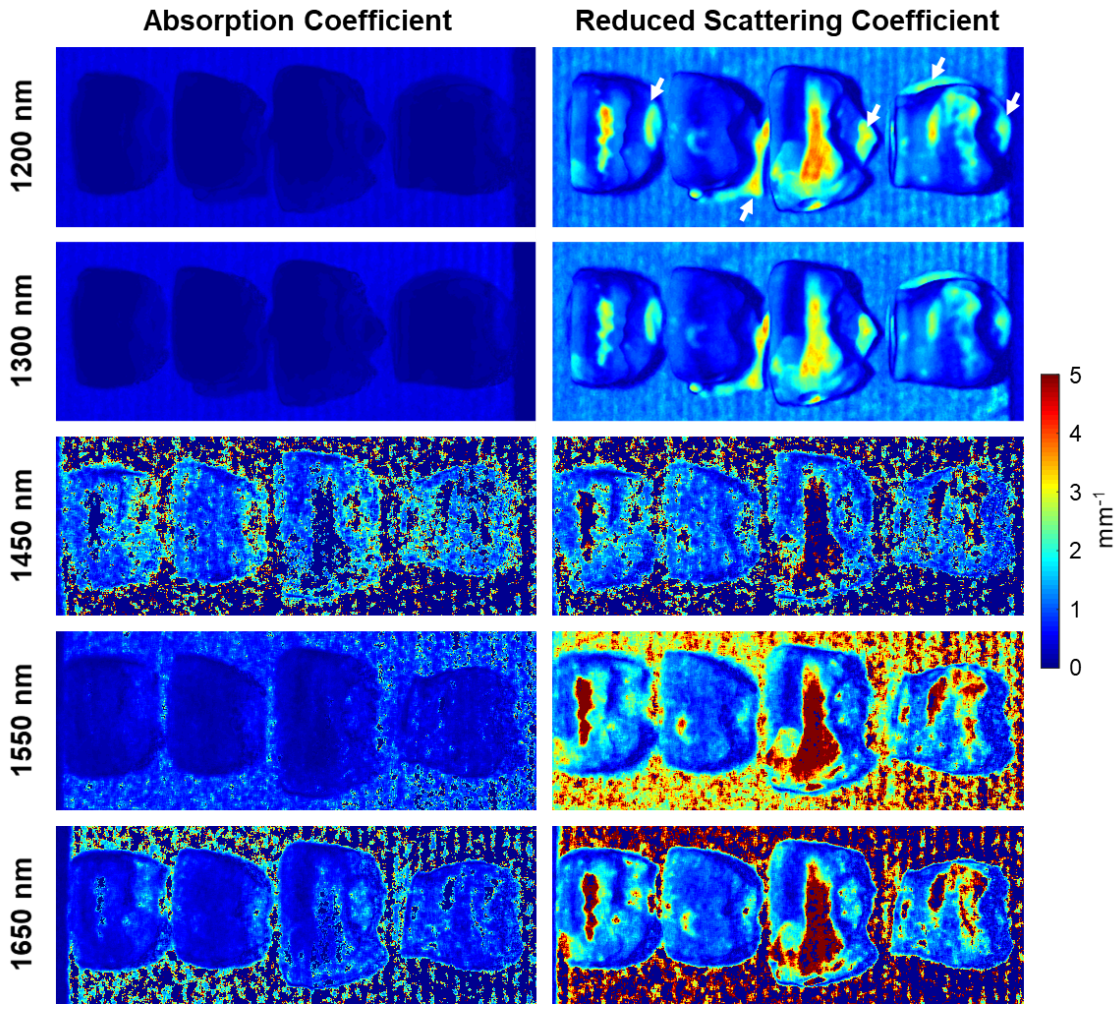

Figure 5.6 Absorption and reduced scattering coefficient maps of the WSL samples at different wavelengths. Absorption and reduced scattering coefficient maps of four WSL samples at 1200, 1300, 1450, 1550, and 1650 nm, calculated for the spatial frequency combination of 0 and 0.3 mm^{-1}. All images are displayed on the same color scale (μ_s' = 0 – 5 mm^{-1}). White arrows indicate signal from tack used for mounting samples, not enamel.

Absorption is very low for these samples at the investigated wavelengths, and there is minimal absorption contrast observed between the lesion and sound enamel. As a result, the focus of the analysis will remain on the scattering coefficient maps. These

are compared for the four different spatial frequency combinations at each wavelength in **Figure 5.7**. Generally, the μ_s' value measured within lesions increases with higher spatial frequencies, while the μ_s' measured in sound enamel decreases.

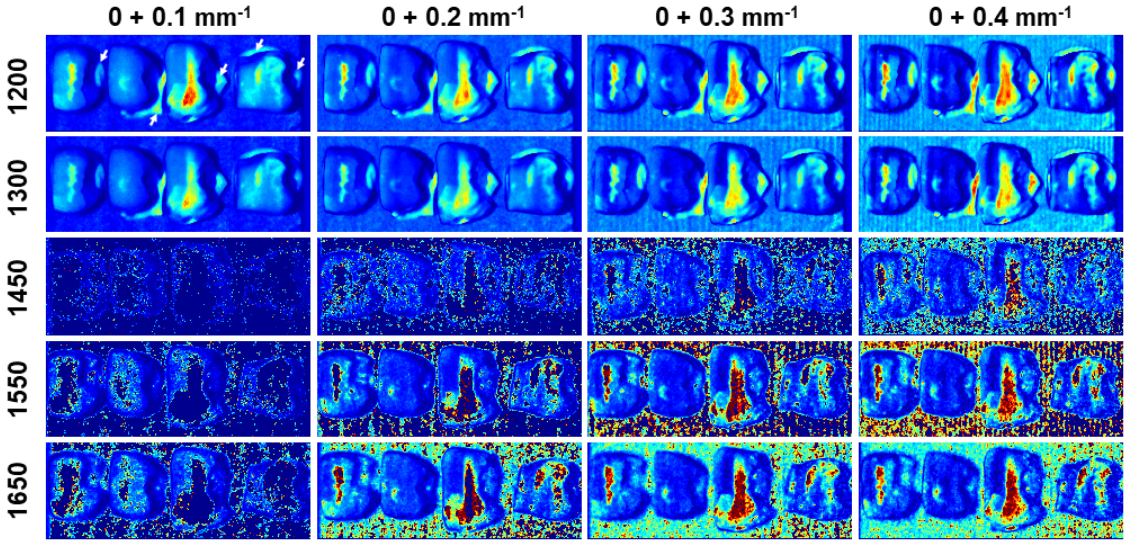

Figure 5.7 Reduced scattering coefficient maps for the WSL samples measured at different wavelengths and with different spatial frequency combinations. Reduced scattering coefficient maps of four WSL samples at 1200, 1300, 1450, 1550, and 1650 nm for the different spatial frequency combinations: 0 + 0.1 mm^{-1}, 0 + 0.2 mm^{-1}, 0 + 0.3 mm^{-1}, and 0 + 0.4 mm^{-1} All images are displayed on the same color range: 0 (blue) – 5 mm^{-1} (red). White arrows indicate signal from tack used for mounting samples, not enamel.

The μ_s' maps at the 1450, 1550, and 1650 nm wavelengths have regions of missing data, which appear as dark blue regions corresponding to NaN (not-a-number) values. To determine the source of these NaN values in the μ_s' maps, the underlying diffuse reflectance (R_d) images were investigated, as shown in **Figure 5.8**. For simplification, just the 0 and 0.1 mm^{-1} frequency results are shown, but similar results were observed with the other spatial frequency combinations. For the 1450, 1550, and 1650 nm results, some R_d values at the 0.1 mm^{-1} frequency were calculated as being greater than for the corresponding pixel at the DC (0 mm^{-1}) frequency. This is unexpected since

the diffuse reflectance of spatially modulated light should always be less than that under planar illumination. Consequently, a combination of R_d values where R_d (0.1 mm^{-1}) > R_d (0 mm^{-1}) falls outside of the region where μ_a and μ_s' values are provided in the look-up-table, producing NaNs at the corresponding pixels in the absorption and reduced scattering coefficient maps.

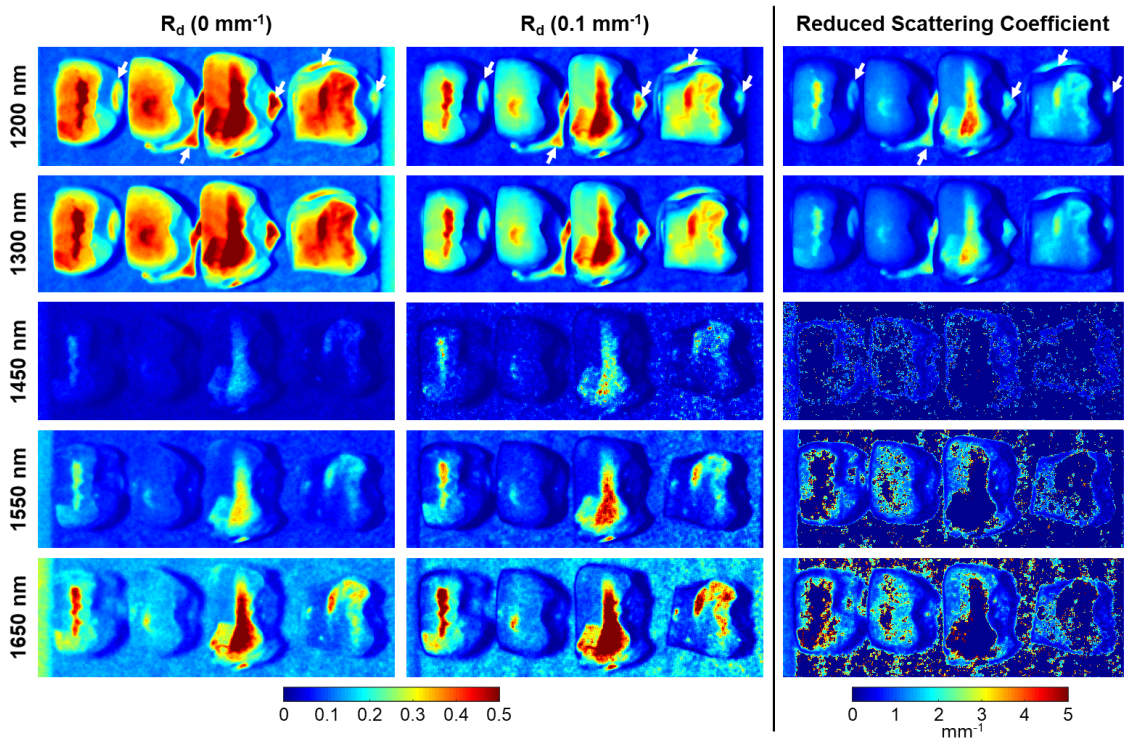

Figure 5.8 Diffuse reflectance images at illumination spatial frequencies of 0 and 0.1 mm^{-1}, with resultant reduced scattering coefficient maps of the WSL samples at 1200, 1300, 1450, 1550, and 1650 nm wavelengths. Missing data in the reduced scattering maps are due to R_d at 0.1 mm^{-1} measuring greater than the R_d at 0 mm^{-1} as a result of imperfect demodulation. White arrows indicate signal from tack used for mounting samples, not enamel.

To provide a quantitative analysis, the mean scattering coefficient values as a function of spatial frequency combination and of wavelength are provided in **Figure 5.9A** and **5.9B**, respectively. For these plots, the mean μ_s' values for sound and lesion were averaged for the four samples, and the error bars represent the standard deviation.

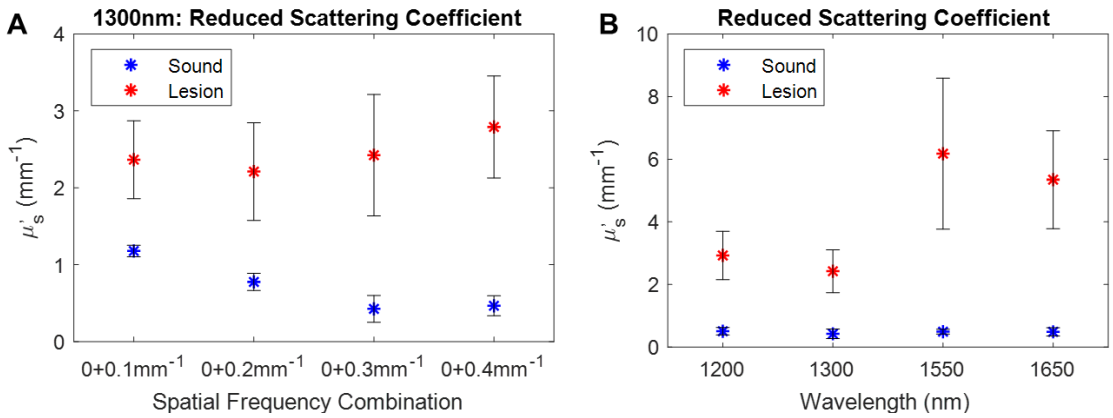

Figure 5.9 Mean reduced scattering coefficient values as a function of spatial frequency combination and of wavelength. (A) Reduced scattering coefficient as a function of spatial frequency combination for the 1300 nm data. There is an increase in lesion scattering and a decrease in sound enamel scattering with increasing AC spatial frequency. **(B)** Reduced scattering coefficient as a function of wavelength for the 0 + 0.3 mm^{-1} results. There is a slight decrease to plateau of reduced scattering in sound enamel with increasing wavelength. There is greater scattering of the lesion with the longer wavelengths (1550 and 1650 nm) compared to the 1200 and 1300 nm results. For both plots, the asterisks represent the mean value, and the error bars are the standard deviation.

For the spatial frequency combination comparison (**Figure 5.9A**), the results from the 1300 nm analysis were used since this data was clean and this wavelength is typically investigated for OCT of enamel. There is an increase in lesion scattering and a decrease in sound enamel scattering with increasing AC spatial frequency. For the wavelength comparison, (**Figure 5.9B**), the mean scattering coefficient was calculated from the 0 and 0.3 mm^{-1} frequency combination since these maps had the least noise (**Figure 5.7**). For the sound enamel, there is a slight decrease to plateau of μ_s' with increasing wavelength. For the lesion, there is less of a consistent trend. Scattering in the lesion decreases slightly from 1200 to 1300 nm, and then there is an increase in μ_s' for 1550 nm followed by a slight decrease again at 1650 nm. Statistical analysis via Mann-Whitney U-tests showed no significant difference in μ_s' between the wavelengths.

5.3.3 Discussion

In this study, the WSL samples exhibited very low absorption, and the contrast of the lesion was minimal in the absorption coefficient maps. This was expected, as the samples were fully dehydrated and there was no contribution from water. However, other studies in literature[34-36,96], used samples that were kept hydrated as would be the case for an *in vivo* situation, and if this SWIR-SFDI setup was to be used clinically, these results would likely change. Water fills in the gaps of the porous active lesions, which significantly reduces the scattering from the lesion. This is different from arrested lesions, which have markedly reduced water permeability; this difference has been used to differentiate between the two types of lesions[34,97,98]. To increase lesion contrast and detection during clinical examination, air is blown over the lesion for a few seconds by the clinician[34,35]. A similar exercise could be performed prior to SFDI imaging to better isolate the lesion scattering.

The scattering differences highlighted in **Figure 5.9** demonstrate higher lesion scattering with higher spatial frequencies and with longer wavelengths. As mentioned in Chapter 4, the choice of spatial frequencies largely impacts the accuracy of optical property separation[86]. Lower spatial frequencies are sensitive to both absorption and scattering, whereas higher spatial frequencies are primarily sensitive to scattering and probe shallower tissue depths[86,92]. If very low and very high spatial frequencies are used together to extract absorption and scattering, the “partial volume” effect may result in errors of this extraction when the tissue is not fully homogenous[86], as is the case for the white spot lesion samples. Since the different spatial frequencies are sampling different thicknesses of tissue, spatial frequency combinations that are very different, such as the 0 mm^{-1} and 0.4 mm^{-1} combination, will have respective R_d images that are based off different tissue volumes. So when the optical properties are different in a superficial layer, which is almost exclusively sampled by the 0.4 mm^{-1} frequency, compared to the rest of

the sample, which is in part sampled by the 0 mm^{-1} frequency, then there could be errors in determining the optical properties from this combination of R_d measurements. Depth penetration and partial volume effects could also be contributing to the differences in scattering seen with the various wavelength choices, since different wavelengths sample different tissue depths depending on the absorption and scattering of the sample at each wavelength choice. Attempts should be made to reduced differences in depth sampling by selecting a pair of spatial frequencies that accurately extract optical properties while minimizing the difference in spatial frequency[86].

As demonstrated in **Figure 5.7**, the 1450, 1550, and 1650 nm absorption and reduced scattering coefficient maps have gaps of missing data where the R_d values at the AC frequencies are measuring greater than the R_d values at the DC frequency, specifically in the location of the lesion, leading to a pair of diffuse reflectance values that does not have a corresponding absorption and reduced scattering coefficient pair within the look-up table. These gaps in data are likely due to do the calibration issues discussed in chapter 4 (section 4.2.5), further motivating the need for a better calibration phantom for the longer wavelengths, where the diffuse reflectance will provide calibration images that have adequate signal above background, are less susceptible to noise, and provide more accurate estimates of optical properties.

5.4 Conclusions

This study was the first to use SFDI to directly quantify enamel and white spot lesion absorption and reduced scattering. From the results of this chapter, the reduced scattering in the sound enamel does not markedly decrease with wavelength in the 1200 to 1650 nm range, but rather plateaus. This contradicts the conclusions made by Chan *et al.* that enamel scattering continues to decrease after 1300 nm, and this decrease in light scattering from sound enamel is most responsible for higher lesion contrast at longer NIR

wavelengths[34]. While it is interesting and important to see how scattering changes with wavelength to help understand contrast differences between lesion and sound enamel with increasing wavelength, the reduced scattering coefficient maps from the 1300 nm data alone provide clear distinction between lesion and sound enamel and could be used clinically to quickly and easily establish the presence of such a lesion. The reduced scattering values also point to differences in lesion severity and depth in a similar manner to that observed with OCT in Chapter 3, as highlighted in the side-by-side comparison in **Figure 5.10**.

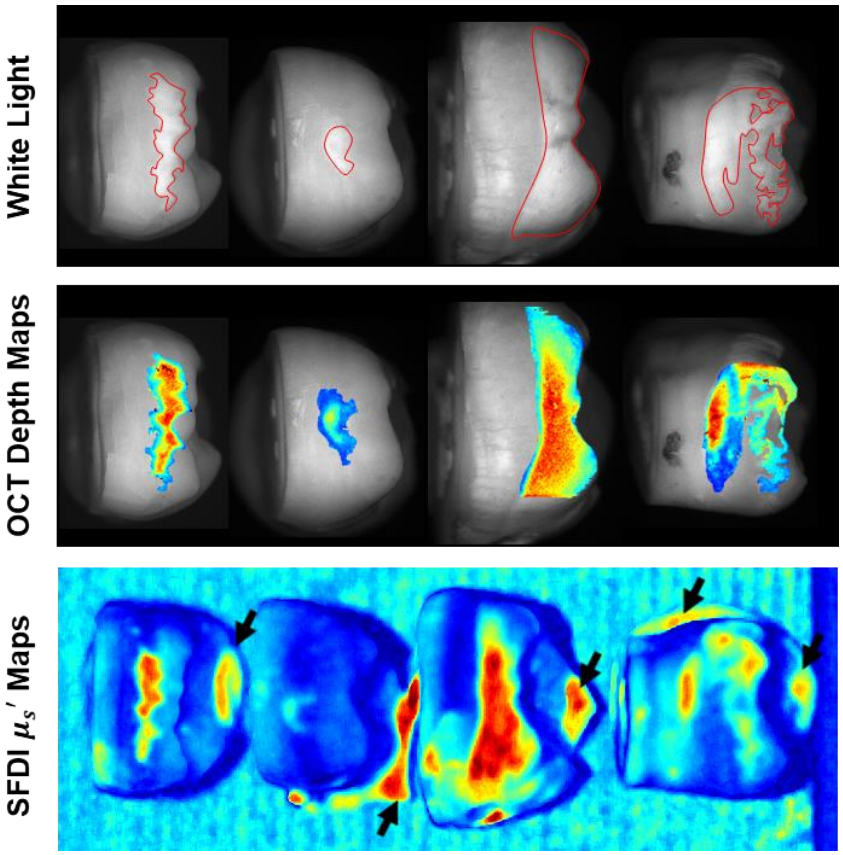

Figure 5.10 Comparison of OCT depth map with SWIR-SFDI reduced scattering coefficient map for the WSL samples. Comparison of the OCT depth maps with reduced scattering coefficient maps generated with SFDI at 1300 nm. White light images with manual segmentation of the lesion provided in red. SFDI provides clear distinction of lesion from sound enamel without manual segmentation and distinguishes lesion severity based on differences in scattering. Black arrows indicate signal from tack used for mounting samples, not enamel.

In relation to clinical uptake, SWIR-SFDI is advantageous over OCT in both speed of acquisition and field-of-view (FOV). With an exposure time of 150 ms for each spatial frequency, SFDI data acquisition takes just a few seconds, and is therefore far less susceptible to subject motion compared to volumetric OCT scans. SFDI can provide a much larger FOV compared with the maximum FOV of 10 mm^2 that the OCT system used here provides, making it more suitable for clinical screening of lesions. Additionally, segmentation of the lesion from the surrounding sound enamel could be achieved with SFDI simply through a cutoff value of reduced scattering, making it quick and free from user-input and associated errors. OCT on the other hand required manual segmentation of the lesion in MATLAB before generating the depth map.

This study was a pilot study on a few relevant samples. Future work would include performing the analysis on a larger cohort of samples and optimizing the imaging setup to ensure that demodulation is ideal for all SWIR wavelengths. Moreover, this work stops at the extraction of absorption and reduced scattering coefficients, but SFDI has the ability to go one step further and extract concentrations. NIR spectroscopy of enamel and enamel components (hydroxyapatite) has been investigated, and absorption spectra for these components are provided in the literature[104]. Enamel is comprised largely of hydroxyapatite, which has absorption peaks near 10000 cm^{-1} (1000 nm) and 7000 cm^{-1} (1428 nm)[104]. Such spectra could be used with SWIR-SFDI to allow for extraction of mineral content differences in white spot lesions. This concept will be investigated in the future direction of this work.

Chapter 6: Conclusions

6.1 Dissertation summary

The overarching goal of this dissertation was to develop short-wave infrared imaging techniques for the assessment and quantification of dental tissue conditions. Various commercially available OCT systems can be used for enamel studies, as demonstrated in Chapter 2. It is important to characterize the systems as was done in this work in order to understand the advantages and limitations (i.e. imaging depth, cost) of each system when planning a study, especially when certain dental conditions may require a particular set of imaging parameters. While the Tel320 provided superior imaging depth and axial resolution, the OQ LabScope 1.0 delivered detailed visualization of the first 500 microns of dental tissue for a fraction of the cost and allows quick and simple adjustment of focus, which can be beneficial for imaging *in vivo* and *in vitro* superficial conditions. For birefringent substrates like enamel, PS-OCT was advantageous over conventional OCT because it reduced banding artifacts. This work can help guide clinicians and researchers in determining which commercially available OCT configurations would be best for their dental applications.

Chapter 3 demonstrated the ability of the Tel320 OCT system to quantify white spot lesion formation, heterogeneity, and treatment, using both artificial and natural WSL samples. OCT can directly visualize the subsurface dental tissue and allow for true quantification and assessment of the depth of effect, as demonstrated in this work. The methodology developed in Chapter 3 could be used for *in vitro / ex vivo* studies for product development and efficacy research as well as for clinical point-of-care assessment of lesion severity and treatment. With the current gold standards for detection being visual inspection and X-ray, OCT would be an advantageous technology to implement to directly visualize subsurface conditions in a nonionizing and noncontact manner. The work

provided in Chapters 2 and 3 may support future efforts toward clinical uptake of OCT for diagnosis and treatment monitoring of potentially reversible dental indications such as demineralization.

Chapter 4 detailed the creation of a SWIR-SFDI system for the quantification of water and lipid content. This was the first study on optimizing wavelength selection to determine a pair of illumination wavelengths that allowed for accurate quantification of these chromophores. The experimental results from the Intralipid titrations supported the condition number analysis, demonstrating that accurate chromophore extraction could be achieved with just two wavelengths: 1200 and 1300 nm. The optimization of spatial frequency selection was also completed, demonstrating that a single spatial frequency pair did not provide the most accurate absorption coefficient extraction across all tested wavelengths. While the extracted absorption coefficients were all accurate and close in value for all four spatial frequency pairs for the 1200 and 1300 nm wavelengths, spatial frequency choice had a greater impact on absorption coefficient estimates for the 1450, 1550, and 1650 nm wavelengths. Depending on the application, it may be desirable to incorporate additional wavelengths beyond the 1200 and 1300 nm pair, and for such a situation, it would be important to acquire raw images using spatial frequency pairs that are not necessarily the same for each wavelength, but instead are chosen to be optimal for each wavelength used. As mentioned in Chapter 1, dry mouth is characterized by decreased saliva secretion, and treatment is focused mainly on symptom management through the use of salivary stimulators and/or oral moisturizers[12]. The efficacy and duration of effects of oral moisturizers on dry mouth patients could potentially be assessed clinically with a simplified SWIR-SFDI system through direct quantification of oral hydration.

Chapter 5 utilized this SWIR-SFDI system to provide spatially resolved maps of optical scattering coefficient for the natural white spot lesion samples studied with OCT in

Chapter 3. This study demonstrated the capability of the SWIR-SFDI system to provide quantitative assessment of hard dental tissue in addition to hydration evaluation. A potential advantage of SWIR-SFDI compared to OCT and planar reflectance imaging was its ability to separate lesions from surrounding sound enamel. With OCT, the lesion had to be manually segmented in MATLAB before generating the depth map; contrast images generated from SWIR planar reflectance imaging resulted in sound areas registering as regions with high contrast in addition to the lesion. On the other hand, the scattering coefficient values measured by SWIR-SFDI could distinguish sound tissue from lesions simply through the use of a cutoff value (i.e. 1 mm^{-1}), which would make these results more accurate and quicker to obtain. These reduced scattering coefficient maps provide complementary information to that obtained by OCT, since both directly capture scattering effects, and but SFDI can provide a 2D *en face* map of lesion severity over a larger field-of-view in a fraction of the time.

6.2 Future directions

6.2.1 OCT and QLF handheld probe for assessment of WSLs

As was seen in Chapter 3, QLF can provide clear distinction of white spot lesions, sometimes picking up areas not distinguishable with white light imaging, as seen with Sample 2 in **Figure 3.13**; however, information on lesion depth is not readily available. OCT, on the other hand, provides direct visualization of the subsurface tissue and can be used to quantify lesion severity and treatment. Combining these two modalities would allow for quick and precise identification of lesions through QLF, and corresponding OCT measurements for depth quantification. The long-term goal of this research is to establish non-invasive tools for the assessment and diagnosis of early dental diseases, including enamel demineralization and white spot lesions. While the current commercially available OCT systems were adequate for imaging the gingiva in the front of the mouth, a handheld

probe will be needed for gaining access to the inner gums and molars. By combining OCT with QLF in a compact, handheld probe, multi-functional complementary data may be obtained for identifying and assessing demineralization and subsurface lesions.

A handheld probe prototype was developed in the lab to allow for simultaneous QLF and OCT imaging. A schematic and photograph of the handheld probe is provided below in **Figure 6.1**. The spectral domain OCT (SD-OCT) component uses a 100-nm bandwidth (FWHM) superluminescent diode source centered at 1325 nm (Thorlabs, Newton, New Jersey). Light from the source is split into sample and reference arms by a fiber-optic beamsplitter (Newport, Irvine, California), so that 90% of the light travels to the sample arm, as described in detail below, illuminating the sample with 1.8 mW. The remaining 10% of the light is directed to a stationary reference arm. Recombined light is directed to a custom-built spectrometer where it is dispersed by a 1200 lines/mm transmission diffraction grating (Wasatch, Logan, Utah) and focused onto a 1024 element InGaAs line scan camera (SUI Goodrich, Princeton, New Jersey). The parameters of the OCT light source and the spectrometer provide a theoretical axial resolution and an imaging depth of 8.0 μm and 3.0 mm, respectively. This system acquires data at a rate of 25,500 A-lines/s, which corresponds to 25.3 fps.

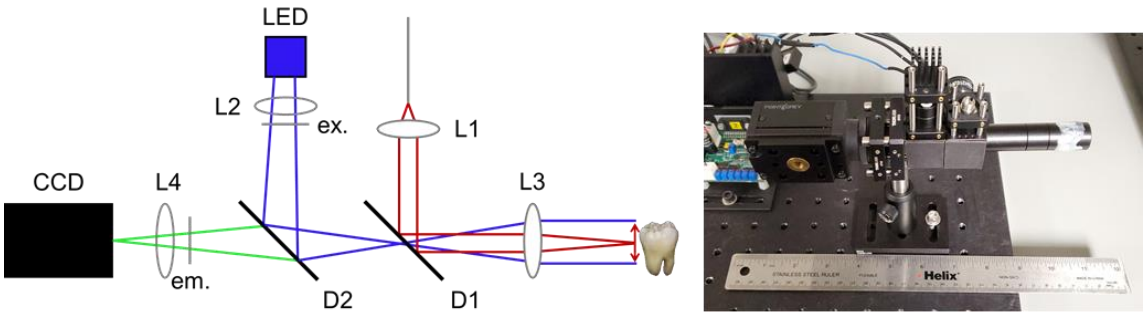

Figure 6.1 Schematic and photograph of the handheld OCT+QLF probe. L = lens, LED = LED excitation source, ex = excitation filter, D = dichroic, em = emission filter, CCD = charge-coupled device camera.

QLF imaging was incorporated within the handheld OCT probe, providing inherently co-registered and simultaneous imaging. The QLF component of the system is designed for autofluorescence of enamel tissue. Excitation wavelengths are isolated from a 455 nm LED (Thorlabs) using an excitation filter with a 45-nm bandwidth centered at 445 nm (Semrock, Rochester, New York). This light is collected using a 10-mm focal length aspheric condenser lens (L2, Thorlabs). A long-pass dichroic mirror (D2) with a 495-nm cut-on (Chroma, Bellows Falls, Vermont) reflects the excitation beam toward the sample. This beam passes through a 950-nm short-pass dichroic (D1, Semrock), where it is combined with the collimated OCT beam. This short-pass dichroic, mounted on a single-axis galvanometer (Thorlabs), scans the reflected OCT beam while transmitting the unaffected QLF excitation and emission light. The co-registered OCT and QLF beams then travel to the sample along a common path through a 12.7-mm diameter, 50-mm focal length achromatic doublet (L3, Thorlabs AC-127-050-A) to simultaneously focus the OCT beam onto the sample, while providing uniform (Köhler) illumination of the region with QLF excitation light. The backscattered OCT signal and fluorescent emissions from the enamel travel back along their original paths and are separated by the short-pass dichroic mirror (D1), which de-scans the OCT beam. Fluorescent emissions are isolated from the excitation light by the long-pass dichroic (D2) and a separate emission filter with an 88-nm bandwidth centered at 550 nm (Semrock). The fluorescent emission is focused onto a compact(44 mm x 29 mm x 58 mm), 1920 x 1440 pixel CCD camera (Point Grey, GS3-U3-28S5M-C, Richmond, British Columbia, Canada) using a 30-mm focal length achromatic doublet (L4, Thorlabs AC-127-030-A). The CCD camera's exposure time was set to match the OCT frame rate for simultaneous image acquisition in order to minimize QLF image flicker due to the scanning OCT dichroic mirror (D1).

Natural WSL Sample 1 from Section 3.4 was imaged with this prototype probe, and the results are shown in **Figure 6.2**. As with the stationary systems, the QLF image

shows clear distinction between sound and lesion through differences in fluorescence: the demineralized enamel in the lesion has less fluorescence and appears darker in the QLF image. In the OCT B-scan, the lesion is distinguishable from sound tissue, with the lesion having greater amounts of backscattering.

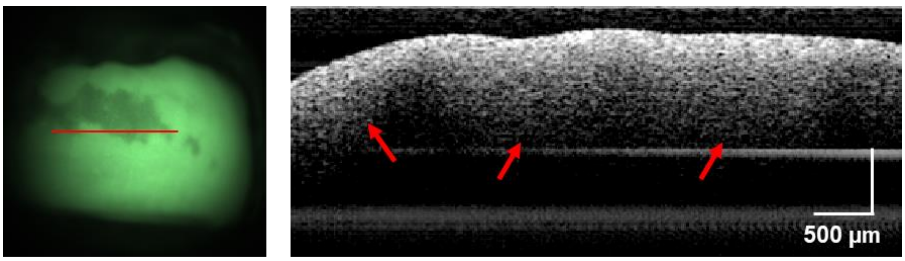

Figure 6.2 Natural WSL sample imaged with the handheld OCT+QLF probe. QLF and OCT B-scan images of Natural WSL Sample 1 acquired with the handheld OCT + QLF probe. The QLF scan is false colored to display in that expected green fluorescence. Red arrows indicate location of lesion.

These preliminary results confirm the probe's capability to be used for enamel imaging. Further work would need to be done to test and optimize *in vivo* imaging of the hard-to-access areas, such as molars and occlusal surfaces. The use of such a handheld device could allow for viewing of hard to reach areas, and various probe attachments can be 3D printed to allow for the probe to access different areas within the mouth. An attachment with a tip that is bent 90^{o} downwards can allow for access to top and sides of back molars. Such a probe would permit an easy transition from *in vitro* to *in vivo* work.

An additional modification for future work could be to use a longer wavelength than the 1300 nm that is most commonly used for commercial OCT systems. As demonstrated in the SWIR imaging work of previous literature[34-37] and in Chapter 5 of this dissertation, wavelengths longer than 1300 nm provide greater lesion contrast. Implementing OCT at such wavelengths may allow for greater imaging depth with high contrast, as

demonstrated in previous literature[105], and potentially greater contrast of lesions from sound enamel, as demonstrated by SWIR reflectance imaging results.

6.2.2 SWIR SFDI for overall oral health assessment

This dissertation covered two main applications of SWIR-SFDI, with Chapter 4 exploiting its traditional use for extracting tissue chromophore concentrations including water, which could be of great importance for assessing oral soft tissue in the application of (i) gingivitis of the gums, and (ii) dry mouth, which largely implicates the tongue. Chapter 5 then explored the implementation of SWIR-SFDI for the direct quantification of scattering in demineralized enamel and subsurface white spot lesions. These two applications demonstrate the capabilities of SFDI as a multifunctional tool that can provide simultaneous assessment of both soft and hard oral tissue in one imaging session. LEDs with nominal wavelengths of 1200 nm and 1300 nm are available for just a few hundred dollars each (Thorlabs). An additional benefit is that the use of incoherent light with the LEDs would eliminate both the speckle and the diffraction issues seen when using a coherent laser source with the DMD.

A priority in future work for this SWIR-SFDI project would first involve establishing a more robust calibration process. While the results for the 1200 and 1300 nm wavelengths were accurate with the current calibration method, calibration with the 10% Intralipid solution yielded higher errors for wavelengths greater than 1350 nm, where the expected diffuse reflectance is very low, as seen in Chapters 4 and 5. For this case, small errors in the calibration lead to large errors in subsequent sample measurements, as seen in Chapter 4 (Figure 4.9). It would be better to calibrate with a phantom with a high diffuse reflectance to reduce the error, or with several calibration phantoms spanning across the range of possible diffuse reflectance values (0 – 1), such as the Spectralon reflectance

standards. If the optical properties of Spectralon standards can be determined for the investigated SWIR wavelengths, these would be ideal, stable samples for calibration.

With SFDI imaging, sample height and surface angle variations will lead to inaccurate optical property extraction if they are not accounted for properly. To overcome this, Gioux *et al.* utilized a Lambertian correction method in which phase profilometry is used to determine the sample's surface profile which is then used to correct for height and contour variations[106]. As is done with SFDI, spatially modulated light is projected onto the sample, and images are taken at various known sample heights in order to determine the phase-height relationship at each pixel[106]. Since teeth have natural curvature on the facial surfaces, and crevices on occlusal (chewing) surfaces, such corrections will need to be investigated and implemented in order to provide accurate SFDI measurements. The work conducted by Gioux *et al.* improved the accuracy of extracted optical properties for surfaces with height variations up to three centimeters, and for tilt angles as high as 40 degrees[106], which should provide adequate correction for dental applications. Additional algorithms were subsequently reported by Zhao *et al.*[107], and van de Giessen *et al.*[108], enabling correction of SFDI images for objects with tilt angles reaching up to 75 degrees and from a rapid single frame measurement, respectively.

While early studies on SFDI used a light propagation model based on diffusion theory to extract optical properties, the validity of this model is known to be limited to situations where the ratio of scattering to absorption coefficients is greater than around 10[92]. Since enamel is approximately 10% water, Darling *et al.* assumed the absorption coefficient of enamel at 1310 nm to be 0.12 cm^{-1}, which is equal to 10% of the water absorption coefficient at that wavelength[109]. From their experimental results for anisotropy factor (g) and scattering coefficient (μ_s)[109], the reduced scattering coefficients of sound and demineralized enamel can be calculated to be 0.18 cm^{-1} and 5.7 cm^{-1}, respectively. Therefore, when imaging dental tissues in the SWIR region, we are likely to encounter

μ'_s/μ_a ratios around 1.5 for sound enamel, and 47.5 for demineralized enamel. This work used a Monte Carlo model for extracting optical properties from diffuse reflectance measurements as this approach has been shown to have wider validity than the diffusion-based model[110]. The tissue-specific refractive index (*n*) and anisotropy factor (*g*) are both needed as input parameters to the Monte Carlo simulations used to generate LUTs for SFDI processing. The LUTs used for this dissertation were generated using a refractive index of 1.4[111] and an anisotropy factor of 0.9[112,113], which are typical values for most biological tissues; however, these values are different for enamel, which has an anisotropy factor of 0.98 at 1310 nm[109], and a refractive index of 1.63[114]. Due to these differences, a future next step for this project would be to generate these LUTs with enamel-specific parameters in order to produce more accurate optical property results. In addition, this dissertation extracted optical properties under the assumption of sample homogeneity, but the tooth is a two-layered tissue comprised of enamel and dentin layers, each with its own refractive index (1.63 and 1.54, respectively[114]), and anisotropy factor (0.96 and 0.93, respectively, measured at 1053 nm[115]). A two-layer LUT as described by Tabassum *et al.*[116] may better account for the tooth structure and should be investigated in future work.

After further optimization of the SWIR-SFDI system, future *in vivo* studies will be needed to determine the capability of the system to assess oral hydration in a clinically relevant manner. A simple mouth drying study can be performed to do this, and the subjects would sit with their mouths open, with clean forced air to simulate dry mouth and tongue and gum hydration would be assessed with the SWIR-SFDI system. Gingival inflammation could also be investigated either through a gingivitis study, or by inducing inflammation with dry brushing to determine if there are any quantifiable differences through SFDI measurements.

While water and lipid are the main tissue chromophores with absorption in the SWIR wavelength range for skin, this is not the case for enamel. Enamel is comprised

largely of hydroxyapatite, which has absorption peaks at 10000 cm^{-1} (1000 nm) and 7000 cm^{-1} (1428 nm)[104]. Such spectra could be investigated with SWIR-SFDI to potentially quantify mineral content with this imaging modality. A larger cohort of samples would also be needed to help validate the scattering differences with different wavelengths seen in Chapter 5.

Appendices

The following MATLAB code was used to create the volumetric OCT depth and AUC maps described in Chapter 3, Section 3.4.1.

```
%% Read in projection view of OCT volume from ImageJ to be used to segment
lesion and create mask:
ImageJ_view = imread('ImageJ_View.bmp');     % Read in projection image
ImageJ_view = rgb2gray(ImageJ_view);         % Convert to grayscale
ImageJ_view = fliplr(ImageJ_view);           % Rotate to be in same
                                             % orientation as OCT volume
ImageJ_view = ImageJ_view(182:693,145:656); % Crop to remove ImageJ
                                             % border


%% Manually segment lesion to create lesion mask:
Mask = roipoly(ImageJ_view); % Use as many points as needed to define
                             % lesion shape

DepthMap = zeros(512,512);   % Pre-allocate matrices (for speed)
AUCMap = zeros(512,512);



%% Going B-scan per B-scan, generate depth and AUC measurements:
for b = 1:512 % length of OCT volume (total number of B-scans)

    % Read in single B-scan:
    Sample = imread(['WSL_volume_',num2str(b),'.bmp']);
    Sample = rgb2gray(Sample);
    Imed_Image = medfilt2(Sample,[6 6]); % Median filter to smooth

    % Detect tooth surface using Canny edge detection method:
    [C4,I4] = max(edge(Imed_Image,'canny',[0 0.55]));

    % Realign B-scan to tooth surface:
    Realigned_Image = zeros(size(Sample,1),size(Sample,2));
    for i = 1:size(Sample,2)
        Realigned_Image(1:(1+size(Sample,1)-I4(i)),i) = ...
            Sample(I4(i):end,i);
    end
    Realigned_Image = mat2gray(Realigned_Image);

    % Apply mask row corresponding to this B-scan to isolate lesion:
    for g = 1:512
        if Mask(b,g) == 1
            Realigned_Image(:,g) = Realigned_Image(:,g);
        else
            Realigned_Image(:,g) = 0;
        end
    end
```

```
    % Binarize resultant lesion B-scan using an intensity threshold:
    Realigned_Image_bw = imbinarize(Realigned_Image,0.4);

    % Going column-by-column, determine the last white pixel and set
    % this as the lesion depth, and determine AUC up to this location:
    for f = 1:512
        A = find(Realigned_Image_bw(:,f));
        TF = isempty(A);
        if TF == 1
            DepthMap(b,f) = 0;
        else
            locs = A(end);
            DepthMap(b,f) = locs*((3582/1.6)/1024); % Correct for
                                                    % refractive index
            AUCMap(b,f) = trapz(Realigned_Image(1:locs,f));
        end
    end

end


%% Display resultant depth map and AUC map:
DepthMap_med = medfilt2(DepthMap,[4 4]);
figure; imagesc(DepthMap_med,[100 600]);
axis image; axis off; colorbar; colormap jet
title('Depth Map');

AUCMap_med = medfilt2(AUCMap,[4 4]);
figure; imagesc(AUCMap_med,[25 125]);
axis image; axis off; colorbar; colormap jet
title('AUC Map');
```

References

1. Garcia RI, Henshaw MM, Krall EA. Relationship between periodontal disease and systemic health. *Periodontology 2000.* 2001;25(1):21-36.
2. Giannobile WV, Beikler T, Kinney JS, Ramseier CA, Morelli T, Wong DT. Saliva as a diagnostic tool for periodontal disease: current state and future directions. *Periodontology 2000.* 2009;50(1):52-64.
3. Armitage GC. The complete periodontal examination. *Periodontology 2000.* 2004;34(1):22-33.
4. Shimada Y, Sadr A, Sumi Y, Tagami J. Application of optical coherence tomography (OCT) for diagnosis of caries, cracks, and defects of restorations. *Current oral health reports.* 2015;2(2):73-80.
5. Ibusuki T, Kitasako Y, Sadr A, Shimada Y, Sumi Y, Tagami J. Observation of white spot lesions using swept source optical coherence tomography (SS-OCT): in vitro and in vivo study. *Dental materials journal.* 2015;34(4):545-552.
6. Robinson C, Shore R, Brookes S, Strafford S, Wood S, Kirkham J. The chemistry of enamel caries. *Critical Reviews in Oral Biology & Medicine.* 2000;11(4):481-495.
7. Yanagisawa T, Miake Y. High-resolution electron microscopy of enamel-crystal demineralization and remineralization in carious lesions. *Journal of electron microscopy.* 2003;52(6):605-613.
8. Samaranayake LP. *Essential microbiology for dentistry.* Elsevier Health Sciences; 2006.
9. Heymann GC, Grauer D. A contemporary review of white spot lesions in orthodontics. *Journal of Esthetic and Restorative Dentistry.* 2013;25(2):85-95.
10. Sonesson M, Bergstrand F, Gizani S, Twetman S. Management of post-orthodontic white spot lesions: an updated systematic review. *European journal of orthodontics.* 2016;39(2):116-121.
11. Kitasako Y, Sadr A, Shimada Y, Ikeda M, Sumi Y, Tagami J. Remineralization capacity of carious and non-carious white spot lesions: clinical evaluation using ICDAS and SS-OCT. *Clinical Oral Investigations.* 2018:1-10.
12. Han P, Suarez-Durall P, Mulligan R. Dry mouth: a critical topic for older adult patients. *Journal of prosthodontic research.* 2015;59(1):6-19.
13. Machoy M, Seeliger J, Szyszka-Sommerfeld L, Koprowski R, Gedrange T, Woźniak K. The use of optical coherence tomography in dental diagnostics: a state-of-the-art review. *Journal of healthcare engineering.* 2017;2017.
14. Schneider H, Park K-J, Häfer M, et al. Dental applications of optical coherence tomography (OCT) in cariology. *Applied Sciences.* 2017;7(5):472.
15. Al-Azri K, Melita LN, Strange AP, et al. Optical coherence tomography use in the diagnosis of enamel defects. *Journal of biomedical optics.* 2016;21(3):036004.
16. Kim J-M, Kang S-R, Yi W-J. Automatic detection of tooth cracks in optical coherence tomography images. *Journal of periodontal & implant science.* 2017;47(1):41-50.
17. Chew H, Zakian C, Pretty I, Ellwood R. Measuring initial enamel erosion with quantitative light-induced fluorescence and optical coherence tomography: an in vitro validation study. *Caries research.* 2014;48(3):254-262.
18. Chan KH, Chan AC, Fried WA, Simon JC, Darling CL, Fried D. Use of 2D images of depth and integrated reflectivity to represent the severity of demineralization in cross-polarization optical coherence tomography. *Journal of biophotonics.* 2015;8(1-2):36-45.

19. Cara AC, Zezell DM, Ana PA, Maldonado EP, Freitas AZ. Evaluation of two quantitative analysis methods of optical coherence tomography for detection of enamel demineralization and comparison with microhardness. *Lasers in surgery and medicine.* 2014;46(9):666-671.
20. Zhou Y, Shimada Y, Matin K, Sadr A, Sumi Y, Tagami J. Assessment of bacterial demineralization around composite restorations using swept-source optical coherence tomography (SS-OCT). *Dental Materials.* 2016;32(9):1177-1188.
21. Austin RS, Taha MH, Festy F, et al. Quantitative Swept-Source Optical Coherence Tomography of Early Enamel Erosion in vivo. *Caries research.* 2017;51(4):410-418.
22. Mandurah M, Sadr A, Shimada Y, et al. Monitoring remineralization of enamel subsurface lesions by optical coherence tomography. *Journal of biomedical optics.* 2013;18(4):046006.
23. Lee RC, Kang H, Darling CL, Fried D. Automated assessment of the remineralization of artificial enamel lesions with polarization-sensitive optical coherence tomography. *Biomedical optics express.* 2014;5(9):2950-2962.
24. Shimada Y, Nakagawa H, Sadr A, et al. Noninvasive cross-sectional imaging of proximal caries using swept-source optical coherence tomography (SS-OCT) in vivo. *Journal of biophotonics.* 2014;7(7):506-513.
25. Nakajima Y, Shimada Y, Sadr A, et al. Detection of occlusal caries in primary teeth using swept source optical coherence tomography. *Journal of biomedical optics.* 2014;19(1):016020.
26. Maia AMA, Freitas AZ, L Campello S, Gomes ASL, Karlsson L. Evaluation of dental enamel caries assessment using quantitative light induced fluorescence and optical coherence tomography. *Journal of biophotonics.* 2016;9(6):596-602.
27. Fried D, Xie J, Shafi S, Featherstone JD, Breunig T, Le CQ. Imaging caries lesions and lesion progression with polarization sensitive optical coherence tomography. *Journal of biomedical optics.* 2002;7(4):618-628.
28. Wada I, Shimada Y, Ikeda M, et al. Clinical assessment of non carious cervical lesion using swept-source optical coherence tomography. *Journal of biophotonics.* 2015;8(10):846-854.
29. Turkistani A, Nakashima S, Shimada Y, Tagami J, Sadr A. Microgaps and demineralization progress around composite restorations. *Journal of dental research.* 2015;94(8):1070-1077.
30. Chen R, Rudney J, Aparicio C, Fok A, Jones R. Quantifying dental biofilm growth using cross-polarization optical coherence tomography. *Letters in applied microbiology.* 2012;54(6):537-542.
31. Koprowski R, Machoy M, Woźniak K, Wróbel Z. Automatic method of analysis of OCT images in the assessment of the tooth enamel surface after orthodontic treatment with fixed braces. *Biomedical engineering online.* 2014;13(1):48.
32. Seeliger J, Machoy M, Koprowski R, Safranow K, Gedrange T, Woźniak K. Enamel thickness before and after orthodontic treatment analysed in optical coherence tomography. *BioMed research international.* 2017;2017.
33. Walther J, Golde J, Kirsten L, et al. In vivo imaging of human oral hard and soft tissues by polarization-sensitive optical coherence tomography. *Journal of biomedical optics.* 2017;22(12):121717.
34. Chan KH, Fried D. Multispectral cross-polarization reflectance measurements suggest high contrast of demineralization on tooth surfaces at wavelengths beyond 1300 nm due to reduced light scattering in sound enamel. *Journal of biomedical optics.* 2018;23(6):060501.

35. Chung S, Fried D, Staninec M, Darling CL. Multispectral near-IR reflectance and transillumination imaging of teeth. *Biomedical optics express.* 2011;2(10):2804-2814.
36. Fried WA, Fried D, Chan KH, Darling CL. High contrast reflectance imaging of simulated lesions on tooth occlusal surfaces at near-IR wavelengths. *Lasers in surgery and medicine.* 2013;45(8):533-541.
37. Zakian CM, Pretty IA, Ellwood R. Near-infared hyperspectral imaging of teeth for dental caries detection. *Journal of Biomedical Optics.* 2009;14(6):064047.
38. Gioux S, Mazhar A, Cuccia DJ. Spatial frequency domain imaging in 2019: principles, applications, and perspectives. *Journal of Biomedical Optics.* 2019;24(7):071613.
39. Mazhar A, Dell S, Cuccia DJ, et al. Wavelength optimization for rapid chromophore mapping using spatial frequency domain imaging. *Journal of biomedical optics.* 2010;15(6):061716.
40. Nandy S, Mostafa A, Kumavor PD, Sanders M, Brewer M, Zhu Q. Characterizing optical properties and spatial heterogeneity of human ovarian tissue using spatial frequency domain imaging. *Journal of biomedical optics.* 2016;21(10):101402.
41. Wilson RH, Nadeau KP, Jaworski FB, et al. Quantitative short-wave infrared multispectral imaging of in vivo tissue optical properties. *Journal of biomedical optics.* 2014;19(8):086011.
42. Aden A, Anderson P, Burnett GR, Lynch RJ, Tomlins PH. Longitudinal correlation of 3D OCT to detect early stage erosion in bovine enamel. *Biomedical optics express.* 2017;8(2):954-973.
43. Walther J, Schnabel C, Tetschke F, et al. In vivo imaging in the oral cavity by endoscopic optical coherence tomography. *Journal of biomedical optics.* 2018;23(7):071207.
44. Duma V, Dobre G, Demian D, et al. Handheld scanning probes for optical coherence tomography. *Romanian Reports in Physics.* 2015;67(4):1346-1358.
45. Aguirre AD, Zhou C, Lee H-C, Ahsen OO, Fujimoto JG. Optical coherence microscopy. In: *Optical Coherence Tomography.* Springer; 2015:865-911.
46. Agrawal A, Pfefer TJ, Woolliams PD, Tomlins PH, Nehmetallah G. Methods to assess sensitivity of optical coherence tomography systems. *Biomedical optics express.* 2017;8(2):902-917.
47. Holmes J, Hattersley S, Stone N, Bazant-Hegemark F, Barr H. Multi-channel Fourier domain OCT system with superior lateral resolution for biomedical applications. Paper presented at: Coherence Domain Optical Methods and Optical Coherence Tomography in Biomedicine XII2008.
48. Schneider CA, Rasband WS, Eliceiri KW. NIH Image to ImageJ: 25 years of image analysis. *Nature methods.* 2012;9(7):671.
49. Drexler W, Liu M, Kumar A, Kamali T, Unterhuber A, Leitgeb RA. Optical coherence tomography today: speed, contrast, and multimodality. *Journal of biomedical optics.* 2014;19(7):071412.
50. Sundararaj D, Venkatachalapathy S, Tandon A, Pereira A. Critical evaluation of incidence and prevalence of white spot lesions during fixed orthodontic appliance treatment: A meta-analysis. *Journal of International Society of Preventive & Community Dentistry.* 2015;5(6):433.
51. Lopatiene K, Borisovaite M, Lapenaite E. Prevention and treatment of white spot lesions during and after treatment with fixed orthodontic appliances: a systematic literature review. *Journal of oral & maxillofacial research.* 2016;7(2).
52. Izatt JA, Choma MA, Dhalla A-H. Theory of optical coherence tomography. In: *Optical coherence tomography.* Springer; 2015:65-94.

53. Austin R, Giusca C, Macaulay G, Moazzez R, Bartlett D. Confocal laser scanning microscopy and area-scale analysis used to quantify enamel surface textural changes from citric acid demineralization and salivary remineralization in vitro. *Dental Materials.* 2016;32(2):278-284.
54. Kraus MF, Potsaid B, Mayer MA, et al. Motion correction in optical coherence tomography volumes on a per A-scan basis using orthogonal scan patterns. *Biomedical optics express.* 2012;3(6):1182-1199.
55. Sotiras A, Davatzikos C, Paragios N. Deformable medical image registration: A survey. *IEEE transactions on medical imaging.* 2013;32(7):1153.
56. Wang X-J, Milner TE, De Boer JF, Zhang Y, Pashley DH, Nelson JS. Characterization of dentin and enamel by use of optical coherence tomography. *Applied Optics.* 1999;38(10):2092-2096.
57. Lee C, Darling CL, Fried D. Polarization-sensitive optical coherence tomographic imaging of artificial demineralization on exposed surfaces of tooth roots. *dental materials.* 2009;25(6):721-728.
58. Manesh SK, Darling CL, Fried D. Polarization-sensitive optical coherence tomography for the nondestructive assessment of the remineralization of dentin. *Journal of biomedical optics.* 2009;14(4):044002.
59. Sugiura M, Kitasako Y, Sadr A, Shimada Y, Sumi Y, Tagami J. White spot lesion remineralization by sugar-free chewing gum containing bio-available calcium and fluoride: A double-blind randomized controlled trial. *Journal of dentistry.* 2016;54:86-91.
60. Kitasako Y, Sadr A, Shimada Y, Sumi Y, Tagami J. The Utility of Chewing Gum in Treating White Spot Lesions. *Current Oral Health Reports.* 2016;3(2):111-116.
61. Kitasako Y, Sadr A, Shimada Y, Ikeda M, Sumi Y, Tagami J. Remineralization capacity of carious and non-carious white spot lesions: clinical evaluation using ICDAS and SS-OCT. *Clinical oral investigations.* 2019;23(2):863-872.
62. Fried D, Staninec M, Darling CL, Chan KH, Pelzner RB. Clinical monitoring of early caries lesions using cross polarization optical coherence tomography. Paper presented at: Lasers in Dentistry XIX2013.
63. Chan KH, Tom H, Lee RC, et al. Clinical monitoring of smooth surface enamel lesions using CP-OCT during nonsurgical intervention. *Lasers in surgery and medicine.* 2016;48(10):915-923.
64. Espigares J, Sadr A, Hamba H, et al. Assessment of natural enamel lesions with optical coherence tomography in comparison with microfocus x-ray computed tomography. *Journal of Medical Imaging.* 2015;2(1):014001.
65. Park K-J, Haak R, Ziebolz D, Krause F, Schneider H. OCT assessment of non-cavitated occlusal carious lesions by variation of incidence angle of probe light and refractive index matching. *Journal of dentistry.* 2017;62:31-35.
66. Nakagawa H, Sadr A, Shimada Y, Tagami J, Sumi Y. Validation of swept source optical coherence tomography (SS-OCT) for the diagnosis of smooth surface caries in vitro. *Journal of dentistry.* 2013;41(1):80-89.
67. Natsume Y, Nakashima S, Shimada Y, Sadr A, Tagami J, Sumi Y. Estimation of lesion progress in artificial root caries by swept source optical coherence tomography in comparison to transverse microradiography. *Journal of biomedical optics.* 2011;16(7):071408.
68. Pretty IA. Caries detection and diagnosis: novel technologies. *Journal of dentistry.* 2006;34(10):727-739.
69. Van der Veen M, de Jong EdJ. Application of quantitative light-induced fluorescence for assessing early caries lesions. In: *Assessment of Oral Health.* Vol 17. Karger Publishers; 2000:144-162.

70. Pretty I, Pender N, Edgar W, Higham S. The in vitro detection of early enamel de- and re-mineralization adjacent to bonded orthodontic cleats using quantitative light-induced fluorescence. *The European Journal of Orthodontics.* 2003;25(3):217-223.
71. Alammari M, Smith P, de Jong EdJ, Higham S. Quantitative light-induced fluorescence (QLF): a tool for early occlusal dental caries detection and supporting decision making in vivo. *Journal of dentistry.* 2013;41(2):127-132.
72. Nakata K, Nikaido T, Ikeda M, Foxton RM, Tagami J. Relationship between fluorescence loss of QLF and depth of demineralization in an enamel erosion model. *Dental materials journal.* 2009;28(5):523-529.
73. Maia AMA, de Freitas AZ, de L. Campello S, Gomes ASL, Karlsson L. Evaluation of dental enamel caries assessment using quantitative light induced fluorescence and optical coherence tomography. *Journal of biophotonics.* 2016;9(6):596-602.
74. Rohrbach DJ, Muffoletto D, Huihui J, et al. Preoperative mapping of nonmelanoma skin cancer using spatial frequency domain and ultrasound imaging. *Academic radiology.* 2014;21(2):263-270.
75. Laughney AM, Krishnaswamy V, Rice TB, et al. System analysis of spatial frequency domain imaging for quantitative mapping of surgically resected breast tissues. *Journal of biomedical optics.* 2013;18(3):036012.
76. Poon C, Sunar U, Rohrbach DJ, et al. Early assessment of burn severity in human tissue ex vivo with multi-wavelength spatial frequency domain imaging. *Toxicology in Vitro.* 2018;52:251-254.
77. Yafi A, Muakkassa FK, Pasupneti T, et al. Quantitative skin assessment using spatial frequency domain imaging (SFDI) in patients with or at high risk for pressure ulcers. *Lasers in surgery and medicine.* 2017;49(9):827-834.
78. Segelstein DJ. *The complex refractive index of water*, University of Missouri--Kansas City; 1981.
79. Altshuler GB, Anderson RR, Manstein D. Method and apparatus for the selective targeting of lipid-rich tissues. In: Google Patents; 2003.
80. Zhao Y. *Widefield functional and metabolic imaging from 600–1300 nm in the spatial frequency domain* 2018.
81. Corlu A, Choe R, Durduran T, et al. Diffuse optical tomography with spectral constraints and wavelength optimization. *Applied optics.* 2005;44(11):2082-2093.
82. Yazdi HS, O'Sullivan TD, Leproux A, et al. Mapping breast cancer blood flow index, composition, and metabolism in a human subject using combined diffuse optical spectroscopic imaging and diffuse correlation spectroscopy. *Journal of biomedical optics.* 2017;22(4):045003.
83. D O'Sullivan T, Leproux A, Chen J-H, et al. Optical imaging correlates with magnetic resonance imaging breast density and revealscomposition changes during neoadjuvant chemotherapy. *Breast Cancer Research.* 2013;15(1):R14.
84. Cerussi AE, Tanamai VW, Hsiang D, Butler J, Mehta RS, Tromberg BJ. Diffuse optical spectroscopic imaging correlates with final pathological response in breast cancer neoadjuvant chemotherapy. *Philosophical Transactions of the Royal Society A: Mathematical, Physical and Engineering Sciences.* 2011;369(1955):4512-4530.
85. Instruments T. Using lasers with DLP DMD technology. *Lasers & DLP, TI DN.* 2008;2509927.
86. Tabassum S, Zhao Y, Istfan R, Wu J, Waxman DJ, Roblyer D. Feasibility of spatial frequency domain imaging (SFDI) for optically characterizing a preclinical oncology model. *Biomedical optics express.* 2016;7(10):4154-4170.

87. Pera V, Karrobi K, Tabassum S, Teng F, Roblyer D. Optical property uncertainty estimates for spatial frequency domain imaging. *Biomedical optics express.* 2018;9(2):661-678.
88. Flock ST, Jacques SL, Wilson BC, Star WM, van Gemert MJ. Optical properties of Intralipid: a phantom medium for light propagation studies. *Lasers in surgery and medicine.* 1992;12(5):510-519.
89. Nachabe R, Hendriks BH, Desjardins AE, van der Voort M, van der Mark MB, Sterenborg HJ. Estimation of lipid and water concentrations in scattering media with diffuse optical spectroscopy from 900 to 1600 nm. *Journal of biomedical optics.* 2010;15(3):037015.
90. Hale GM, Querry MR. Optical constants of water in the 200-nm to 200-μm wavelength region. *Applied optics.* 1973;12(3):555-563.
91. Allen TJ, Beard PC, Hall A, Dhillon AP, Owen JS. Spectroscopic photoacoustic imaging of lipid-rich plaques in the human aorta in the 740 to 1400 nm wavelength range. *Journal of biomedical optics.* 2012;17(6):061209.
92. Cuccia DJ, Bevilacqua FP, Durkin AJ, Ayers FR, Tromberg BJ. Quantitation and mapping of tissue optical properties using modulated imaging. *Journal of biomedical optics.* 2009;14(2):024012.
93. Troy TL, Thennadil SN. Optical properties of human skin in the near infrared wavelength range of 1000 to 2200 nm. *Journal of biomedical optics.* 2001;6(2):167-177.
94. McClatchy DM, Rizzo EJ, Wells WA, et al. Wide-field quantitative imaging of tissue microstructure using sub-diffuse spatial frequency domain imaging. *Optica.* 2016;3(6):613-621.
95. Bodenschatz N, Krauter P, Liemert A, Wiest J, Kienle A. Model-based analysis on the influence of spatial frequency selection in spatial frequency domain imaging. *Applied optics.* 2015;54(22):6725-6731.
96. Logan CM, Fried WA, Simon JC, Staninec M, Fried D, Darling CL. Multispectral near-infrared imaging of composite restorations in extracted teeth. Paper presented at: Lasers in Dentistry XX2014.
97. Lee RC, Staninec M, Le O, Fried D. Infrared methods for assessment of the activity of natural enamel caries lesions. *IEEE Journal of Selected Topics in Quantum Electronics.* 2016;22(3):102-110.
98. Lim L, Cheung G, Lee S. Comparison of spectral domain and swept-source optical coherence tomography in pathological myopia. *Eye.* 2014;28(4):488.
99. Jones RS, Fried D. Attenuation of 1310-and 1550-nm laser light through sound dental enamel. Paper presented at: Lasers in dentistry VIII2002.
100. Weber JR, Durkin AJ, Tromberg BJ, et al. Multispectral imaging of tissue absorption and scattering using spatial frequency domain imaging and a computed-tomography imaging spectrometer. *Journal of biomedical optics.* 2011;16(1):011015.
101. Bodenschatz N, Brandes AR, Liemert A, Kienle A. Sources of errors in spatial frequency domain imaging of scattering media. *Journal of biomedical optics.* 2014;19(7):071405.
102. Lin AJ, Koike MA, Green KN, et al. Spatial frequency domain imaging of intrinsic optical property contrast in a mouse model of Alzheimer's disease. *Annals of biomedical engineering.* 2011;39(4):1349-1357.
103. Nguyen JQM, Crouzet C, Mai T, et al. Spatial frequency domain imaging of burn wounds in a preclinical model of graded burn severity. *Journal of biomedical optics.* 2013;18(6):066010.

104. Kolmas J, Marek D, Kolodziejski W. Near-Infrared (NIR) spectroscopy of synthetic hydroxyapatites and human dental tissues. *Applied spectroscopy.* 2015;69(8):902-912.
105. Ishida S, Nishizawa N. Quantitative comparison of contrast and imaging depth of ultrahigh-resolution optical coherence tomography images in 800–1700 nm wavelength region. *Biomedical optics express.* 2012;3(2):282-294.
106. Gioux S, Mazhar A, Cuccia DJ, Durkin AJ, Tromberg BJ, Frangioni JV. Three-dimensional surface profile intensity correction for spatially modulated imaging. *Journal of biomedical optics.* 2009;14(3):034045.
107. Zhao Y, Tabassum S, Piracha S, Nandhu MS, Viapiano M, Roblyer D. Angle correction for small animal tumor imaging with spatial frequency domain imaging (SFDI). *Biomedical optics express.* 2016;7(6):2373-2384.
108. Van de Giessen M, Angelo JP, Gioux S. Real-time, profile-corrected single snapshot imaging of optical properties. *Biomedical optics express.* 2015;6(10):4051-4062.
109. Darling CL, Huynh G, Fried D. Light scattering properties of natural and artificially demineralized dental enamel at 1310 nm. *Journal of biomedical optics.* 2006;11(3):034023.
110. Flock ST, Patterson MS, Wilson BC, Wyman DR. Monte Carlo modeling of light propagation in highly scattering tissues. I. Model predictions and comparison with diffusion theory. *IEEE Transactions on Biomedical Engineering.* 1989;36(12):1162-1168.
111. Durduran T, Choe R, Baker WB, Yodh AG. Diffuse optics for tissue monitoring and tomography. *Reports on Progress in Physics.* 2010;73(7):076701.
112. Ghosh N, Mohanty S, Majumder S, Gupta P. Measurement of optical transport properties of normal and malignant human breast tissue. *Applied Optics.* 2001;40(1):176-184.
113. Ansari MA, Erfanzadeh M, Hosseini Z, Mohajerani E. Diffuse optical tomography: image reconstruction and verification. *Journal of lasers in medical sciences.* 2014;5(1):13.
114. Meng Z, Yao XS, Yao H, et al. Measurement of the refractive index of human teeth by optical coherence tomography. *Journal of biomedical optics.* 2009;14(3):034010.
115. Fried D, Glena RE, Featherstone JD, Seka W. Nature of light scattering in dental enamel and dentin at visible and near-infrared wavelengths. *Applied optics.* 1995;34(7):1278-1285.
116. Tabassum S, Pera V, Greening G, Muldoon TJ, Roblyer D. Two-layer inverse model for improved longitudinal preclinical tumor imaging in the spatial frequency domain. *Journal of biomedical optics.* 2018;23(7):076011.